CONTRIBUTION TO THE DEVELOPMENT OF RAYLEIGH-BASED FIBER OPTIC SYSTEMS FOR SENSING APPLICATIONS

Ph.D. DISSERTATION BY:

VERÓNICA DE MIGUEL SOTO

SUPERVISOR:

PROF. DR. MANUEL LÓPEZ-AMO SAINZ

upna
Universidad Pública de Navarra
Nafarroako Unibertsitate Publikoa

PAMPLONA, 2019

upna
Universidad Pública de Navarra
Nafarroako Unibertsitate Publikoa

Agradecimientos

Antes de iniciar la exposición del trabajo realizado, me gustaría dedicar unas palabras de agradecimiento a todas las personas que han colaborado, de una forma u otra, pero todas ellas de forma indispensable en el desarrollo y consecución de este trabajo a lo largo de estos años.

En primer lugar, debo agradecer a mi director de tesis, Manuel López-Amo, por su disponibilidad en todo momento, su confianza y compresión así como sus ganas de compartir su extenso conocimiento en las áreas en las que he tenido la oportunidad de trabajar. Manolo, gracias por tu infinita paciencia y por tu tiempo.

También Agradecer al extenso equipo de compañeros con los que he tenido la suerte de compartir conocimientos, tiempo y trabajo en el laboratorio: Rosana, Mikel, Sergio, David, Aitor Júdez, Jon, Juanjo, Javi, Haritz, Alayn, Jesús, Iñaki… También agradecer a mis compañeros de despacho: Diego, Aritz y María Elena, por sus ánimos y tertulias. Debo hacer especial mención a 4 personas más, empezando por Daniel Leandro. Quiero darle mi más sincero agradecimiento por su paciencia, sus buenos consejos y por transmitirme su amplio conocimiento en los láseres de fibra óptica. Su colaboración ha sido un gran pilar en el desarrollo de esta tesis. Agradecer de corazón a Álvaro González Vila y Ana por su increíble recibimiento durante mi estancia en Mons y ayuda en absolutamente cualquier problema que pudiera surgir. Por último, pero no menos importante, quiero agradecer a Aitor López, excelente compañero y mejor persona, quien me ha acompañado en esta andadura de cuatro años y con el cual ha sido un placer trabajar.

Also I would like to thank Dr. Per-Johan Jason and Prof. Marc Wuilpart from university of MONS (Belgium), for their warm welcome in their team during my short-term stay. It was a pleasure to work in your fantastic group and to have the opportunity to learn from you and from so many and interesting things as I was able to do.

También quiero agradecer a mis amigas: Cris, Irene, Noemí, las dos Elenas, Aitzi y Sarita. Gracias por los buenos ratos que hemos pasado juntas, los cafés interminables y por vuestro apoyo incondicional.

Por supuesto, quiero agradecer a mis padres, Matilde y Santiago, por su cariño, ayuda y apoyo incondicionales desde que empecé esta larga carrera. Sin ellos y su esfuerzo no habría sido posible llegar hasta aquí.

Por último, agradecer a mi nueva familia navarra por su apoyo en todo momento, sus consejos y su cariño y paciencia infinitos. Os estaré siempre agradecida por todo lo bueno que me habéis dado y hecho por mí. Gracias a Alicia, Iñaki, abuela Rosa, tía Rosa, tío Vicente, Iker y Javier.

Termino dándole las gracias a mi compañero por excelencia, en lo profesional y lo personal, a la persona que más me ha ayudado desde que empecé mi andadura en la UPNA y que se merece todas las buenas palabras que se me ocurran. Aitor, gracias por todo. Gracias por tu paciencia y compresión, por tus consejos y por darme fuerzas cuando más me flaqueaban. Gracias a ti ha sido más fácil superar este reto que a veces me parecía inalcanzable. Espero que sigamos acumulando triunfos juntos.

ABSTRACT

Fiber optic sensor technology has experienced a tremendous growth since its early beginnings in the 1970s, when it was envisioned for sensing physical and chemical parameters. Besides, the demonstration of the first fiber laser in 1961 brought intensive research into fiber laser technology, which has radically changed the market situation in the industrial laser sector and sensing applications. Because of this, the development and experimental demonstration of some Rayleigh scattering-based fiber optic systems, including optical fiber lasers, for sensing applications has been carried out in this work. Two of the principal challenges of optical sensor networks have been addressed: multiplexing several fiber optic sensors in a single network ensuring good signal quality and enabling remote sensing at hundreds of kilometers. Most of them are based on random distributed-feedback fiber lasers (RDFB-FL) which are specially oriented for long distance applications. In addition, high resolution sensor systems have been also developed using this type of lasers, achieving enhanced resolution measurements for a variety of physical parameters. For this reason, deep study of the properties of RDFB-FL has an important role in this work.

RESUMEN

La tecnología de los sensores de fibra óptica ha experimentado un gran crecimiento desde sus comienzos en la década de 1970, cuando se contempló su utilización para detectar parámetros tanto físicos como químicos. Además, la demonstración del primer láser de fibra en 1961 atrajo una intensa investigación en este tipo de láseres, lo que cambió radicalmente la situación del mercado en el sector del láser industrial y la interrogación de sensores. Debido a esto, en este trabajo se ha llevado a cabo el desarrollo y demonstración experimental de varios sistemas láser de fibra óptica basados en la dispersión Rayleigh, para su posterior utilización en aplicaciones de interrogación de sensores. Se han abordado dos de los principales retos de las redes ópticas de sensores: la multiplexación de sensores en una única red garantizando una buena calidad de señal y la monitorización remota de estos sensores a cientos de kilómetros. La mayoría de los sistemas propuestos se basan en láseres *random* de fibra, láseres de realimentación distribuida, especialmente adecuados para aplicaciones de larga distancia. Además, se han desarrollado también sistemas de sensores de alta resolución utilizando este tipo de láseres, consiguiendo medidas con resoluciones mejoradas para una variedad de parámetros físicos. Así una parte notable de esta tesis está dedicada al estudio de los láseres *random* de realimentación distribuida en fibra óptica.

Thesis outline

List of figures

Chapter II

Chapter III

Chapter IV

Chapter V

Chapter VI

List of tables

Acronyms

AOM – Acousto-optic Modulator

ASE – Amplified Spontaneous Emission

BOSA – Brillouin Optical Spectrum Analyzer

BW – Bandwidth

C-OTDR – Coherence Optical Time Domain reflectometer

CDM – Coherence-Division Multiplexing

CW – Continuous Wave

CWDM – Coarse Wavelength-Division Multiplexing

DAQ – Data Acquisition card

DCF – Dispersion Compensating Fiber

DFB – Distributed Feedback

DOP – Degree of Polarization

DWDM – Dense Wavelength-Division Multiplexing

EDFA – Erbium Doped Fiber Amplifier

EMI – Electromagnetic Interference

EOM – Electro-optical Amplitude Modulator

EPS – Expanded Polystyrene

ESA – Electrical Spectrum Analyzer

FBG – Fiber Bragg Grating

FDM – Frequency-Division Multiplexing

FFT – Fast Fourier Transform

FL – Fiber Laser

FLM – Fiber Loop Mirror

FOLCI – Fiber Optic Low-coherence Interferometry

FOS – Fiber Optic Sensor

FPI – Fabry-Pérot Interferometer

FSR – Free Spectral Range

FUT – Fiber under Test

FWHM – Full Width at Half Maximum

Hi-Bi – Highly Birefringent

ITU – International Telecommunication Union

LED – Light-emitting Diode

LRI – Local Receiving Interferometer

MASER – Microwave Amplification by Stimulated Emission of Radiation

MOF – Micro-structured Optical Fiber

MZ – Mach-Zehnder

MZI – Mach-Zehnder Interferometer

MWFL – Multi-wavelength Fiber Laser

NLL – Narrow Linewidth Laser

OBR – Optical Backscatter Reflectometer

OPD – Optical Path Difference

OSA- Optical Spectrum Analyzer

OFDR – Optical Frequency Domain Reflectometry

OTDR – Optical Time Domain Reflectometry

OWTDR – Optical Wave Time Domain Reflectometry

PC – Polarization Controller

PCC – Photovoltaic Power Converter

PCF – Photonic Crystal Fiber

PD – Photo Detector

PDM – Polarization-Division Multiplexing

PM – Polarization Maintaining

PSFBG – Phase-Shift Fiber Bragg Grating

RDFB – Random Distributed-Feedback

RDFB-FL – Random Distributed-Feedback Fiber-Laser

RFOSw – Remote Powered by Light Fiber Optic switch

RIN – Relative Intensity Noise

RS – Rayleigh scattering

SBS – Stimulated Brillouin Scattering

SDM – Spatial Division Multiplexing

SE – Stimulated Emission

SHM – Structural health Monitoring

SI – Sensing Interferometer

SMF – Single Mode Fiber

SNR – Signal to Noise Ratio

SOA – Semiconductor Optical Amplifier

SRS – Stimulated Raman Scattering

SWI – Swept wavelength Interferometry

TDM – Time-Division Multiplexing

TLS – Tunable Laser Source

WDM – Wavelength-Division Multiplexing

upna

Universidad Pública de Navarra
Nafarroako Unibertsitate Publikoa

CHAPTER I

Introduction

1.1. Motivation and objectives

Modern optical fiber sensors were developed thanks to two of the most important scientific advances made in the 1960s: the laser and the low-loss optical fiber. The early 1970s was the period when low-loss optical fiber began to be used for sensing purposes apart from telecommunications. This revolutionary work quickly led to the growth of a number of research groups, which focused on the exploitation of this new technology for sensing and measurement. This field has continued to progress and has developed enormously since then due to the advantageous features offered by fiber optic sensing systems. They offer high sensitivity, dynamic range and reliability. In addition to these characteristics, their extraordinary resistance

to high temperatures, corrosion, explosion hazards and their immunity to electromagnetic interference allow their use in hostile environments where other types of sensors cannot operate properly. However, the main difference when comparing fiber-based sensor networks with other sensing technologies lies in the dual functionality of fiber. Not only can it be part of the sensor structure but it also forms the communication channel between the detection site and the central station. Thus, it removes the logistical inconvenience of electrical power supply in remote locations which is a desirable feature in long distance applications. However, increasing the interrogation distance can become a challenge. In relation to this, multiplexing of several sensors in the same optical network is a desirable practice since it is possible to reduce the total cost of the system by sharing a number of devices in the network.

In this technological framework, this thesis wants to contribute to the development of Rayleigh-based fiber optic systems for sensing applications. With this aim in mind, different schemes are presented for sensing purposes being most on them based on random distributed-feedback fiber lasers (RDFB-FL). High resolution sensor systems and remote monitoring of optical fiber networks have been the focus of attention in this work.

RDFB-FL can generate exceptional stable narrow-linewidth laser sources that can be exploited in many sensing applications, achieving high-resolution measurements. In regard to optical sensor networks, the distinctive properties of these fiber lasers, such as high power and long cavities, make them especially convenient for remote long distance sensor monitoring. In addition, their particular mode-less behavior is an advantageous feature for the generation of multi-wavelength and tunable laser sources and their use in multiplexing networks. In this way, two of the main challenges of optical sensor networks have been addressed and it has been shown that improved solutions can be provided using RDFB-FL as the light source.

All the work included in this thesis has been carried out in the context of the activities developed in the Optical Communication group of the Public University of Navarra.

1.2. Thesis outline

This PhD. Work has been divided into five chapters and organized as follows:

In Chapter II, a brief overview of the most important technologies used in the following chapters is presented. The fundamental aspects of sensor networks and optical fiber lasers have been described, highlighting the different types of sensors, amplification mechanisms and multiplexing techniques employed in the present work. An extensive section has been dedicated to RDFB-FL, due to their great relevance in the development of this thesis.

Chapter III provides new applications of a RDFB-FL to develop high resolution sensor systems. Several variations of an initial laser scheme are proposed to perform high resolution temperature, strain and transversal load measurements. Then, a comparative study of several fiber optic sensors to measure cryogenic temperatures is carried out. Finally, a brief study of a quasi-distributed vibration sensor scheme based on ultra-weak FBGs is presented. A post-processing method which eliminates spectral shadowing is also developed, improving the overall performance of the system.

In Chapter IV, two optimization studies of new RDFB-FL structures are presented. Firstly, the performance of a tunable multi-wavelength fiber laser is optimized for its later use in a sensor multiplexing network. Secondly, the operation of a novel scheme that combines a double-pumped RDFB-FL and second-order amplification has been analyzed. The objective of this last study is to maximize the output power of the system, allowing to increase the interrogation distance of a remote sensor network.

Chapter V is dedicated to propose new systems that improve both the multiplexing capacity and the remote monitoring distance of fiber optic sensor networks. All the presented schemes have in common the use of RDFB-FL for the interrogation of the sensor structure. The schemes optimized in the previous chapter are used to interrogate sensor networks and test their performance. The advantageous features of this type of lasers for long distance applications are exploited to reach a maximum monitoring distance of 290 km, establishing a new distance milestone in remote sensing networks.

A summary, the main conclusions drawn and future research tasks are gathered in Chapter VI.

Finally, related publications of the author concerning the work developed within this document are included in the appendix.

1.3. Acknowledgment of Contributions

Different financial supports have allowed to accomplish the work presented in this thesis, as well as co-work relationships inside of the university and outside during the research time developed abroad. Due to the financial support obtained, thanks should be pay to:

- Spanish Government project CICYT/FEDER TEC 2013-47264-C2-2-R
- Spanish Government project AEI/FEDER TEC 2016-76021-C2-1-R
- Cost action MP1401

In the field of the co-work relationships through which the presented work was performed, I would like to thank to:

- Daniel Leandro, Mikel Bravo, Rosa Ana Pérez, Aitor López, Juan Jesus Beato and José Ignacio Pérez-Landazábal (Universidad Pública de Navarra, Spain), Per-Johan Jason (University of Mons, Belgium) Deniz Kurtoğlu and Kivilcim Yüksel (Izmir Institute of Technology, Turkey) due to the common work developed
- Amaia Ortigosa and David Erro (Universidad Pública de Navarra, Spain) for the optical interrogator software development.
- Philippe Roy, Jean-Luis Auguste and Raphael Jamier from XLIM in Limoges (France) for the cooperation in the development and fabrication of the photonic crystal fibers used in this work.
- Per-Johan Jason and Marc Wuilpart for their help during the work developed in Belgium.

To the host of my research period abroad:

- Marc Wuilpart in University of Mons (Belgium).

CHAPTER 2

Overview of the basic technologies employed

The main objective of this chapter is to present a brief overview of the most important technologies used in the following chapters. The fundamental aspects of sensor networks and optical fiber lasers have been described, highlighting the different types of sensors, amplification mechanisms and multiplexing techniques employed in the present work. An extensive section has been dedicated to RDFB-FL, due to its great relevance in the development of this thesis.

2.1. Fiber optic sensor networks

Fiber optic sensor (FOS) networks are formed by three main elements: the sensors or transducers, the communication channel and the interrogation unit. One of the main characteristics that differentiates fiber networks from other sensing technologies is the dual functionality of the fiber, acting as a telemetry path and as a sensor structure at the same time. However, the high cost that the interrogation unit usually presents makes it necessary to share the resources of the network by multiplexing several sensors.

Sensor networks can be classified among different criteria. The most common are: types of sensors, amplification mechanism, network topology and multiplexing technique. Throughout this chapter, each of these criteria will be detailed, focusing especially on the most used elements in the development of this thesis.

2.1.1. Background

An FOS can be defined as a device that modulates the optical signal in response to a measurable environmental parameter (physical, chemical or biological), so that this parameter can be determined after processing the optical signal [1]. Fiber optic technology began with the emerging need for superior performances in specific applications that the existing systems did not provide. The remarkable advantages inherent to this type of sensors, see Table 2. 1, assisted their inclusion in a great diversity of markets.

In an initial classification, sensor networks can be divided between simple and hybrid networks. The first ones include a single type of sensor while the others multiplex sensors with different operating principles. In the same manner, another possible subdivision splits the optical fiber sensor networks according to the principle of operation of the sensors that integrate them: transmission or reflection.

Advantages of FOS	Passive-nonelectrical Small size, flexible, light weight Immunity to ionizing radiation, radio frequency and electromagnetic interferences Environmental robustness, high reliability High sensitivity, accuracy and bandwidth Multiplexing capability Remote and secure data transmission Biocompatible Cost-competitive	
Applications	Biomedical/biologic applications Aerospace and industrial applications Operation in harsh environments: high temperatures, extreme vibration, high voltage… Health monitoring of structures: buildings, tunnels, bridges, heritage structures…	
Magnitude to be measured	Temperature Pressure Flow Liquid level Displacement Vibration Rotation Magnetic fields Acceleration	Chemical substances Force Radiation pH Humidity Strain Velocity Electric field Acoustic field

Table 2. 1. Advantages, possible applications and measurands of fiber optic sensors.

2.1.2. Types of sensors

There are many criteria to classify the types of sensors that form a sensor network. In this review, we will focus on the most used. A detailed state of the art regarding this topic can be found in references [1]-[6].

Topology	Transducing approach	Modulation mechanism
Single-point Multi-point/Quasi-distributed Distributed	Intrinsic Extrinsic	Amplitude Phase Wavelength Polarization

Table 2. 2. Classification of fiber optic sensors.

Point, multi-point or distributed sensors

Depending on their topology and configuration, FOS can be classified as point, multi-point or distributed. A single-point sensor generally present the sensing part located at the tip of the fiber. A multipoint FOS consists of several detection regions along the fiber, where each region can detect the same parameter or a different one. These detection regions can be physically separated from a few millimeters up to several meters away, according to the requirements of the application. The truly distributed FOS use the entire length of the fiber to detect one or more external features, achieving several tens of meters, or even tens of kilometers. This is an exclusive capability of fiber optic sensors and cannot be easily accomplished using traditional electrical detection procedures. Figure 2. 1 shows a graphic representation of each type of sensor according to their topology.

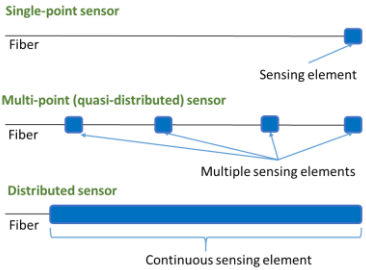

Figure 2. 1. Classification of FOS according to their topology.

Intrinsic-Extrinsic sensor

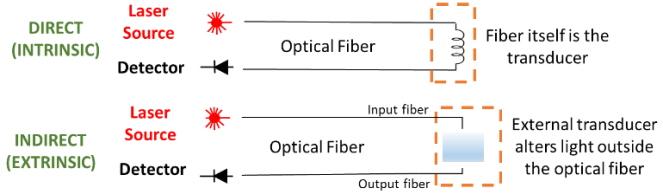

Figure 2. 2. Classification of FOS by transducing approach.

Another way to classify fiber optic sensors is by considering the transduction approach, see Figure 2. 2. First, intrinsic or "all fiber" sensors carry out the detection process in the fiber itself. The second type is formed by extrinsic sensors which use fiber only to guide the light to a detection region. Then, the optical signal leaves the cable and is modulated in another medium. Fiber simply records and transmits the detected signal.

Interferometric – FBG-based sensors

Depending on the modulation mechanism, four main categories can be distinguished: amplitude, phase, wavelength and polarization. In the following work, only interferometric and FBG-based sensors have been employed. For this reason, only the named structures will be described.

Fiber optic interferometers have been widely employed as physical parameter sensors, such as temperature, strain, pressure and refractive index. There are four representative types of interferometers called Mach-Zehnder, Fabry-Perot, Sagnac and Michelson [7]. The first three have served as sensor structures throughout the thesis and Figure 2. 3 shows a basic scheme of their configuration and operating principle.

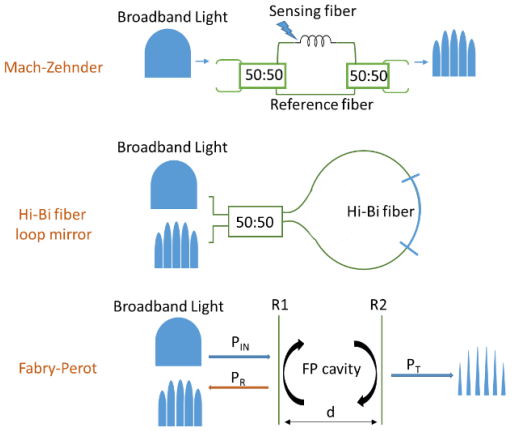

Figure 2. 3. Interferometric sensors employed in this work.

Fabry-Pérot

A Fabry-Pérot interferometer (FPI) is formed by two reflective surfaces separated by a certain distance *L* [8]-[11]. The incident light enters the cavity and interference occurs due to the multiple superpositions of the reflected and transmitted signals between these parallel surfaces. The FPI can be divided into intrinsic or extrinsic, depending on whether the reflector elements are located inside the fiber itself or not. The reflected and transmitted spectrum of the FPI can be explained as a wavelength dependent intensity modulation of the input light, caused by the phase difference between the reflected and transmitted beams in the cavity.

Depending on the wavelength, these signals may be in phase or out-of-phase, originating maximum and minimum peaks in the spectrum. This periodic phase difference φ_{FPI} is determined by the length of the cavity *L* and the refractive index of the cavity material *n,* as expressed in equation 2.1. When any disturbance is induced in the sensor, the optical path difference (OPD) of the FPI varies causing a phase deviation. This deviation results in a change in the wavelength spectrum, which can be measured to quantify the applied perturbation.

$$\varphi_{FPI} = \frac{2\pi}{\lambda} n2L \tag{2.1}$$

Mach-Zehnder

Mach-Zehnder interferometers (MZI) are formed by two independent arms: the reference and the sensing one [12][13] . A coupler is used to divide the light between both arms and then recombine the signals using another coupler. The interference of both signals depends on the optical path difference (OPD) between arms. To use this scheme as a sensor, the reference arm must be isolated and the sensing arm is subjected to variations in temperature, strain, etc. Analyzing the deviations of the interference signal, OPD changes can be determined.

Sagnac

Finally, the basic operation principle of Sagnac interferometer will be briefly described. These sensors have attracted great interest due to their simple structure and manufacture and also because of their environmental robustness [14]. A Sagnac is formed by an optical fiber loop in which two beams propagate in opposite directions with different states of polarization. Both signals recombine in a coupler, interfering at the output port. Although both beams travel the same distance along the interferometer, the OPD is generated by the different propagation speed in the fiber loop, which depends on the polarization state of each propagating signal. To maximize the dependence on polarization, highly birefringent fibers (Hi-Bi fibers) [15]-[17] are generally used as sensing fibers. As in the case of the FPI, the phase of the generated interference present a periodic behavior and is given by the following equation:

$$\varphi_{SI} = \frac{2\pi}{\lambda} BL, \quad B = \left| n_f - n_s \right| \tag{2.2}$$

Where B and L are the birefringent coefficient and the length of the sensing fiber, respectively and n_f and n_s are the effective indices of each propagation mode (fast and slow).

Fiber Bragg grating and phase-shifted fiber Bragg grating

A fiber Bragg grating (FBG) is a periodic disturbance of the refractive index along the fiber that is created by applying an intense optical interference pattern in the core of the fiber. Among all FOS, FBGs have been widely employed for their advantageous properties [18]. Not only they present the inherent advantages of FOS, but their simplicity and versatility make them stand out from other type of sensors. FBGs are inscribed directly on the fiber and the information is encoded in an absolute parameter: the resonance wavelength of the structure. This fact allows these sensors to be self-

referenced and easily multiplexable. There are several types of FBGs depending on the modulation of the refractive index applied. In the development of this thesis, conventional FBGs and phase-shifted FBGs, which are a particular case of the first type, have been used as sensor heads and as filtering elements. When the light illuminates the grating, its refractive index disturbance causes the light of a specific wavelength to be reflected, called the Bragg wavelength λ_{Bragg}, which meets the following condition:

$$\lambda_{Bragg} = 2n_{eff}\Lambda \tag{2.3}$$

Where Λ is the period of the refractive index modulation and n_{eff} is the effective refractive index of the fiber core. The other wavelengths pass through the FBG without suffering any alteration.

A particular case of these grating are the phase-shifted FBG. The distinctive feature of such gratings is the presence of a narrow transmission region in the reflection spectrum, whose total width in the maximum half could be of the order of a few tens, sometimes units of picometers. Several approaches have been proposed to fabricate phase-shifted FBGs [19]-[21]. Figure 2. 4 shows the principle of operation of both structures.

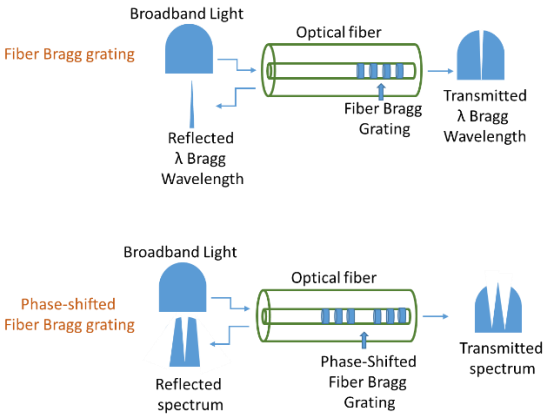

Figure 2. 4. Principle of operation of the FBG-based sensors used in this thesis.

2.1.3. Amplification mechanism

A simple definition of optical amplifier could be: a device that increases the power of an optical signal directly in the optical domain, without the need for electrical processing. Optical amplifiers are essential elements in sensor networks. They allow to increase the capacity, interrogation distance as well as the number of multiplexed sensors, compensating the losses of the network. Without the help of optical amplifiers, electronic amplification would be needed, which implies more expensive systems and difficulties at high transmission rates or in WDM systems.

Despite their numerous advantages, optical amplifiers present several challenges. For example, they generate noise that decreases the signal-to-noise ratio (SNR) of the transmitted signals. In addition, nonlinear effects can be enhanced by high powers in the communication channels, generating crosstalk between them. Finding the compromise between the generated noise and crosstalk is one of the main challenges of these systems [22].

The optical amplification is based on the stimulated emission effect (SE), proposed by Albert Einstein in 1917 [23]. The stimulated emission is the process by which an incoming photon of a specific frequency interact with an excited atomic electron (with an energy level E_2), which causes its fall to a lower energy level E_1. The released energy ($\Delta E=E_2-E_1$) is transferred to the electromagnetic field, creating a novel photon with a frequency $\nu=\Delta E/h$ whose phase, polarization and direction of travel are equal to the photons of the incident wave. This contrasts with the spontaneous emission, which occurs at random intervals without taking into account the ambient electromagnetic field [24]-[26], see Figure 2. 5.

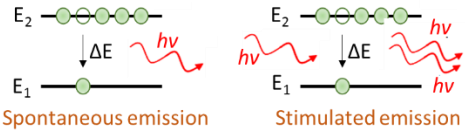

Figure 2. 5. Schematic representation of spontaneous and stimulated emission.

To achieve effective amplification, the stimulated emission rate must be higher than the absorption rate at the frequency of the incident signal. In this manner, the number of excited particles must be increased by using a source of energy called pump. If we combine a pump source, an active medium

where amplification occurs, and an element that injects the pump signal into this amplifying cavity, we obtain what is called an optical fiber amplifier.

Erbium amplification

Erbium-doped fiber amplifiers (EDFA) are by far the most significant fiber amplifiers in the context of long-haul fiber optic communications since their invention in the late 1980s [27]. They can efficiently amplify light in the 1550 nm wavelength region, where telecommunication fibers show their minimum loss. EDFA are based on single-mode fiber whose core has been doped with Er^{3+} and gain is provided by stimulated emission. The characteristics and variations of EDFAs have been widely documented in previous publications [28]-[36], so we will focus on their main features and use in long-range applications.

Although gain can be obtained pumping at different wavelengths, the maximum efficiency of amplification is attained using 980nm-pump lasers. The amplification band extends from 1525 to 1565 nm, which is very convenient for wavelength division multiplexing systems. EDFAs are the optical amplifiers with the highest efficiency gain per pumping power, with values of ~8-10 dB/mW. However, their gain spectrum is not uniform throughout the band and flattening methods are sometimes required.

An EDFA typical scheme is shown in Figure 2. 6. The pump lasers are injected into the laser cavity through two wavelength division multiplexers, mixing the signal and the pumping. The depicted scheme is bi-directional, but unidirectional schemes using a single pump laser in co or counter-propagation can be also implemented. Depending on the desired application, each configuration present some advantages compared to others. The bi-directional scheme would be the most advantageous in terms of performance, with the drawback of using two pumps. In the case of co-propagating pump, the noise in the cavity is lower. However, counter-propagating pump presents a more efficient behavior in terms of generated gain.

The combination of EDFAs and WDM technology offer exceptional capacity to extend the transmission capacity in long-distance fiber optic sensor networks. Many remote sensor systems implementing Erbium amplification have been proposed [37]-[39], reaching a maximum distance of 230km in [37]. Other approaches have attained larger monitoring distances and number of sensors

multiplexed combining EDFA with other amplification methods such as Raman [40]-[43] and Brillouin amplification [44].

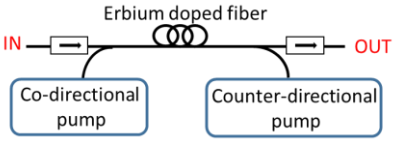

Figure 2. 6. Typical bi-directional EDFA scheme.

Raman amplification

Raman amplification is based on the Raman scattering effect, discovered by the Indian physicist C.V. Raman in 1928 [45][46]. Below is described the basic principle operation of this process. A more detailed explanation is provided through the references [47]-[51].

A Raman amplifier is an optical amplifier based on Raman gain and on the effect of stimulated Raman scattering (SRS). Raman scattering causes an incident photon to be red-shifted (decrease in frequency, longer λ) or blue-shifted (increase in frequency, shorter λ). In both cases, a part of the energy of the incident photon is absorbed or emitted by the material and is translated into molecular vibrations or phonons. Since this process is inelastic, the molecules involved fall to vibration levels different from their initial state, as shown in Figure 2. 7. When the energy level of the molecule is greater or lower than the initial level it is named Stokes or anti-Stokes Raman scattering, respectively.

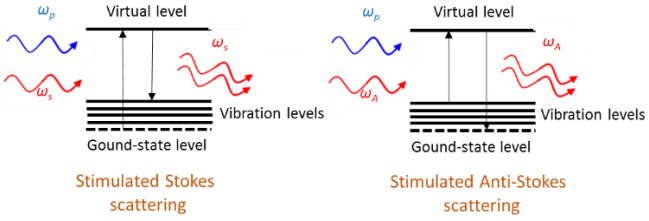

Figure 2. 7. Schematic of the stimulated Stokes and Anti-Stokes Raman scattering processes.

The active Raman medium is frequently an optical fiber, although it can also be a bulk crystal or a cell with a liquid or gas medium. An input signal can be amplified if co-propagates or counter-propagates together with the pump beam, whose wavelength is usually a few tens of nanometers shorter. For the silica fibers, the maximum gain is obtained for a frequency shift of ~10-15 THz between the pump and the signal, depending on the composition of the fiber core. This frequency difference between the pump and the signal is called Stokes shift. The gain bandwidth is more than 40 THz wide, with a dominant peak close to 13.2 THz (~100nm in the 1550nm-band) (see Figure 2. 8) [52].

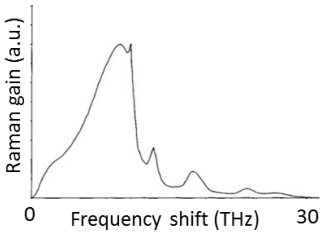

Figure 2. 8. Diagram of the Raman gain spectrum.

The most widely used amplification technique for remote sensor networks is definitely distributed Raman amplification (DRA). It has all the properties inherent to Raman amplification and also has very advantageous qualities for long distance applications, to list some of them:

- A special type of fiber is not needed to generate amplification, since Raman scattering is an inherent process of the germane-silicate fibers. The transmission fiber itself acts as the amplifier.
- Raman gain is available over a wide region, ranging from approximately 0.3 to 2 mm. Gain can be generated at any wavelength by appropriately modifying the pump wavelength, even combining several pumps to obtain a wider gain spectrum.
- The direction of propagation of the pump signal can be chosen to adapt the structure for the requirements of each desired application (noise, gain…).
- DRA provides distributed amplification along the fiber, overcoming the losses at every point and improving the SNR.
- Raman amplification has a relatively broad-band bandwidth of 5 THz, and the gain is reasonably flat over a wide wavelength range.

Several works have developed this technique for remote monitoring applications [53]-[62]. The maximum distance achieved was 250 km in [61], where four sensors were multiplexed and interrogated in a remote system implementing Raman amplification.

Brillouin amplification

While the scattering from optical phonons is known as scattering Raman, the interaction of light with acoustic phonons is named scattering Brillouin after Léon Brillouin. He theoretically predicted light scattering from thermally excited acoustic waves in 1922 [63].

The basic principle of Brillouin scattering is as follows: the incident photon is converted into a scattered photon of slightly lower energy and a phonon. The coupling of the optical pump signal and the acoustic waves occurs via a process called electrostriction. Scattering Brillouin can occur spontaneously at low and also at higher optical powers, originating spontaneous and stimulated Brillouin scattering, respectively. The latter involves a strong nonlinear optical gain for the back-reflected wave. The frequency of the reflected light is slightly lower than that of the incident beam and this difference in frequency corresponds to the frequency of the emitted phonons, called Brillouin frequency shift (~11 GHz). Brillouin scattering occurs essentially only in backward direction in optical fibers (due to phase-matching considerations) [64]. The Brillouin frequency shift depends on the material and also on the temperature and pressure of the medium. As a result, these dependencies can be exploited for their use in fiber sensing applications. For the sake of clarity, the main features of each type of amplification technique are gathered in Table 2. 3.

Amplification mechanism	Principal Features
Raman	Based on SE and SRS Any pump-λ can be used Amplification BW ~60nm Raman shift ~10-15THz (13.2THZ at 1550nm) Low Gain coefficient ~0.43$(W/Km)^{-1}$ High generation threshold ~1W Co, counter and bi-directional pump can be used • Co-directional pump: provides ↑amplification but ↑non-linear effects • Counter-directional pump: provides ↓non-linear effects and ↓RIN • Bi-directional pump: best performance, but 2 pumps are needed • Higher-order pump: distribute gain evenly and allow to reach longer distances Require long fibers for its generation Main noise sources: Amplified spontaneous scattering, Rayleigh backscattering.
Erbium	Based on SE 980nm pump is more efficient Amplification BW ~40nm Co, counter and bi-directional pump can be used Co-directional gives ↓ noise Counter-directional provides ↑ gain Non uniform gain – flattening needed High gain efficiency ~8-10dB/mW Main noise source: Amplified spontaneous emission
Brillouin	Based on SBS – acoustic phonons Amplification BW ~0.001nm at 1550nm Brillouin shift ~11GHz High Gain coefficient ~249.5$(W/Km)^{-1}$ Low generation threshold ~80mW Counter-directional pump Main noise source: spontaneous Brillouin scattering and thermal noise

Table 2. 3. Main features of Erbium, Raman and Brillouin amplification techniques.

2.1.4. Network Topology

A network topology is defined as the arrangement of a network. There are several topologies that can be used to reach the sensors that constitute a certain network [65][66]. The main four configurations used in fiber sensor networks are shown in Figure 2. 9, and can be used in transmission or reflection mode.

The topology is marked principally by the requirements of each application, taking into account some factors such the range of optical power in which the system works correctly. It is important to take into account the value of the signal level received from each of the sensors to avoid saturating the receiver as well as surpassing the minimum level of signal to guarantee a certain SNR. All the schemes proposed in this thesis follow the serial bus or the dual bus topology, since they are most suitable and cost-effective for long distance applications.

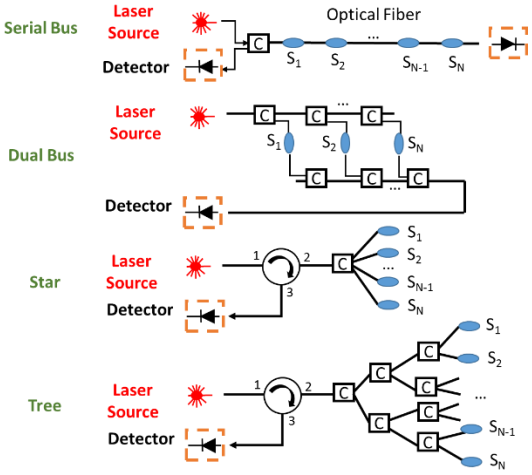

Figure 2. 9. Multiplexing topologies for fiber optic sensors.

2.1.5. Multiplexing Techniques

In telecommunications, multiplexing is a method by which multiple signals are combined over a shared medium. Multiplexing divides the capacity of the communications channel between several logical channels, one for each

multiplexed sensor. The inverse process consists of extracting the original channels in the receiver and is called demultiplexation [66]-[68].

In sensor networks, the main objective of multiplexing is to share the cost of the active devices of the network among all the multiplexed sensors. In this manner, a more efficient use is achieved and the cost per sensor is reduced. The multiplexing process in a sensor network consists of three steps:

- Generate a signal with adequate power, spectral distribution, polarization and modulation.
- Correctly detect the signal encoded by the sensors
- Unequivocally identify the information that corresponds to each sensor.

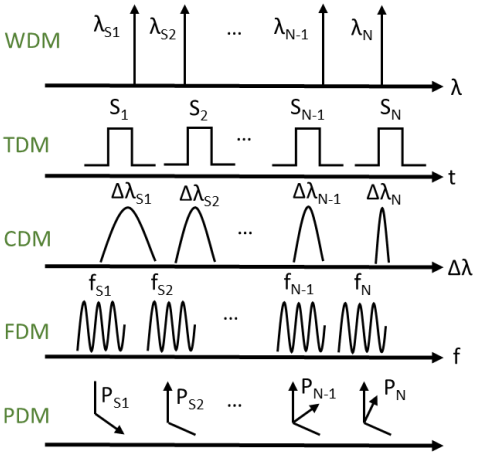

Figure 2. 10. Multiplexing modulation formats.

Various sensor multiplexing techniques have been proposed (see Figure 2. 10), namely, wavelength division multiplexing (WDM), time division multiplexing (TDM), coherence division multiplexing (CDM), frequency division multiplexing (FDM), space division multiplexing (SDM) and hybrid combinations of the above mentioned. It is important to emphasize that any multiplexing technique present ideal features, but an optimal method can be chosen depending on each specific application. Cost, noise, bandwidth and flexibility are factors that should be analyzed to select the most appropriate

multiplexing technique. In addition, there are several interrelated factors that influence this decision, such as:

- The modulation or coding of the optical signal used
- Network topology
- Need or not of optical amplification
- Decoding method
- Types of sensors to be multiplexed
- Economic conditions

Wavelength-division multiplexing

Multiplexing by wavelength division is a type of FDM and consists of combining optical signals with different wavelengths, transmit them together and separate them again in reception [69]. The international telecommunication union (ITU) establishes two additional differentiated categories within these multiplexing systems: coarse wavelength division multiplexing (CWDM) and dense WDM (DWDM). In the first case, a small number of channels (4 to 8) are multiplexed with a large channel spacing (~20 nm). In contrast, DWDM multiplex a large number of channels (more than 40) and consequently the spacing between channels is reduced (12.5, 25, 50 and 100 GHz).

In the area that concerns this thesis, which are the sensor networks, the most interesting technique is DWDM since it allows to maximize the number of sensors to be multiplexed. In WDM sensor networks, the information of each sensor is allocated in a particular wavelength. For this reason, FBGs are the most employed sensors, since their information is encoded in their λ-Bragg, (Chapter II, Section 2.1.2). Some of the advantages this technique presents are:

- Reduces the number of fibers needed to interrogate the sensors network.
- The placement of the sensors is flexible.
- Allows to interrogate all sensors continuously, without the need to assign them a time-slot.

Time-division multiplexing

This technique consists of combining several optical signals, transmit them together and separate them again based on the different arrival times of each one. In sensor networks implementing TDM, each sensor is assigned to a specific time-slot, being able to use all the available bandwidth in that time

interval. This contrasts with what happens in WDM networks, where the bandwidth is shared between all the multiplexed sensors.

Pulsed light sources are required in TDM systems, which desirably emit pulses of short duration, high extinction ratio and low timing jitter. Since each sensor is identified by the time that takes the pulse to travel from the source to the sensor along the network, it is important for the sensors to be placed in separate locations. If necessary, optical delays should be introduced between them to avoid overlapping and crosstalk. Another important consideration in TDM networks is the excess loss induced by the couplers that divide the signal to reach each sensor [66].

Optical time domain reflectometry

Some TDM approaches can be found as:

- Optical time domain reflectometry (OTDR)
- Optical frequency domain reflectometry (OFDR)
- Coherence-OTDR or phase-OTDR

Techniques such as OTDR and phase-OTDR have been employed in this thesis. For this reason, a brief description of their principle of operation is described below.

These systems are based on the phenomenon known as Rayleigh scattering (RS). In silica optical fibers, it represents the predominant event of attenuation between 600 and 1600 nm. Nevertheless and as in many fields in technology, an undesirable effect can be exploited efficiently to get advantage of it.

Rayleigh scattering

When an optical wave propagates in a material, it interacts with its constituent elements (atoms and molecules). This interaction originates a wave radiated in a direction different from that of the incident wave, originating what is known as scattering. If the elements involved in this process are of a much smaller dimension than the incident wavelength, it is called Rayleigh scattering. This mechanism is elastic, so the optical frequency of the reflected signal is the same as that of the incident signal. In addition, all waves scattered within a scattering center are in phase and interfere constructively. In the case of optical fibers, not all scattered light is coupled back to the guided mode, causing loss. The part of the light that is recaptured

by the fiber and propagates in the opposite direction to the incident wave is called Rayleigh backscattering. This concept is widely used throughout the development of the thesis, especially in random distributed feedback fiber lasers, which are described in the following sections. If we consider a uniform fiber and an optical incident pulse of width *dz*, the elementary power backscattered in z and detected at the input of the fiber $dP_B(z)$ is given by:

$$dP_B(z) = P_i(z)B_c(\lambda, z)\alpha_s(\lambda, z)dz = P_0(z)B_c(\lambda, z)\alpha_s(\lambda, z)e^{-\alpha z}dz \quad (2.4)$$

Being P_0 the pulse peak power at z=0, $P_i(z)=P_0(z)e^{-\alpha z}$ the pulse peak after a propagation distance z, α the attenuation of the fiber and $P_b(z)$ the power backscattered in z. A schematic representation of these parameters is shown in Figure 2. 11. Finally, $\alpha_s(\lambda, z)$ represents the local scattering coefficient, which gives the amount of scattered light per unit of length, and $B_c(\lambda, z)$, which is the local backscatter capture fraction. This dimensionless parameter provides the fraction of scattered light that is re-captured in the fiber and backscattered.

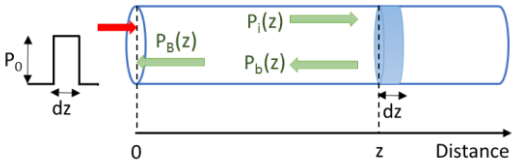

Figure 2. 11. Definition of $P_0(z)$, $P_i(z)$, $P_b(z)$ and $P_B(z)$.

OTDR systems and their variants carry out the analysis of the backscattered signals in the time domain. Pulses are sent from the header to the fiber sensors and the backscattered signal is measured as a function of time. These sensing systems can be classified according to the optical property of the backscattered signal analyzed, which is where the measurable external parameter (temperature, strain, vibration...) is encoded, namely:

- Optical power (OTDR)
- Polarization state (POTDR)
- Phase (phase-OTDR or C-OTDR)

Since OTDRs allows the localization of losses along an optical fiber, any perturbation that induces a power loss along the fiber can be detected and

measured. The basic scheme of an OTDR and a typical detected trace are depicted in Figure 2. 12. A light source injects a pulse in the fiber under test (FUT) using an optical circulator. The backscattered light is redirected through the optical circulator to the photodetector and then the signal processing unit. The latter averages the detected signals for several emitted pulses to enhance the SNR.

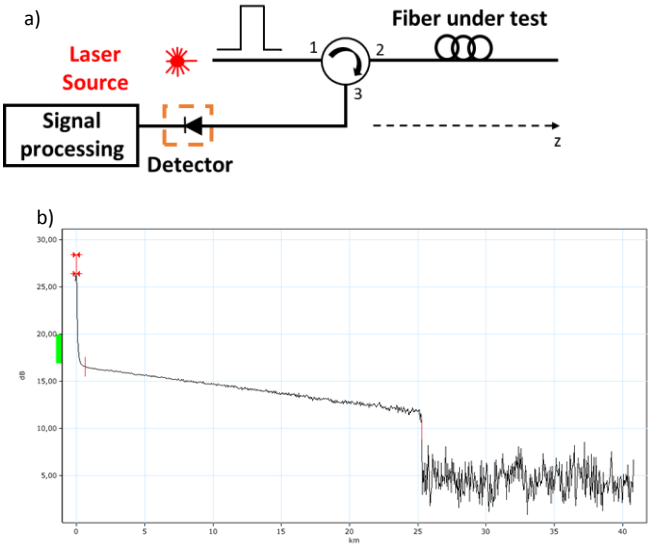

Figure 2. 12. a) Basic configuration of an OTDR and b) example of a real OTDR trace.

In these systems, the time scale is easily translated into the distance scale using the group velocity parameter v_g. Then, an emitted pulse of finite duration T presents a finite width W, being $W=v_gT$. It is important to note that the spatial resolution Δz in the system is determined by half the width of the emitted pulse ($W/2$). In this manner, the contributions of each interval ($z-W/2$, z) along the fiber can be distinguished unequivocally in the header. As a consequence, the total backscattered power detected at the header is given by the integration of equation (2.4) in the interval ($z-W/2$, z). Assuming that α_s and B_c are constant within half the pulse width, the total backscattered signal at point z is given by [70]:

$$P_B(z) = P_0 B_c(\lambda, z)\alpha_s(\lambda, z)\frac{W}{2}e^{-\alpha z} \quad (2.5)$$

This expression assumes that the coherence length of the source (Chapter II, section 2.2.3) is much smaller than half the pulse-width emitted, so that all contributions in the integration interval are added together without taking into account their phases. However, this consideration does not apply in the case of phase-OTDRs, where highly-coherent sources are employed and coherence noise is superimposed on the typical trace of the OTDR, which is mainly a straight line. An example of a real trace measured in a phase-OTDR scheme is depicted in Figure 2. 13. This noise is the result of the coherent interactions (interferences) between the backscattered signals within the backscattering interval (z-W/2, z). To illustrate this effect, let us consider a piece of optical fiber (see Figure 2. 14), where each circle represents a scattering center.

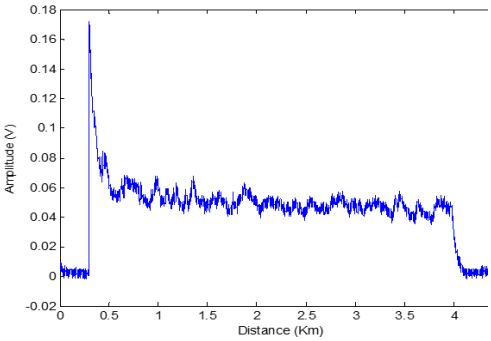

Figure 2. 13. Example of a real phase-OTDR trace.

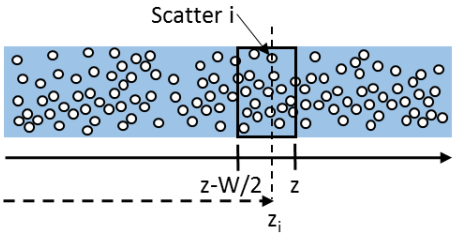

Figure 2. 14. Scheme of the scattering centers.

The electric field resulting from the signal backscattered in z and detected at the input of the fiber can be written as [71]:

$$E_B(z) = \sum_{i=1}^{N} E_0 a_i e^{-\alpha z_i} e^{-2j\beta z_i} \quad (2.6)$$

Being N the number of scattering centers in the integrating zone (z-W/2, z), E_0 the input field amplitude, a_i the fraction of electric field backscattered in the scattering center i, α the attenuation coefficient of the fiber, $\beta=\omega n/c$ the propagation constant and z_i the distance to the scattering center i.

The backscattered power measured at the header $P_B(z)$ is proportional to the square value of $E_B(z)$:

$$P_B(z) \propto |E_B(z)|^2 = f(\phi_{ij}) \quad (2.7)$$

$$\phi_{ij} = \frac{2\omega}{c} n(z_i - z_j) \qquad (i = 1 \rightarrow N, j = 1 \rightarrow N, i \neq j) \quad (2.8)$$

$P_B(z)$ is a function of the phase delay ϕ_{ij}, which represents the phase difference between the signals backscattered in z_i and z_j. The interference pattern generated presents a random behavior because of the randomly distributed scattering centers along the fiber. However, it remains constant for each integrating interval if no external perturbation is applied, thus modifying the phase difference. From equation (2.8), ϕ_{ij} depends on both the refractive index n and the distances between the scattering centers. Temperature, intrusion or vibration modify these parameters and so any deviation can be detected using the phase-OTDR technique.

Since these systems are based on RS, they present low SNRs. One of the proposals to improve this point is to include weak FBGs (FBGs with low reflection coefficient) inscribed along the fiber. In these schemes, a highly-coherent light source emits pulses centered at the λ-Bragg of the inscribed FBGs, increasing the SNR in certain sections of interest [72]-[75]. External disturbances are detected by measuring the amplitude variations detected in the areas where the FBGs are located. Figure 2. 15 shows an example of a characteristic graph obtained with this particular type of scheme, superposing several traces detected over an interval of time. In Chapter III section 3.5, the operation and features of phase-OTDRs combined with weak FBGs are explained in more detail, as well as vibration measurements carried out using this technique.

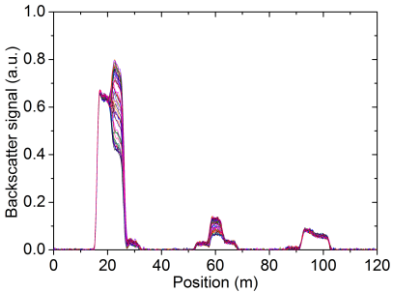

Figure 2. 15. Real phase-OTDR trace implementing the weak-FBG technique.

Moreover, an Optical Backscatter Reflectometer (OBR 4600, Luna Technologies) based on optical frequency domain reflectometry (OFDR) is employed in Chapter II section 3.2.2 to perform distributed temperature measurements [76]. The basic principle of operation of an OFDR system is as follows: a tunable laser illuminates an interferometer formed by a reference arm internal to the instrument and a sensing arm, which is connected to the fiber under test (FUT). Then, this CW laser source completes a sweep in a determined optical frequency range and the interference signal between both arms is detected. Finally, a Fourier Transform is applied to the received signal. As a result, the reflection events (such as R, at position z_R) produced along the FUT can be observed as a function of the optical time delay, which occurs as the light propagates from and back to the device.

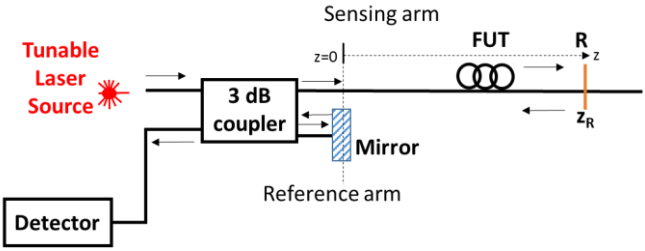

Figure 2. 16. Basic OFDR measurement set-up.

It is important to note that the two interfering signals are characterized by different optical frequencies since the optical source is linearly swept. This frequency difference is proportional to the time delay between the reference

and the sensing signal, and consequently to the distance z_R. However, this can only be assumed if the states of polarization of the interfering beams are identical. In practice, the intrinsic birefringence of the FUT may cause a degradation of the interference process and a modified scheme implementing polarization diversity detection must be applied, such as in Luna's OBR 4600. This particular device is formed by two Mach-Zehnder interferometers placed in cascade, two polarization controllers and a polarization beam splitter and is able to identify the backscattered events present along the FUT after applying a Fourier analysis.

Coherence-division multiplexing

CDM is a technique that allows multiplexing several interferometric sensors (Chapter II, Section 2.1.2.) into a single fiber using the coherence properties of short-coherence length light sources. As in WDM, CDM allows all the sensors to be continuously monitored, separating the signals corresponding to each sensor spatially and not temporarily. Several configurations have been proposed to carry out this technique, namely: series, extrinsic-reference ladder and intrinsic-reference ladder [77].

CDM sensor networks must be carefully designed so that the OPD of each interferometric sensor is much longer than the coherence length of the light source employed (Chapter V section 5.5). In this manner, it is guaranteed that the signals traveling through the interferometer interfere coherently. The main drawbacks of this technique are:

- It can only be used with interferometric sensors.
- It presents a poor SNR.
- The insertion losses are considerable as the number of multiplexed sensors increases. However, this drawback has been studied and power loss can be kept relatively modest by choosing the coupling constants of the couplers appropriately [78].

Other techniques and comparison

As well as the previous techniques, frequency division multiplexing (FDM) and spatial division multiplexing (SDM) can be employed in multiplexed fiber networks. On the one hand, in FDM the sensor information is encoded in a specific frequency of the electric domain (such as carriers, amplitude, frequency or phase modulated of different frequencies). Then, electronic devices are needed to differentiate each sensor [79]. On the other hand, the concept of using SDM to increase the multiplexing capacity of an optical fiber network is almost as old as optical fiber communications itself [80]. This

technique occupies as many channels as sensors are multiplexed. The most obvious approach for implementing this technique is the use of fibers containing multiple cores, which can be exploited as parallel channels for independent signals. If the number of fibers is not an issue for a particular application, CDM is a very flexible approach without crosstalk between sensors. In Table 2. 4, the main pros and cons of the explained multiplexing techniques are gathered.

Mux Technique	Advantages	Drawbacks
WDM	• High measurement speed • Flexible placement of sensors • Continuous monitoring of all the sensors (sensors are λ-separated)	• Expensive and specialized equipment required • A tunable laser or a broadband light source are needed
TDM	• High measurement speed • High multiplexing capability • Simple and efficient schemes • A single optical source is required	• Specialized equipment required • Synchronization needed • Non-continuous monitoring of the sensors (sensors are temporally-separated) • Sensor allocation must be carefully designed
CDM	• Continuous monitoring of all the sensors (sensors are spatially-separated) • Simple equipment required • Provide absolute and insensitive to power fluctuations measurements	• Low measurement speed • Low multiplexing capability • Sensor geometry must be carefully designed

Table 2. 4. Main pros and cons of the multiplexing techniques used along the development of the thesis.

2.2. Fiber lasers

2.2.1. Background

The term "laser" originated as an acronym for "light amplification by stimulated emission of radiation". The first laser was built in 1960 by Theodore H. Maiman at Hughes Research Laboratories, based on the theoretical work of Charles Hard Townes and Arthur Leonard Schawlow. The chronological evolution of lasers is shown in Table 2. 5, starting with Albert Einstein in 1917, who proposed the process that makes lasers possible: stimulated emission (see Chapter II section 2.1.3).

Year	Event
1917	Albert Einstein describes the theory of stimulated emission– the principle of lasers [23].
1940s	Invention of the MASER (microwave amplification by stimulated emission of radiation) by Charles Townes, Arthur Schawlow et al. of Bell Laboratories in New Jersey [81].
1954	Townes et. Al built the first MASER, sending a beam of excited ammonia molecules into a resonant cavity.
1958	Schawlow and Townes proposed the laser [81] .
1960	Theodore H. Maiman demonstrated the first Ruby laser in Hughes Laboratory in Malibu, California [82].
1961	E. Snitzer demonstrates the first fiber laser using a neodymium-doped glass [83][84].
1966	The telecommunication potential of optical fibers is discussed [85].
1970s	Low loss glass fibers were manufactured for the first time by Corning. Silica-based fiber lasers are first presented [86][87]. Raman fiber laser is demonstrated.
1980s	Rare-earth-based fiber amplifiers and lasers are presented.
1986	First Erbium-doped fiber laser developed in Southampton University by Mears et al. [88].
1990s	First practical Raman fiber lasers appear, together with high-power lasers and fiber Bragg gratings [89][90].

Table 2. 5. Historical evolution of lasers.

The beam of light generated by a typical laser presents unique properties when compared to other light sources. Lasers generally show a narrower frequency distribution, much higher intensity and degree of collimation or shorter pulse duration. All this features make lasers a specialized light source that should be used only when their unique properties are required, such as communications systems, military targeting or medical applications, as well

as many other areas [91]. A fiber laser (FL) is a type of laser in which the active medium is an optical fiber generally doped with rare-earth elements such as erbium, ytterbium, neodymium, dysprosium, praseodymium, thulium or holmium. FLs are closely related to doped-fiber amplifiers, previously explained in this chapter Section 2.1.3, which provide light amplification without lasing. Fiber laser technology developed in the laboratory has found its place in the commercial market for its various advantages over other types of lasers. Alternative amplifying technologies, such as solid-state, gas and semiconductor based amplifiers, are well developed and could provide competitive solutions. For instance, semiconductor fiber lasers are formed by a semiconductor gain medium, such as a semiconductor optical amplifier (SOA), and a fiber resonator [92][93]. The technology of these lasers competes with that of rare-earth-doped fiber lasers. SOA-based lasers provide more compact set-ups, containing a small semiconductor chip with electrical and fiber connections. In addition, SOA-based lasers require lower operation powers which often leads to lower costs. However, the output power that can be achieved is limited and also implies stronger nonlinear distortions (self-phase modulation and four-wave mixing) and higher noise figure. Due to their wide amplification bandwidth, several works have been presented for their use in WDM sensor networks applications. Multi-wavelength [94]-[100] and narrow-linewidth tunable lasers [101][102] have been developed using SOA amplification combined with fiber ring structures.

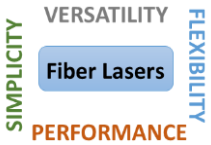

Figure 2. 17. Diagram representing the four main merits of fiber lasers.

Nevertheless, if we compare these systems with all-fiber lasers, the latter show lower coupling losses of the amplifying medium to the fiber. In addition, FLs are outstanding reliable structures, with low operation and maintenance cost which guarantee a high efficiency and beam quality. These are merits that make them suitable for many industrial applications. From plastic and metal marking applications to the perfecting of diamonds and assistance in medical surgeries, fiber lasers are truly one of the most versatile and adaptable equipment on the market. However, FLs have to deal with several challenges that limit their performance. First, the high powers required for

laser generation can cause fiber damage and very short resonators are difficult to achieve, due to the limited gain and pump absorption per fiber unit length.

2.2.2. Types of fiber lasers

Fiber lasers can be classified following different criteria. Among them, the most used ones are their amplification mechanism and their laser cavity configuration. It should be noted that a fiber amplifier can be converted into a fiber laser by placing it inside a cavity designed to provide optical feedback. Lasing will occur when the total gain overcomes the total cavity losses. For instance, Erbium, Raman or Brillouin fiber lasers can be developed exploiting Erbium, Raman or Brillouin amplification, respectively, and also hybrid combinations of them. Regarding the laser cavity, linear/Fabry-Pérot, ring or distributed cavities can be carried out [103], see Figure 2. 18.

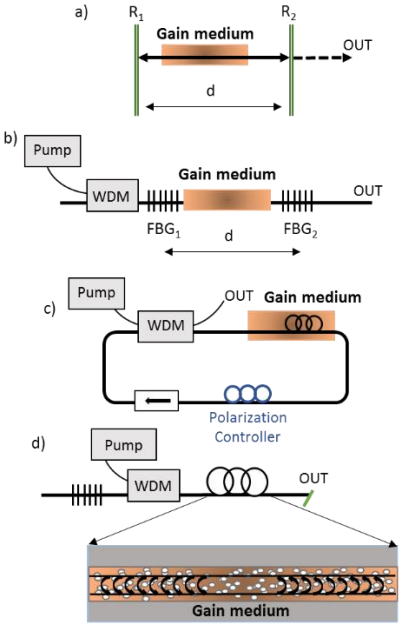

Figure 2. 18. Examples of different types of laser cavities, a) Linear b) Linear using FBGs as reflectors, c) Unidirectional ring and d) distributed-feedback cavity laser.

On the one hand, Fabry-Pérot-cavity fiber lasers offer a compact and simple configuration. Two mirrors of high reflectivity delimit the gain medium. Linear-cavities are frequently used when compact single-longitudinal lasers or high output powers are needed. However, the efficiency of this scheme is reduced when the pump must pass through the dielectric mirrors to enter the cavity. Using WDM to inject the pump into the cavity or exchange the mirrors by fiber loop mirrors or FBGs are possible solutions to this drawback. In fact, efficient all-fiber cavities are achieved using FBGs, since they act as a mirror for the lasing wavelength but are transparent to the pump radiation.

On the other hand, ring cavities are characterized by the round-trips in different directions that light makes inside them. In some cases, isolators and polarization controllers are included to ensure unidirectional laser operation and to control the variable polarization in the cavity, respectively. It should be remarked that ring-cavity fiber lasers have no mirrors; for this reason, they are simple all-fiber schemes and provide a more efficient gain mechanism than linear-cavity fiber lasers. Nevertheless, power fluctuations and non-constant polarization are some of the challenges of these lasers, in addition to the limitations imposed by the cavity length itself. For instance, 1-100m-length cavities give free spectral ranges (FSR) from 1-100 MHz. The free spectral range of an optical resonator or cavity is of great importance since it determines the frequency spacing of its axial (Gaussian-shaped) resonator modes. Therefore, the radiated laser beam is not arbitrary in ring-cavity lasers, but is determined by the axial (length) and cross-sectional dimensions of the cavity. The so-called longitudinal and transversal modes establish a frequency and spatial-dependent output beam, respectively [104].

This drawback affecting the performance of traditional-cavity lasers (linear or ring cavities), does not influence distributed-feedback cavity lasers. They are generally formed by a resonator which consists of a distributed reflecting structure containing a gain medium. Then, the system acts as a distributed reflector in the wavelength range of the laser action. A specific type of these lasers are random distributed feedback fiber laser (RDFB-FL), which have been extensively used in the development of this thesis for its outstanding features, and whose principle of operation is described further in this chapter.

2.2.3. Random distributed-feedback fiber lasers

Random fiber lasers differ from the traditional laser concept formed by an optical resonator encapsulating a gain medium. The optical resonator is an important part of the laser and, as explained above, feedback is necessary to

achieve the lasing emission. In random distributed feedback lasers, the feedback is generated by the multiple scatters distributed randomly along a fiber. This fiber can be also the gain medium or an especially altered one [105]. The advantages of both random lasers and traditional fiber lasers are joined in random fiber lasers. For instance, they provide good directionality and high efficiency together with an outstanding stability [106]. In 2009, Baptista et al. proposed a Raman FBG laser sensor for strain and temperature measurements, which could be considered the first laser system implementing a random distributed-feedback based cavity [107]. It was in 2010, when after the work presented by Turitsyn et al. [108], this type of lasers began to be called random distributed feedback fiber lasers (RDFB-FL). In fact, at the same time Pinto et al. proposed a multiwavelength RDFB-FL using a photonic crystal fiber FLM [109]. However, random lasing was discovered many years before by Ambartsumyan et al. in 1966 [110]. In their experiment, an incoherent feedback was obtained by replacing one of the mirrors of a ruby laser with a diffusive surface. Then, the first distributed feedback fiber laser was proposed in 1970s [111]. After these events, many configurations have been proposed, among them: random lasing using powdered laser crystal [112], colloidal solutions [113], zinc oxide powder [114] and even in bone tissue and cold atoms in 2010 and 2013, respectively [115][116].

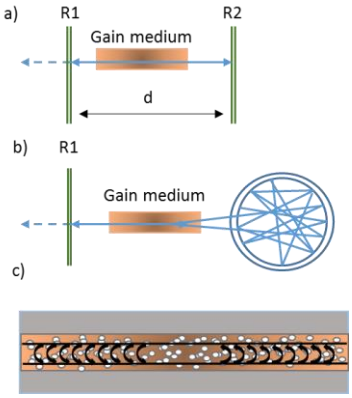

Figure 2. 19. Examples of laser cavities. a) Traditional, b) random c) random distributed-feedback fiber lasers proposed by Turitsyn et al.

In recent years, RDFB-FL have received a lot of attention from researchers which has resulted in a wide range of applications and improvements. Many studies have been carried out to enhance the already promising inherent features of RDFB-FL, for instance, the optimization of the output power [117]-[120], relative intensity noise (RIN) transfer [121][122] and thermal noise [123]. In addition, their spectral and statistical properties have been analyzed in [124]-[126] and a variety of configurations have been proposed implementing polarized pump or linearly-polarized outputs [127]-[130], mixing different fibers in the gain media [131], short cavities [132][133] and tunable [134], multi-wavelength [109][135]-[140] or super-continuum output [141][142]. Finally, RDFB-FL schemes allow to combine the traditionally employed Raman amplification with other amplification mechanisms such as Erbium. In fact, recent works have proposed new schemes for random distributed feedback generation based on Erbium-doped fiber or implementing Brillouin random lasing, Ytterbium-Brillouin or Erbium-Brillouin [140][143]-[151].

The distinctive properties of these lasers use to include high power and long cavities, which make them especially convenient for long-haul telecommunications or sensing applications [152]-[158]. Besides, RDFB-FL present mode-less behavior, which is useful in multiwavelength and tunable laser sources [134]-[140] since the undesired mode competition or mode hoping are eliminated. Their ability to generate outstanding stable narrow-linewidth laser sources can be exploited in many sensing applications [159]-[163], being able to achieve high-resolution measurements [164]. In addition, RDFB-FLs can be internally modulated without frequency restrictions or self-mode-locking effects. Contrary to conventional lasers, the feedback does not correspond to a fixed length. As a result, the length of the laser cavity does not distort the analog internal modulation and does not determine the repetition rate of the generated pulses. An internally modulated RDFB-FL could be used to interrogate a sensor array by TDM as it was proposed in [158], where ten FBGs were monitored at 200 km applying this technique.

After presenting a general vision of the main characteristics and possible applications for which we can exploit this type of lasers, their principle of operation will be described.

Principle of operation

There are many aspects that differentiate RDFB-FLs over conventional lasers, such as their principle of operation. Most of them are based in two

mechanisms: Rayleigh distributed-feedback and stimulated Raman scattering (SRS). Both effects have been described separately before in this chapter (see Chapter II section 2.1.5 and 2.1.3), but below they will be explained in the context of RDFB-FL generation.

In RDFB-FLs based on Raman scattering, the laser medium is a conventional optical fiber. In the telecommunications C-band, attenuation is mainly determined by RS, with a backscattering coefficient as low as ~4.5×10^{-5} km^{-1}. Although the total backward radiation in the fiber is negligible small (<0.1%), the situation changes if the scattered reflection is amplified. Distributed random feedback originates from the RS generated in the naturally disordered refractive index of the fiber core. The gain mechanism is generally based on the SRS: the injected pump power excites a number of molecular vibrations of the silica glass during an inelastic scattering process and losses part of its energy. The residual energy is absorbed by the Stokes photon, which has lower frequency than the pump photon. This frequency difference between the pump and the Stokes photons (Stokes shift) is determined by the structure of vibration levels of the media (see Figure 2. 7). The total amplification of the Stokes wave in a fiber span L can be expressed as exp ($g_R P_p L$) and so increases exponentially with the length of the fiber. g_R and P_p are the frequency-dependent Raman gain coefficient and the pump wave, respectively. However, this gain is limited in practice by the pump wave attenuation α_p along the fiber, $P_p(z)$ ~exp $(-\alpha_p z)$, determining what it is called effective length of the fiber, which can be approximated by $L_{eff} \sim 1/\alpha_p$ (i.e. L_{eff} ~35km in SMF-28 fiber using a pump power of 1.6W) [108]. From this effective length, the transmitted signal is no longer amplified and the output power suffers an exponential decay as it is transmitted along the fiber, see Figure 2. 20. This fact is of particular importance in long distance applications.

Figure 2. 20. Scheme of the gain/loss balance along the RDFB-FL cavity.

In conventional lasers, stimulated emission is spatially coherent and the frequencies of operation (longitudinal modes) are determined by the

resonator's dimensions. Nevertheless, non-resonant feedback occurs in random lasers by reflecting photons from a phase-scrambling medium (the optical fiber). The amplified photons scatter multiple times and do not return to their initial location periodically, avoiding the possibility to form a spatial resonance. As a result, the emitted light has no spatial coherence and is undefined in phase. Due to the absence of resonant feedback, the spectrum emitted is continuous. Nevertheless, CW-operation is only achieved if the lasing threshold is surpassed. If not, the pronounced SBS (see Chapter II section 2.1.3) near the generation threshold causes a different temporal behavior from the steady state.

Near the threshold, irregular pulses are generated with pronounced components in radio-frequency signal at 11GHz (Brillouin shift). A simplified explanation of this effect is as follows: photons with complex trajectories are captured in the cavity but there are some that return back to their initial locations more often than others. Then, when the amplification surpass the losses in the laser cavity, these resonant photons reach the lasing condition first, leading to the generation of narrow stochastic components. These narrow-band spectral components cause Brillouin instabilities, since the resonant light photons interact with the acoustic phonons. As the pump power increases, the residual cavity coherence disappear and laser operation becomes continuous-wave.

At moderate pump-powers, some optical fiber non-linearities can arise and cause deeper mode-mixing, affecting the phases of the cavity modes. For instance, cross-phase modulation may be a reason that causes the frequency perturbation in the cavity. If this happen and the frequency of the "resonant" photons keeps changing due to non-linear interactions, the light field would not belong to any precise mode. As a result, any residual cavity resonances would be eliminated. RDFB-FLs typically generate a well-confined optical spectrum with a 1nm-width, much narrower than the spectral profile of Raman gain (~10nm). Below the generation threshold power, the spectrum is broader and corresponds to the amplified spontaneous emission (ASE) spectrum. The abrupt narrowing of the spectrum proves that real lasing is achieved. In Figure 2. 21, real measured experimental spectra illustrate the evolution of the RDFB-FL output spectra as the pump power is increased.

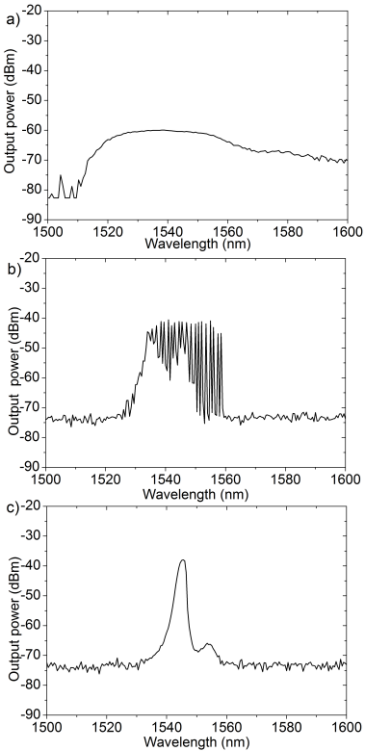

Figure 2. 21. Evolution of the generated spectra with the increasing pump power a) below lasing threshold (ASE spectrum) b) near the threshold (SBS effect) c) above threshold (near Gaussian profile CW mode).

In addition to the pump power requirement, a minimum fiber length of ~2L_{eff} is necessary to guarantee RDFB-FL generation. However, once this requirement is satisfied, a further increase on the fiber length L>>2L_{eff} has little impact of the lasing threshold. In fact, it tends to a constant value for long lengths and increases at L<2L_{eff}~70Km. This contrasts with linear cavities, in which the threshold power grows linearly with the cavity length, exceeding at some point the threshold for RS-based lasing [108].

Regarding the many configurations that can be performed to obtain a RDFB-FL, three main schemes can be distinguished: forward-pumped, backward-

pumped and single-arm configuration. These configurations are depicted in Figure 2. 22.

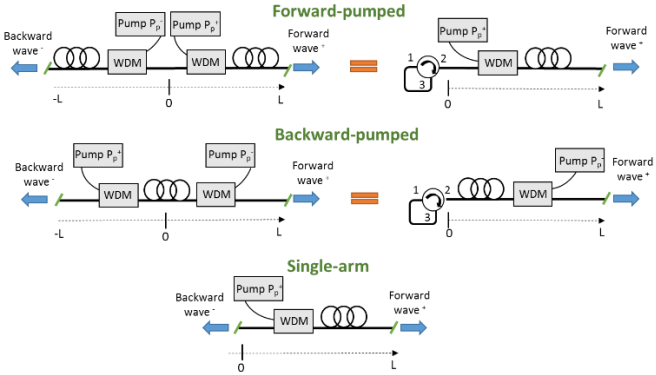

Figure 2. 22. RDFB-FL configurations.

In the first one, the generation wave extracted from the laser is co-propagating with the pump wave. This configuration can be carried out in two technical ways: a symmetrical scheme based on two fiber spans of length *L* and two pump lasers injected in the center of the fiber or an equivalent scheme using only one pump laser. The symmetry of the first system is exploited and a mirror of 100% reflection, such a fiber loop mirror, is placed at one end of the scheme. The main advantage of the reduced scheme is that two times less fiber and only one pump laser are needed for the laser generation. Secondly, in the backward-pumped configuration, the output generation wave is counter-propagating with the pump wave. This scheme can be modified to obtain a reduced version, as in the forward-pump laser configuration. Finally, the third set-up is named single-arm scheme and comprises a fiber span of length L and only one pump laser. Since there are not any point-based reflector, the laser is operated via the random distributed feedback only.

Laser properties

Mode-less behavior

One of the most interesting properties of RDFB-FLs is their mode-less behavior. This particular feature makes them suitable for sensor networks multiplexing and high-resolution sensing applications since the space

between modes is not predetermined. This feature is latter exploited in a high-resolution sensing system in Chapter IV. In order to explain this concept and how unlimited-resolution measurements can be obtained, the mode generation in traditional laser cavities and in RDFB-FL must be compared.

A traditional linear or ring cavity has a fixed cavity length *L*, establishing a fixed longitudinal mode spacing. This condition implies the generation of standing waves, which are longitudinal modes located at different frequencies. These modes occur at wavelengths or frequencies within the gain bandwidth of the laser. The total number of modes generated in a laser cavity is determined by a separation *L* between the mirrors that form the cavity as well as the bandwidth of the laser. The laser frequencies generated are separated a distance Δf following the expression $\Delta f = c/2nL$ where *n* is the refractive index.

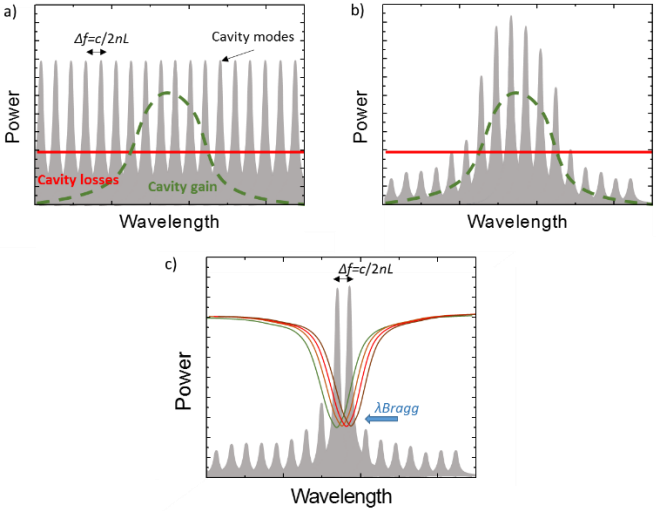

Figure 2. 23. Multi-mode cavity resonance modes before a) and after b) applying the gain profile. c) FBG-filtered single-longitudinal-mode laser for sensing applications.

In sensing applications with traditional-cavity lasers, a wavelength selective device, such as an FBG, is generally employed to filter and select a single-mode of the laser cavity. In this manner, only one mode reaches the lasing threshold at a time corresponding with λ_{FBG}. If the FBG selecting the lasing-

mode experiences an external temperature or strain variation, λ_{FBG} will move accordingly. Then, any deviation can be determined by tracking the lasing wavelength shift. If the λ_{FBG} displacement is greater than the separation between modes Δf, the lasing mode will switch to the adjacent mode, see Figure 2. 23 c). It is important to note that the maximum obtainable resolution using this technique is limited by the separation between modes, since wavelength variations smaller than Δf cannot be properly detected.

On the contrary, RDFB-cavities are not length-fixed and the multiple lasing longitudinal modes degenerate in a collective mode which fills the entire gain bandwidth, see Figure 2. 24 a). If the previous sensing technique is performed with a RDFB-FL, a single-longitudinal-mode behavior will be also achieved at the λ_{FBG}. However, if the λ_{FBG} varies due to an external perturbation, the lasing wavelength will shift continuously along the laser spectrum, see Figure 2. 24 b). The absence of a fixed mode separation leads to unlimited-resolution measurements, without taking into account the limitations that can be induced by the measurement devices themselves.

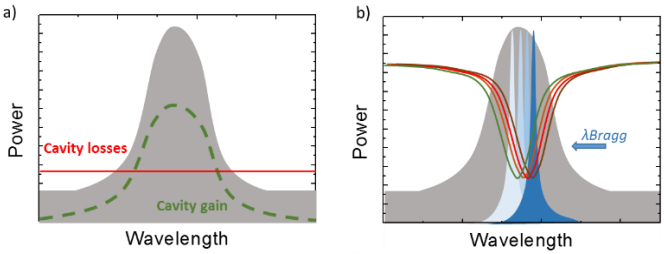

Figure 2. 24. RDFB-FL cavity modes a) without filtering and b) FBG-filtered single-longitudinal mode for sensing applications.

In conventional fiber lasers which have cavity modes, the spectral profile of each individual mode reflecting at each round-trip leads to narrowing after many round-trips. On the contrary, in RDFB-FL with broadband RS reflection, only the gain spectral profile determines narrowing at each round trip. Then, this laser can be treated as a single-mode one with a continuous spectrum which width and central wavelength is defined by the gain profile. Since the Raman gain spectrum present two peaks of maximum gain, see Figure 2. 8, lasing could be achieved in two wavelength bands (near 1555 and 1565 nm, separately or at the same time) depending on the system configuration and the pump power injected in the system. The radio frequency spectra of a

RDFB-FL does not present longitudinal mode beating, which would arise in any cavity of a fixed length. For this reason, these lasers can be treated as mode-less.

Coherence length

The coherence length is a parameter that quantifies the degree of temporal coherence as the propagation length (and therefore propagation time) over which coherence degrades significantly, dropping to the value of 1/e. For a light beam with a Lorentzian optical spectrum, the coherence length can be calculated as:

$$L_{coh} = \frac{c}{n\Delta f} = \frac{\lambda^2}{n\Delta\lambda} \quad (2.\ 9)$$

where c is the speed of light in a vacuum, n is the refractive index of the medium, Δf is the full width at half-maximum (FWHM) linewidth, λ is the signal central wavelength and $\Delta\lambda$ is the FWHM width of the wavelength range of the light source.

The term coherence length is often used instead of coherence time. The reason is that the optical time delays involved real experiments are often determined by optical path lengths, which are easier to determine. For instance, an interferometer shows pronounced interference fringes only if the coherence length of the laser light which illuminates it is at least as long as the optical path-length difference (OPD) of the two arms. Some lasers, particularly single-frequency solid-state lasers, can present coherence lengths as long as 9.5 km for a Lorentzian spectrum with a linewidth of 10 kHz.

On the contrary, low-coherence broadband sources such as light-emitting diodes (LED) are widely employed in fiber optic low-coherence interferometry (FOLCI) applications or also called fiber optic white-light interferometry. As their spectral width varies from 30 to 60 nm, they offer short coherence lengths (compared to laser sources) and narrower interferograms are obtained. Given that the inherent line-width of RDFB-FLs is much narrower than the spectral width of LED sources, they present a considerably wider output spectrum in comparison with traditional lasers ($\Delta\lambda_{3dB}$~1-2 nm, depending on the fiber used for laser generation). Therefore, their coherence length may be short enough to be compatible with low-coherence interferometry systems. FOLCI technique allows the absolute measurement of parameters such as displacement, temperature, strain, pressure, among others. In addition, the precision of the measurements is insensitive to optical

power variations along the fiber link, which is very desirable for remote sensing applications. This concept has been exploited in a remote sensor interrogation application using an RDFB-FL as the light source in Chapter V.

The theoretical coherence length of an RDFB-FL can be calculated applying the equation 2.9. Considering that their spectrum profile can be approximated to a Lorentzian function, a central laser wavelength λ~1550nm and a laser bandwidth of $\Delta\lambda_{3dB}$~1.9nm, the resulting coherence length is ~0.8mm. This value has been measured experimentally using a RDFB-FL with these feature as the light source in a FOLCI scheme. An experiment carried out and the obtained results are detailed in Chapter V, section 5.5. The experimental coherence length is in accordance with the theoretical value of 0.8mm.

Polarization features

The polarization of a laser emission is defined as the direction of the electric field oscillation of the laser beam. If the laser output is polarized, it generally means that it presents a linear polarization state (the electric field oscillates in a certain direction perpendicular to the direction of propagation). However, elliptical polarization is also possible. Other lasers do not generate a polarized output but this does not imply that the laser output is strictly unpolarized. The polarization state may simply be unstable due to i.e. temperature drifts or randomly switch between different directions. For generating a truly un-polarized laser beam, some kind of polarization-scrambling optical device is commonly required.

RDFB-FLs using conventional single-mode fibers and depolarized-pumps generate randomly polarized or unpolarized light. This affirmation has been verified by measuring the degree of polarization (DOP) at the output of a RDFB-FL scheme used in the framework of this thesis. The DOP is a value that describes the portion of an electromagnetic wave which is polarized. A perfectly polarized wave presents a DOP of 100%, while an unpolarized wave may show a DOP of 0%. A partially polarized wave, formed by a superposition of a polarized and unpolarized component, will give a DOP somewhere in between 0 and 100%. The DOP is calculated as the fraction of the total power that is carried by the polarized component of the wave DOP = $I_{pol} / (I_{pol}+I_{unpol})$. The DOP and the Poincare sphere was measured for different pump powers (from 0.2 to 1.7W) using a polarization analyzer device (Agilent N7781B and polarization-NAVIGATOR software), see Figure 2. 25 a). The Poincare sphere describes the polarization and changes in polarization of a propagating wave.

Any given polarization state corresponds to a unique point on the sphere. The pump laser injected in the cavity shows an initial DOP = 0.7. However, the proportion of polarized light decreases to almost 0 as the pump power rises and the laser threshold is exceeded (~1.6W), see Figure 2. 25 b). This confirms the statement established in previous works, which affirms that the beam of light generated by a RDFB-FL is unpolarized. The attempts carried out to govern the polarization state of the RDFB-FL output faced some problems, being unable to achieve higher DOP if a linearly-polarized pump is not applied.

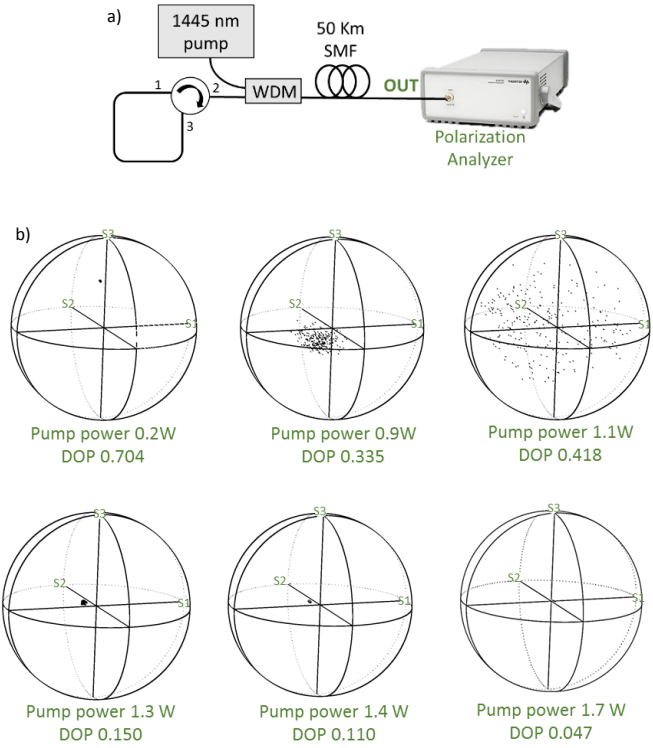

Figure 2. 25. A) Experimental set-up used for polarization measurements and b) Poincare spheres and evolution of the DOP measured at the RDFB-FL output.

If linearly-polarized output beams are needed for a particular application, many adjustments must be implemented in the basic scheme of the RDFB-FL. For instance, using a linearly polarized pump results in the generation of partially polarized output radiation. In addition, the features of the laser (laser threshold, power output, efficiency and degree of polarization) have been proved to be significantly influenced by the polarization state of the pump used [165]-[170]. However, the efficiency of the schemes implementing linearly-polarized pumps is considerably reduced compared to depolarized pumping structures. One of the proposed solutions to this inconvenience is to combine a polarized-pump with an all-PM all-fiber scheme. In [171], they use a linearly-polarized pump whose propagation axis is aligned with the PM-fiber slow-axis used. As a result, the Raman gain generated for other components of the polarization is severely discriminated, creating a single component with linear polarization. This proposal enables high-efficiency and linearly-polarized laser generation.

2.3. References

[1] Udd, E., & Spillman Jr, W. B. (Eds.). (2011). Fiber optic sensors: an introduction for engineers and scientists. John Wiley & Sons.

[2] Lee, B. (2003). Review of the present status of optical fiber sensors. Optical fiber technology, 9(2), 57-79.

[3] Grattan, K. T. V., & Sun, T. (2000). Fiber optic sensor technology: an overview. Sensors and Actuators A: Physical, 82(1-3), 40-61.

[4] Krohn, D. A., MacDougall, T., & Mendez, A. (2014). Fiber optic sensors: fundamentals and applications. Bellingham, WA: Spie Press.

[5] Yin, S., & Francis, T. S. (2002). Fiber optic sensors. CRC press.

[6] Culshaw, B., & Kersey, A. (2008). Fiber-optic sensing: A historical perspective. Journal of lightwave technology, 26(9), 1064-1078.

[7] Lee, B. H., Kim, Y. H., Park, K. S., Eom, J. B., Kim, M. J., Rho, B. S., & Choi, H. Y. (2012). Interferometric fiber optic sensors. Sensors, 12(3), 2467-2486.

[8] Vaughan, M. (2017). The Fabry-Perot interferometer: history, theory, practice and applications. Routledge.

[9] Yoshino, T., Kurosawa, K., Itoh, K., & Ose, T. (1982). Fiber-optic Fabry-Perot interferometer and its sensor applications. IEEE Journal of quantum electronics, 18(10), 1624-1633.

[10] Yoshino, T., Kurosawa, K., Itoh, K., & Ose, T. (1982). Fiber-optic Fabry-Perot interferometer and its sensor applications. IEEE Journal of quantum electronics, 18(10), 1624-1633.

[11] Islam, M., Ali, M., Lai, M. H., Lim, K. S., & Ahmad, H. (2014). Chronology of Fabry-Perot interferometer fiber-optic sensors and their applications: a review. Sensors, 14(4), 7451-7488.

[12] Li, L., Xia, L., Xie, Z., & Liu, D. (2012). All-fiber Mach-Zehnder interferometers for sensing applications. Optics express, 20(10), 11109-11120.

[13] Dandridge, A. (1991). Fiber optic sensors based on the Mach-Zehnder and Michelson interferometers. Fiber Optic Sensors: An Introduction for Engineers and Scientists, 271-323.

[14] Culshaw, B. (2005). The optical fibre Sagnac interferometer: an overview of its principles and applications. Measurement Science and Technology, 17(1), R1.

[15] Ortigosa-Blanch, A., Knight, J. C., Wadsworth, W. J., Arriaga, J., Mangan, B. J., Birks, T. A., & Russell, P. S. J. (2000). Highly birefringent photonic crystal fibers. Optics letters, 25(18), 1325-1327.

[16] Liu, Y., Liu, B., Feng, X., Zhang, W., Zhou, G., Yuan, S., ... & Dong, X. (2005). High-birefringence fiber loop mirrors and their applications as sensors. Applied optics, 44(12), 2382-2390.

[17] Payne, D., Barlow, A., & Hansen, J. (1982). Development of low-and high-birefringence optical fibers. IEEE journal of quantum electronics, 18(4), 477-488.

[18] Kersey, A. D., Davis, M. A., Patrick, H. J., LeBlanc, M., Koo, K. P., Askins, C. G., ... & Friebele, E. J. (1997). Fiber grating sensors. Journal of lightwave technology, 15(8), 1442-1463.

[19] Chehura, E., James, S. W., & Tatam, R. P. (2009, October). A simple method for fabricating phase-shifted fibre Bragg gratings with flexible choice of centre wavelength. In 20th International Conference on Optical Fibre Sensors (Vol. 7503, p. 750379). International Society for Optics and Photonics.
[20] Yang, Y., Liu, X., & Jin, W. (2013, November). Phase Shifted Fiber Bragg Grating Fabrication Techniques and Their Laser Applications. In Asia Communications and Photonics Conference (pp. ATh3D-5). Optical Society of America.
[21] Bakhti, F., & Sansonetti, P. (1996). Wide bandwidth, low loss and highly rejective doubly phase-shifted UV-written fibre bandpass filter. Electronics Letters, 32(6), 581-582.
[22] Urquhart, P., Lopez, O. G., Boyen, G., & Bruckmann, A. (2007, October). Optical amplifiers for telecommunications. In Intelligent Signal Processing, 2007. WISP 2007. IEEE International Symposium on (pp. 1-6). IEEE.
[23] Einstein, A. (1917). Zur quantentheorie der strahlung. Phys. Z., 18, 121-128.
[24] Yablonovitch, E. (1987). Inhibited spontaneous emission in solid-state physics and electronics. Physical review letters, 58(20), 2059.
[25] Sanchez-Mondragon, J. J., Narozhny, N. B., & Eberly, J. H. (1983). Theory of spontaneous-emission line shape in an ideal cavity. Physical review letters, 51(7), 550.
[26] Summers, H. D., Berry, G. M., Lewis, G. W., & Blood, P. (1998). Spontaneous emission control in quantum well laser diodes. Optics express, 2(4), 151-156.
[27] Mears, R. J., Reekie, L., Jauncey, I. M., & Payne, D. N. (1987). Low-noise erbium-doped fibre amplifier operating at 1.54 μm. Electronics Letters, 23(19), 1026-1028.
[28] Desurvire, E. (1994). Erbium-doped fiber amplifiers: principles and applications (Vol. 19). New York: Wiley.
[29] Giles, C. R., & Desurvire, E. (1991). Modeling erbium-doped fiber amplifiers. Journal of lightwave technology, 9(2), 271-283.
[30] Becker, P. M., Olsson, A. A., & Simpson, J. R. (1999). Erbium-doped fiber amplifiers: fundamentals and technology. Elsevier.
[31] Desurvire, E., Simpson, J. R., & Becker, P. C. (1987). High-gain erbium-doped traveling-wave fiber amplifier. Optics Letters, 12(11), 888-890.
[32] Saleh, A. A. M., Jopson, R. M., Evankow, J. D., & Aspell, J. (1990). Modeling of gain in erbium-doped fiber amplifiers. IEEE Photonics Technology Letters, 2(10), 714-717.
[33] Pedersen, B., Bjarklev, A., Povlsen, J. H., Dybdal, K., & Larsen, C. C. (1991). The design of erbium-doped fiber amplifiers. Journal of Lightwave Technology, 9(9), 1105-1112.
[34] Giles, C. R., Desurvire, E., & Simpson, J. R. (1989). Transient gain and cross talk in erbium-doped fiber amplifiers. Optics Letters, 14(16), 880-882.
[35] Ainslie, B. J. (1991). A review of the fabrication and properties of erbium-doped fibers for optical amplifiers. Journal of Lightwave Technology, 9(2), 220-227.

[36] Naji, A. W., Hamida, B. A., Cheng, X. S., Mahdi, M. A., Harun, S., Khan, S., ... & Ahmad, H. (2011). Review of Erbium-doped fiber amplifier. International Journal of Physical Sciences, 6(20), 4674-4689.
[37] Saitoh, T., Nakamura, K., Takahashi, Y., Iida, H., Iki, Y., & Miyagi, K. (2008, May). Ultra-long-distance (230 km) FBG sensor system. In 19th International Conference on Optical Fibre Sensors (Vol. 7004, p. 70046C). International Society for Optics and Photonics.
[38] Perez-Herrera, R. A., Diaz, S., Fernández-Vallejo, M., López-Amo, M., Quintela, M. A., & Lopez-Higuera, J. M. (2009, October). Switchable multi-wavelength erbium-doped fiber laser for remote sensing. In 20th International Conference on Optical Fibre Sensors (Vol. 7503, p. 75031Y). International Society for Optics and Photonics.
[39] Bravo, M., Vallejo, M. F., & Lopez-Amo, M. (2012). Hybrid OTDR-fiber laser system for remote sensor multiplexing. IEEE Sensors Journal, 12(1), 174-178.
[40] Lee, J. H., Chang, Y. M., Han, Y. G., Chung, H., Kim, S. H., & Lee, S. B. (2004). Raman amplifier-based long-distance remote, strain and temperature sensing system using an erbium-doped fiber and a fiber Bragg grating. Optics express, 12(15), 3515-3520.
[41] Rao, Y. J., Ran, Z. L., & Chen, R. R. (2006). Long-distance fiber Bragg grating sensor system with a high optical signal-to-noise ratio based on a tunable fiber ring laser configuration. Optics letters, 31(18), 2684-2686.
[42] Hu, J., Chen, Z., Yang, X., Ng, J., & Yu, C. (2010). 100-km Long distance fiber bragg grating sensor system based on erbium-doped fiber and Raman amplification. IEEE Photonics Technology Letters, 22(19), 1422-1424.
[43] Hu, J., Chen, Z., & Yu, C. (2012). 150-km long distance FBG temperature and vibration sensor system based on stimulated Raman amplification. Journal of Lightwave Technology, 30(8), 1237-1243.
[44] Leandro, D., Ullan, A., Loayssa, A., Lopez-Higuera, J. M., & Lopez-Amo, M. (2011). Remote (155 km) fiber bragg grating interrogation technique combining Raman, Brillouin, and erbium gain in a fiber laser. IEEE photonics technology letters, 23(10), 621-623.
[45] Raman, C. V. (1928). A new radiation.
[46] Raman, C. V., & Krishnan, K. S. (1928). A new type of secondary radiation. Nature, 121(3048), 501.
[47] Islam, M. N. (2002). Raman amplifiers for telecommunications. IEEE Journal of selected topics in Quantum Electronics, 8(3), 548-559.
[48] Islam, M. N. (2004). Overview of Raman amplification in telecommunications. In Raman Amplifiers for Telecommunications 1 (pp. 1-34). Springer, New York, NY.
[49] Bromage, J. (2004). Raman amplification for fiber communications systems. Journal of Lightwave Technology, 22(1), 79.
[50] Namiki, S., Seo, K., Tsukiji, N., & Shikii, S. (2006). Challenges of Raman amplification. Proceedings of the IEEE, 94(5), 1024-1035.
[51] Headley, C., & Agrawal, G. (2005). Raman amplification in fiber optical communication systems. Academic press.
[52] Lin, Q., & Agrawal, G. P. (2006). Raman response function for silica fibers. Optics letters, 31(21), 3086-3088.

[53] Peng, P. C., Tseng, H. Y., & Chi, S. (2004). Long-distance FBG sensor system using a linear-cavity fiber Raman laser scheme. IEEE Photonics Technology Letters, 16(2), 575-577.
[54] Diaz, S., Lasheras, G., Lopez-Amo, M., Urquhart, P., Jauregui, C., & Lopez-Higuera, J. M. (2005, May). Wavelength-division-multiplexed distributed fiber Raman amplifier bus network for sensors. In 17th International Conference on Optical Fibre Sensors (Vol. 5855, pp. 242-246). International Society for Optics and Photonics.
[55] Diaz, S., Lasheras, G., & Lopez-Amo, M. (2005). WDM bi-directional transmission over 35 km amplified fiber-optic bus network using Raman amplification for optical sensors. Optics express, 13(24), 9666-9671.
[56] Han, Y. G., Tran, T. V. A., Kim, S. H., & Lee, S. B. (2005). Development of a multiwavelength Raman fiber laser based on phase-shifted fiber Bragg gratings for long-distance remote-sensing applications. Optics letters, 30(10), 1114-1116.
[57] Han, Y. G., Tran, T. V. A., Kim, S. H., & Lee, S. B. (2005). Multiwavelength Raman-fiber-laser-based long-distance remote sensor for simultaneous measurement of strain and temperature. Optics letters, 30(11), 1282-1284.
[58] Diaz, S., & Lopez-Amo, M. (2006). Comparison of wavelength-division-multiplexed distributed fiber Raman amplifier networks for sensors. Optics express, 14(4), 1401-1407.
[59] Han, Y. G. (2009, October). Long-distance Remote sensors for simultaneous measurement of strain and temperature based on multiwavelength fiber lasers. In 20th International Conference on Optical Fibre Sensors (Vol. 7503, p. 75032B). International Society for Optics and Photonics.
[60] Fernandez-Vallejo, M., Díaz, S., Perez-Herrera, R. A., Passaro, D., Selleri, S., Quintela, M. A., ... & Lopez-Amo, M. (2010). Resilient long-distance sensor system using a multiwavelength Raman laser. Measurement Science and Technology, 21(9), 094017.
[61] Fernandez-Vallejo, M., Rota-Rodrigo, S., & Lopez-Amo, M. (2011). Remote (250 km) fiber Bragg grating multiplexing system. Sensors, 11(9), 8711-8720.
[62] Han, Y. G. (2011). A long-distance remote sensing technique using a multiwavelength Raman fiber laser based on fiber Bragg gratings embedded in a quartz tube. IEEE Sensors Journal, 11(5), 1152-1156.
[63] Brillouin, L. (1922). Diffusion de la lumière et des rayons X par un corps transparent homogène-Influence de l'agitation thermique. In Annales de physique (Vol. 9, No. 17, pp. 88-122). EDP Sciences.
[64] Shen, Y. R., & Bloembergen, N. (1965). Theory of stimulated Brillouin and Raman scattering. Physical Review, 137(6A), A1787.
[65] Perez-Herrera, R. A., & Lopez-Amo, M. (2013). Fiber optic sensor networks. Optical Fiber Technology, 19(6), 689-699.
[66] López-Amo, M., & López-Higuera, J. M. (2011). Multiplexing techniques for FBG sensors. Chapter, 6, 99-115.
[67] Cranch, G. A., & Nash, P. J. (2001). Large-scale multiplexing of interferometric fiber-optic sensors using TDM and DWDM. Journal of lightwave technology, 19(5), 687-699.

[68] Fang, G., Xu, T., & Li, F. (2015). Heterodyne interrogation system for TDM interferometric fiber optic sensors array. Optics Communications, 341, 74-78.
[69] Senior, J. M., & Cusworth, S. D. (1990). Wavelength division multiplexing in optical fibre sensor systems and networks: a review. Optics & Laser Technology, 22(2), 113-126.
[70] Beller, J. (1998). OTDRs and backscatter measurements. Fiber optic test and measurement, 11.
[71] Healey, P. (1984). Fading in heterodyne OTDR. Electronics letters, 20(1), 30-32.
[72] Koyamada, Y., Imahama, M., Kubota, K., & Hogari, K. (2009). Fiber-optic distributed strain and temperature sensing with very high measurand resolution over long range using coherent OTDR. Journal of Lightwave Technology, 27(9), 1142-1146.
[73] Liu, T., Wang, F., Yuan, Q., Liu, Y., Zhang, L., & Zhang, X. (2017, August). Simulation of the performance of phase-sensitive OTDR based on Ultra-weak FBG array using double pulses. In Optical Communications and Networks (ICOCN), 2017 16th International Conference on (pp. 1-3). IEEE.
[74] Zhu, F., Zhang, Y., Xia, L., Wu, X., & Zhang, X. (2015). Improved Φ-OTDR sensing system for high-precision dynamic strain measurement based on ultra-weak fiber Bragg grating array. Journal of Lightwave Technology, 33(23), 4775-4780.
[75] Wang, C., Shang, Y., Liu, X. H., Wang, C., Yu, H. H., Jiang, D. S., & Peng, G. D. (2015). Distributed OTDR-interferometric sensing network with identical ultra-weak fiber Bragg gratings. Optics express, 23(22), 29038-29046.
[76] Duncan, R. G., Soller, B. J., Gifford, D. K., Kreger, S. T., Seeley, R. J., Sang, A. K., ... & Froggatt, M. E. (2007, April). OFDR-based distributed sensing and fault detection for single-and multi-mode avionics fiber-optics. In Joint Conference on Aging Aircraft (pp. 16-19).
[77] Brooks, J., Wentworth, R., Youngquist, R., Tur, M., Kim, B., & Shaw, H. (1985). Coherence multiplexing of fiber-optic interferometric sensors. Journal of Lightwave Technology, 3(5), 1062-1072.
[78] Wentworth, R. H. (1989). Theoretical noise performance of coherence-multiplexed interferometric sensors. Journal of Lightwave Technology, 7(6), 941-956.
[79] Nosu, K., Toba, H., & Iwashita, K. (1987). Optical FDM transmission technique. Journal of lightwave technology, 5(9), 1301-1308.
[80] Richardson, D. J., Fini, J. M., & Nelson, L. E. (2013). Space-division multiplexing in optical fibres. Nature Photonics, 7(5), 354.
[81] Schawlow, A. L., & Townes, C. H. (1958). Infrared and optical masers. Physical Review, 112(6), 1940.
[82] Maiman, T. H. (1960). Stimulated optical radiation in ruby.
[83] Snitzer, E. (1961). Optical maser action of Nd+ 3 in a barium crown glass. Physical Review Letters, 7(12), 444.
[84] Snitzer, E. (1961). Proposed fiber cavities for optical masers. Journal of Applied Physics, 32(1), 36-39.

[85] Kao, K. C., & Hockham, G. A. (1966, July). Dielectric-fibre surface waveguides for optical frequencies. In Proceedings of the Institution of Electrical Engineers (Vol. 113, No. 7, pp. 1151-1158). IET Digital Library.
[86] Stone, J., & Burrus, C. A. (1974). Neodymium-doped fiber lasers: room temperature cw operation with an injection laser pump. Applied optics, 13(6), 1256-1258.
[87] Stone, J., & Burrus, C. (1973). Neodymium-doped silica lasers in end-pumped fiber geometry. Applied Physics Letters, 23(7), 388-389.
[88] Mears, R. J., Reekie, L., Poole, S. B., & Payne, D. N. (1986). Low-threshold tunable CW and Q-switched fibre laser operating at 1.55 μm. Electronics Letters, 22(3), 159-160.
[89] Hill, K. O., & Meltz, G. (1997). Fiber Bragg grating technology fundamentals and overview. Journal of lightwave technology, 15(8), 1263-1276.
[90] Richardson, D. J., Nilsson, J., & Clarkson, W. A. (2010). High power fiber lasers: current status and future perspectives. JOSA B, 27(11), B63-B92.
[91] Silfvast, W. (2004). Introduction. In Laser Fundamentals (pp. 1-6). Cambridge: Cambridge University Press. doi: 10.1017 /CBO9780511616426.003
[92] Connelly, M. J. (2007). Semiconductor optical amplifiers. Springer Science & Business Media.
[93] Dutta, N. K., & Wang, Q. (2013). Semiconductor optical amplifiers. World scientific.
[94] Ahmad, H., Sulaiman, A. H., Shahi, S., & Harun, S. W. (2009). SOA-based multi-wavelength laser using fiber Bragg gratings. Laser physics, 19(5), 1002-1005.
[95] Pleros, N., Bintjas, C., Kalyvas, M., Theophilopoulos, G., Yiannopoulos, K., Sygletos, S., & Avramopoulos, H. (2002). Multiwavelength and power equalized SOA laser sources. IEEE Photonics Technology Letters, 14(5), 693-695.
[96] Ahmad, H., Thambiratnam, K., Sulaiman, A. H., Tamchek, N., & Harun, S. W. (2008). SOA-based quad-wavelength ring laser. Laser Physics Letters, 5(10), 726.
[97] Zhang, Z., Wu, J., Xu, K., Hong, X., & Lin, J. (2009). Tunable multiwavelength SOA fiber laser with ultra-narrow wavelength spacing based on nonlinear polarization rotation. Optics express, 17(19), 17200-17205.
[98] Yu, B. A., Kwon, J., Chung, S., Seo, S. W., & Lee, B. (2003). Multiwavelength-switchable SOA-fibre ring laser using sampled Hi-Bi fibre grating. Electronics Letters, 39(8), 649-650.
[99] Moon, D. S., Kim, B. H., Lin, A., Sun, G., Han, W. T., Han, Y. G., & Chung, Y. (2007). Tunable multi-wavelength SOA fiber laser based on a Sagnac loop mirror using an elliptical core side-hole fiber. Optics express, 15(13), 8371-8376.
[100] Chen, L. R. (2004). Tunable multiwavelength fiber ring lasers using a programmable high-birefringence fiber loop mirror. IEEE Photonics Technology Letters, 16(2), 410-412.

[101] Zhou, D., Prucnal, P. R., & Glesk, I. (1998). A widely tunable narrow linewidth semiconductor fiber ring laser. IEEE Photonics Technology Letters, 10(6), 781-783.
[102] Hu, Z., Li, F., Pan, Z., & Tan, W. (2000). Wavelength-tunable narrow-linewidth semiconductor fiber-ring laser. IEEE Photonics Technology Letters, 12(8), 977-979.
[103] Perez-Herrera, R. A., & Sainz, M. L. A. (2010, November). Fiber lasers for optical sensing applications. In Proceedings of the 3rd WSEAS international conference on Advances in sensors, signals and materials (pp. 125-129). World Scientific and Engineering Academy and Society (WSEAS).
[104] Silfvast, W. (2004). Laser cavity modes. In Laser Fundamentals (pp. 371-401). Cambridge: Cambridge University Press. doi: 10.1017/CBO9780511616426.013
[105] Zhang, L., Xu, Y., Lu, P., Mihailov, S., Chen, L., & Bao, X. (2018). Multi-wavelength Brillouin random fiber laser via distributed feedback from a random fiber grating. Journal of Lightwave Technology, 36(11), 2122-2128.
[106] Churkin, D. V., Sugavanam, S., Vatnik, I. D., Wang, Z., Podivilov, E. V., Babin, S. A., ... & Turitsyn, S. K. (2015). Recent advances in fundamentals and applications of random fiber lasers. Advances in Optics and Photonics, 7(3), 516-569.
[107] Frazão, O., Correia, C., Santos, J. L., & Baptista, J. M. (2009). Raman fibre Bragg-grating laser sensor with cooperative Rayleigh scattering for strain–temperature measurement. Measurement Science and Technology, 20(4), 045203.
[108] Turitsyn, S. K., Babin, S. A., El-Taher, A. E., Harper, P., Churkin, D. V., Kablukov, S. I., ... & Podivilov, E. V. (2010). Random distributed feedback fibre laser. Nature Photonics, 4(4), 231.
[109] Pinto, A. M. R., Frazão, O., Santos, J. L., & Lopez-Amo, M. (2010). Multiwavelength fiber laser based on a photonic crystal fiber loop mirror with cooperative Rayleigh scattering. Applied Physics B, 99(3), 391-395.
[110] Ambartsumyan, R. V., Basov, N. G., Kryukov, P. G., & Letokhov, V. S. (1966). A laser with a nonresonant feedback. IEEE J. Quantum Electron, 2(9), 442-446.
[111] Elachi, C., Evans, G. A., & Yeh, C. (1976). U.S. Patent No. 3,958,188. Washington, DC: U.S. Patent and Trademark Office.
[112] Markushev, V. M., Ter-Gabriélyan, N. É., Briskina, C. M., Belan, V. R., & Zolin, V. F. (1990). Stimulated emission kinetics of neodymium powder lasers. Soviet Journal of Quantum Electronics, 20(7), 773.
[113] Lawandy, N. M., Balachandran, R. M., Gomes, A. S. L., & Sauvain, E. (1994). Laser action in strongly scattering media. Nature, 368(6470), 436.
[114] Cao, H., Zhao, Y. G., Ho, S. T., Seelig, E. W., Wang, Q. H., & Chang, R. P. (1999). Random laser action in semiconductor powder. Physical Review Letters, 82(11), 2278.
[115] Song, Q., Xiao, S., Xu, Z., Liu, J., Sun, X., Drachev, V., ... & Kim, Y. L. (2010). Random lasing in bone tissue. Optics letters, 35(9), 1425-1427.

[116] Baudouin, Q., Mercadier, N., Guarrera, V., Guerin, W., & Kaiser, R. (2013). A cold-atom random laser. Nature physics, 9(6), 357.
[117] Zhang, H., Zhou, P., Xiao, H., & Xu, X. (2014). Efficient Raman fiber laser based on random Rayleigh distributed feedback with record high power. Laser Physics Letters, 11(7), 075104.
[118] Vatnik, I. D., Churkin, D. V., & Babin, S. A. (2012). Power optimization of random distributed feedback fiber lasers. Optics express, 20(27), 28033-28038.
[119] Du, X., Zhang, H., Xiao, H., Ma, P., Wang, X., Zhou, P., & Liu, Z. (2016). High-power random distributed feedback fiber laser: From science to application. Annalen der Physik, 528(9-10), 649-662.
[120] Zhou, P., Ye, J., Xu, J., Zhang, H., Huang, L., Wu, J., ... & Leng, J. (2018, January). The rising power of random distributed feedback fiber laser. In 2017 International Conference on Optical Instruments and Technology: Advanced Laser Technology and Applications (Vol. 10619, p. 106190A). International Society for Optics and Photonics.
[121] Nuño, J., Alcon-Camas, M., & Ania-Castañón, J. D. (2012). RIN transfer in random distributed feedback fiber lasers. Optics Express, 20(24), 27376-27381.
[122] del Campo, J. N., Alcon-Camas, M., & Ania-Castanon, J. D. (2012, June). RIN transfer in random distributed feedback fiber lasers. In Nonlinear Photonics (pp. JM5A-7). Optical Society of America.
[123] Foster, S., Tikhomirov, A., & Milnes, M. (2007). Fundamental thermal noise in distributed feedback fiber lasers. IEEE journal of quantum electronics, 43(5), 378-384.
[124] Smirnov, S. V., & Churkin, D. V. (2013). Modeling of spectral and statistical properties of a random distributed feedback fiber laser. Optics express, 21(18), 21236-21241.
[125] Gorbunov, O. A., Sugavanam, S., & Churkin, D. V. (2015). Intensity dynamics and statistical properties of random distributed feedback fiber laser. Optics letters, 40(8), 1783-1786.
[126] Sarmani, A. R., Bakar, M. A., Bakar, A. A. A., Adikan, F. M., & Mahdi, M. A. (2011). Spectral variations of the output spectrum in a random distributed feedback Raman fiber laser. Optics express, 19(15), 14152-14159.
[127] Wu, H., Wang, Z. N., Churkin, D. V., Vatnik, I. D., Fan, M. Q., & Rao, Y. J. (2014). Random distributed feedback Raman fiber laser with polarized pumping. Laser Physics Letters, 12(1), 015101.
[128] Lou, Z., Xu, J., Huang, L., Zhang, H., Leng, J., Xiao, H., & Zhou, P. (2017). Linearly-polarized random distributed feedback Raman fiber laser with record power. Laser Physics Letters, 14(5), 055102.
[129] Zlobina, E. A., Kablukov, S. I., & Babin, S. A. (2015). Linearly polarized random fiber laser with ultimate efficiency. Optics letters, 40(17), 4074-4077.
[130] Du, X., Zhang, H., Wang, X., Zhou, P., & Liu, Z. (2015). Investigation on random distributed feedback Raman fiber laser with linear polarized output. Photonics Research, 3(2), 28-31.

[131] Zhang, W. L., Zhu, Y. Y., Rao, Y. J., Wang, Z. N., Jia, X. H., & Wu, H. (2013). Random fiber laser formed by mixing dispersion compensated fiber and single mode fiber. Optics Express, 21(7), 8544-8549.
[132] Zhang, H., Xiao, H., Zhou, P., Wang, X., & Xu, X. (2014). Random distributed feedback Raman fiber laser with short cavity and its temporal properties. IEEE Photonics Technology Letters, 26(16), 1605-1608.
[133] Wang, Z., Wu, H., Fan, M., Zhang, L., Rao, Y., Zhang, W., & Jia, X. (2015). High power random fiber laser with short cavity length: theoretical and experimental investigations. IEEE Journal of Selected Topics in Quantum Electronics, 21(1), 10-15.
[134] Babin, S. A., El-Taher, A. E., Harper, P., Podivilov, E. V., & Turitsyn, S. K. (2011). Tunable random fiber laser. Physical Review A, 84(2), 021805.
[135] Sugavanam, S., Yan, Z., Kamynin, V., Kurkov, A. S., Zhang, L., & Churkin, D. V. (2014). Multiwavelength generation in a random distributed feedback fiber laser using an all fiber Lyot filter. Optics express, 22(3), 2839-2844.
[136] DeMiguel-Soto, V., Bravo, M., & Lopez-Amo, M. (2014). Fully switchable multiwavelength fiber laser assisted by a random mirror. Optics letters, 39(7), 2020-2023.
[137] Bravo, M., de Miguel Soto, V., Ortigosa, A., & Lopez-Amo, M. (2015) Fully Switchable Multi-Wavelength Fiber Lasers Based on Random Distributed Feedback for Sensors Interrogation. Journal of Lightwave Technology, 33(12), 2598-2604.
[138] Zhu, Y. Y., Zhang, W. L., & Jiang, Y. (2013). Tunable multi-wavelength fiber laser based on random Rayleigh back-scattering. IEEE Photonics Technology Letters, 25(16), 1559-1561.
[139] Litago, I. A., Pérez-Herrera, R. A., Quintela, M. Á., López-Amo, M., & López-Higuera, J. M. (2016). Tunable dual-wavelength random distributed feedback fiber laser with bidirectional pumping source. Journal of Lightwave Technology, 34(17), 4148-4153.
[140] Wu, H., Wang, Z., Fan, M., Li, J., Meng, Q., Xu, D., & Rao, Y. (2018). Multiwavelength ytterbium-Brillouin random Rayleigh feedback fiber laser. Laser Physics Letters, 15(3), 035105.
[141] Ma, R., Rao, Y. J., Zhang, W. L., Wu, H., & Zeng, X. (2017, April). Broadband supercontinuum light source seeded by random distributed feedback fiber laser. In Optical Fiber Sensors Conference (OFS), 2017 25th (pp. 1-4). IEEE.
[142] Ma, R., Rao, Y. J., Zhang, W. L., Zeng, X., & Wu, H. (2018, March). Stable supercontinuum source based on random lasing. In 2nd Canterbury Conference on OCT with Emphasis on Broadband Optical Sources (Vol. 10591, p. 105910W). International Society for Optics and Photonics.
[143] Zhang, W. L., Li, S. W., Ma, R., Rao, Y. J., Zhu, Y. Y., Wang, Z. N., ... & Li, J. (2015). Random distributed feedback fiber laser based on combination of Er-doped fiber and single-mode fiber. IEEE Journal of Selected Topics in Quantum Electronics, 21(1), 44-49.

[144] Wang, L., Dong, X., Shum, P. P., & Su, H. (2014). Tunable erbium-doped fiber laser based on random distributed feedback. IEEE Photonics Journal, 6(5), 1-5.
[145] Sugavanam, S., Zulkifli, M. Z., & Churkin, D. V. (2015). Multi-wavelength erbium/Raman gain based random distributed feedback fiber laser. Laser Physics, 26(1), 015101.
[146] Huang, C., Dong, X., Zhang, N., Zhang, S., & Shum, P. P. (2014). Multiwavelength Brillouin-erbium random fiber laser incorporating a chirped fiber Bragg grating. *IEEE Journal of Selected Topics in Quantum Electronics*, *20*(5), 294-298.
[147] Song, J., Dong, X., Guo, Z., Xu, B., & Wang, D. (2018, October). Random Laser with Erbium-Doped Fiber and fs-Laser Introduced Random Fiber Grati
[148] Liu, Z., Yang, J., Bao, L., Shen, C., Huang, R., & Dong, X. (2018, October). Half-open cavity random fiber laser based on chirped-fiber Bragg grating array written in erbium-doped fiber. In 2018 Asia Communications and Photonics Conference (ACP) (pp. 1-3). IEEE.
[149] Wu, H., Wang, Z., Sun, W., He, Q., Wei, Z., & Rao, Y. J. (2018). 1.5 μm Low Threshold, High Efficiency Random Fiber Laser with Hybrid Erbium–Raman Gain. Journal of Lightwave Technology, 36(4), 844-849.
[150] Wu, H., Wang, Z., Fan, M., Li, J., Meng, Q., Xu, D., & Rao, Y. (2018). Multiwavelength ytterbium-Brillouin random Rayleigh feedback fiber laser. Laser Physics Letters, 15(3), 035105.
[151] Zhang, L., Xu, Y., Lu, P., Mihailov, S., Chen, L., & Bao, X. (2018). Multi-wavelength Brillouin random fiber laser via distributed feedback from a random fiber grating. Journal of Lightwave Technology, 36(11), 2122-2128.
[152] Wang, Z. N., Rao, Y. J., Wu, H., Li, P. Y., Jiang, Y., Jia, X. H., & Zhang, W. L. (2012). Long-distance fiber-optic point-sensing systems based on random fiber lasers. Optics express, 20(16), 17695-17700.
[153] Wang, Z., Jia, X., Rao, Y., Jiang, Y., & Zhang, W. (2012, January). Novel long-distance fiber-optic sensing systems based on random fiber lasers. In Third Asia Pacific Optical Sensors Conference (Vol. 8351, p. 835142). International Society for Optics and Photonics.
[154] Fernandez-Vallejo, M., Bravo, M., & Lopez-Amo, M. (2013). Ultra-long laser systems for remote fiber Bragg gratings arrays interrogation. IEEE Photonics Technology Letters, 25(14), 1362-1364.
[155] Wang, Z., Sun, W., Wu, H., Qian, X., He, Q., Wei, Z., & Rao, Y. (2016). Long-distance random fiber laser point sensing system incorporating active fiber. Optics express, 24(20), 22448-22453.
[156] DeMiguel-Soto, V., Leandro, D., & Lopez-Amo, M. (2018). Ultra-long (290 km) remote interrogation sensor network based on a random distributed feedback fiber laser. Optics express, 26(21), 27189-27200.
[157] DeMiguel-Soto, V., Lopez-Aldaba, A., Leandro, D., & Lopez-Amo, M. (2016, October). Ultra-Long random laser for remote real-time interferometric sensor monitoring using FFT analysis. In Asia-Pacific Optical Sensors Conference (pp. Tu3A-4). Optical Society of America.

[158] Leandro, D., deMiguel Soto, V., Perez-Herrera, R. A., Acha, M. B., & López-Amo, M. (2016). Random DFB fiber laser for remote (200 km) sensor monitoring using hybrid WDM/TDM. Journal of Lightwave Technology, 34(19), 4430-4436.
[159] Sugavanam, S., Tarasov, N., Shu, X., & Churkin, D. V. (2013). Narrow-band generation in random distributed feedback fiber laser. Optics express, 21(14), 16466-16472.
[160] Xu, J., Ye, J., Xiao, H., Leng, J., Wu, J., Zhang, H., & Zhou, P. (2016). Narrow-linewidth Q-switched random distributed feedback fiber laser. Optics express, 24(17), 19203-19210.
[161] Leandro, D., Rota-Rodrigo, S., Ardanaz, D., & Lopez-Amo, M. (2015). Narrow-linewidth multi-wavelength random distributed feedback laser. Journal of Lightwave Technology, 33(17), 3591-3596.
[162] Ye, J., Xu, J., Zhang, H., & Zhou, P. (2017). Powerful narrow linewidth random fiber laser. Photonic Sensors, 7(1), 82-87.
[163] Zhu, T., Chen, F. Y., Huang, S. H., & Bao, X. Y. (2013). An ultra-narrow linewidth fiber laser based on Rayleigh backscattering in a tapered optical fiber. Laser Physics Letters, 10(5), 055110.
[164] Leandro, D., deMiguel-Soto, V., & Lopez-Amo, M. (2016). High-Resolution Sensor System Using a Random Distributed Feedback Fiber Laser. Journal of Lightwave Technology, 34, 4596-4602.
[165] Wu, H., Wang, Z. N., Churkin, D. V., Vatnik, I. D., Fan, M. Q., & Rao, Y. J. (2014). Random distributed feedback Raman fiber laser with polarized pumping. Laser Physics Letters, 12(1), 015101.
[166] Lou, Z., Xu, J., Huang, L., Zhang, H., Leng, J., Xiao, H., & Zhou, P. (2017). Linearly-polarized random distributed feedback Raman fiber laser with record power. Laser Physics Letters, 14(5), 055102.
[167] Du, X., Zhang, H., Wang, X., Zhou, P., & Liu, Z. (2015). Investigation on random distributed feedback Raman fiber laser with linear polarized output. Photonics Research, 3(2), 28-31.
[168] Zhang, L., Wang, Y., Xu, Y., Zhou, D., Chen, L., & Bao, X. (2018). Linearly polarized multi-wavelength fiber laser comb via Brillouin random lasing oscillation. IEEE Photonics Technology Letters, 30(11), 1005-1008.
[169] Huang, L., Xu, J., Ye, J., Liu, X., Zhang, H., Wang, X., & Zhou, P. (2018). Power scaling of linearly polarized random fiber laser. IEEE Journal of Selected Topics in Quantum Electronics, 24(3), 1-8.
[170] Stolen, R. (1979). Polarization effects in fiber Raman and Brillouin lasers. IEEE Journal of Quantum Electronics, 15(10), 1157-1160.
[171] Babin, S. A., Zlobina, E. A., Kablukov, S. I., & Podivilov, E. V. (2016). High-order random Raman lasing in a PM fiber with ultimate efficiency and narrow bandwidth. Scientific reports, 6, 22625.

CHAPTER III

High resolution sensor systems

This chapter provides new applications of a random distributed feedback fiber laser to develop high resolution sensor systems. Several variations of the laser scheme are presented to perform high resolution temperature, strain and transversal load measurements. Then, a comparative study of several fiber optic sensors to measure cryogenic temperatures is carried out. Finally, a brief study of a distributed vibration sensor scheme based on ultra-weak FBGs is presented. A post-processing method which eliminates spectral shadowing is also developed, improving the performance of the system.[1]

---

[1]This Chapter has been partially published in the papers entitled: *High Resolution Sensor System Using a Random Distributed Feedback Fiber Laser* in Journal of Lightwave Technology, *Study of Optical Fiber Sensors for Cryogenic Temperature Measurements* in Sensors and *Spectral shadowing suppression technique in phase-OTDR sensing based on weak fiber Bragg grating array* in Optics Letters.

3.1. Introduction

Since the late 1970s, optical fibers have been proposed for sensing both physical and chemical parameters. The growing need to improve the performance of optical fiber sensors for industrial, civil work and aerospace applications has involved a lot of research and work since then [1]-[3].

From the point of view of the industry, fiber optic sensors (FOS) present several interesting qualities. They offer high sensitivity, dynamic range and reliability. Their packages are compact, lightweight and for some applications, they offer a competitive cost. In addition to these characteristics, their extraordinary resistance to high temperatures, corrosion, explosion hazards and their immunity to electromagnetic interference (EMI) allow their use in hostile environments. In these situations, traditional sensors such as electronic strain or capacitance gauges cannot operate properly. For all these reasons, FOS are the most suitable for solving these difficulties. They are key elements in improving industrial processes, quality control systems, medical diagnosis and control of anomalies.

FOS have demonstrated their ability to measure all the common parameters needed for controlling industrial processes and structures: temperature, strain, liquid level, flow, position and vibration among others [4]. What differentiates all these sensors is the method by which the parameter of interest modulates the light transmitted through the fiber, i.e. intensity, phase, polarization or wavelength modulation.

In general, the sensor´s response against a stimulus is characterized by two parameters which are closely connected: sensitivity and resolution. The sensitivity determines the degree of reaction of the sensor to physical or chemical variations. Then, the resolution sets the accuracy of this measurement. When monitoring any changes in a system, it is just as important to detect the smaller shifts as to detect them accurately. In order to control any process, high resolutions are desirable, especially when it comes to processes where a lack of accuracy can be a danger. FOS are characterized by their high sensitivity and resolution compared to other types of sensors [4]. Table 3. 1 shows a brief state of the art of high resolution fiber optic sensor systems. Temperature, strain and transversal load are the main parameters analyzed.

Year/Ref	Technology	Measured parameters	Max Resolution
1990/[5]	Thin film	Temperature	10^{-4} °C
1998/[6]	LPG	Strain	0.5 με
2006/[7]	OTDR	Temperature Strain	0.01 °C 0.1 με
2007/[8]	DBR fiber laser	Temperature Strain	0.05 °C 9.3 με
2008/[9]	FBG	Strain	$5x10^{-6}$ με/√Hz
2009/[10]	FBG-FPC	Temperature Strain	0.014 °C 0.11 με
2009/[11]	OTDR	Temperature Strain	0.01 °C 0.1 με
2010/[12]	FBG	Strain	$2.6x10^{-3}$ με
2010/[13]	Fabry- Pérot	Strain	10 με
2011/[14]	Fabry- Pérot PDH	Strain	$5.8x10^{-3}$ με
2015/[15]	DBR fiber laser	Strain Load	4.73 με $77x10^{-6}$ g
2016/[16]	**RDFB-FL**	**Temperature Strain**	**0.01 °C 0.2 με**
2016/[17]	**RDFB-FL**	**Load**	**1 g**
2017/[18]	Fabry-Pérot	Temperature	0.12 $x10^{-9}$ °C
2017/[19]	Heterodyne spectroscopy	Temperature	5.5 $x10^{-6}$ °C
2018/[20]	Heterodyne spectroscopy	Temperature	0.005°C
2018/[21]	Fabry-Pérot	Temperature Strain	0.1°C 0.8 με

Table 3. 1. State of art of high resolution fiber optic sensor systems.

Cryogenic temperature systems are becoming more important in the energy sector, transportation, and medical technology. It is essential to guarantee a safe operation of the systems in these areas providing continuous monitoring of the temperature. However, monitoring at cryogenic temperatures requires greater care than equivalent measurements at room temperature, due to thermal problems of sensor placing and heat sinking.

For the majority of cryogenic sensing measurements, resistive, diode, and thermocouple based sensors are commonly used [22]. Although FOS offer many advantageous properties, their low intrinsic thermal sensitivity at low temperatures [23] is a main drawback, limiting their utilization at cryogenic temperatures.

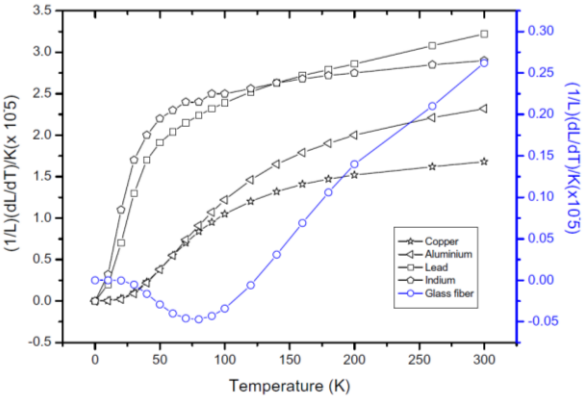

Figure 3. 1. Thermal expansion coefficient of materials. Graph extracted from [23].

To overcome this limitation, FBGs have been widely used [23]-[26] but embedded in (or bonded) to substrates with larger thermal expansion coefficients than silica fibers, which increase their sensitivity. In Table 3. 2, a brief state of art of FOS for measuring cryogenic temperatures is shown. Although these techniques significantly increase the sensitivity with temperature, the flexibility of the optical fiber drops since the sensor is bonded to a rigid substrate.

Contrary to FBG sensors, which can be considered as point fiber optic sensors, distributed fiber optic sensing presents unique characteristics over other conventional sensing techniques. The ease to measure temperature and strain continuously along a single fiber is particularly interesting for monitoring large structures, such as pipelines, flow lines, oil wells, and dikes [37], but also for structural health monitoring [38]. A few applications using distributed sensors at cryogenic temperatures have been developed lately. A distributed liquid level sensor for liquid nitrogen and helium tanks was developed in [39]. In addition, a Brillouin distributed sensor monitored the

temperature of the supra-conductive magnets in CERN Laboratory (Geneva) [40], and MilliKelvin resolution was reached in [41].

Year/Ref	Technology	Sensitivity (pm/°C)	Temperature (°C)
2001/[27]	Teflon-bonded FBG	39	-196
2006/[28]	Pressurized FBG	24	Below -73
2008/[29]	Indium–coated FBG	15	-258
2011/[30]	LPG	60	-185
2011/[31]	PMMA-coated FBG	37.69	-178 to -123
2012/[32][9]	ORMOCER-coated FBG	2.4	-223 to 26
2015/[33]	Phase-shifted LPG	30	-223 to 26
2016/[34]	Indium-coated FBG	50.8	-223 to 25
2017/[35]	Lead-coated FBG Indium-coated FBG	22 28	-268 to-223
2018/[36]	Polymer resin-coated FBG	48	-180 to 25

Table 3. 2. State of art of cryogenic fiber optic sensors based on FBG.

This chapter provides new applications of a random distributed feedback fiber laser (RDFB-FL) to develop high resolution sensor systems. In section 3.2, a system based on this type of lasers is proposed for high resolution temperature sensing at different temperature ranges. Subsequently, variations of this structure are presented to perform high resolution strain and transversal load measurements. The strain and transversal load sensors are shown in sections 3.3 and 3.4 respectively. Within section 3.2, a comparative study of several FOS to measure cryogenic temperatures is carried out. In section 3.5, a brief study of a distributed vibration sensor scheme based on ultra-weak FBGs is presented. A post-processing method which eliminates spectral shadowing is also developed, improving the performance of the system.

3.2. High resolution temperature systems

In the first part of this section, a high resolution temperature system based on a RDFB-FL is demonstrated. The particular properties of these lasers are exploited to interrogate a π-phase shifted fiber Bragg grating (PS-FBG, Chapter II section 2.1.2) as a temperature sensor. The modeless behavior of the laser delivers high frequency stability because of the distributed cavity, obtaining a measured temperature resolution under 0.01 °C.

The second part shows a study of different optical fiber sensors for cryogenic temperature measurements. A distributed sensor, several interferometric and FBG-based fiber optic sensors are analyzed, comparing their advantages and drawbacks.

3.2.1. High resolution temperature system based on a RDFB-FL

a. Description of the system

The proposed setup in Figure 3. 2 is a modified version of a forward-pumped RDFB-FL, previously described in Chapter II section 2.2.4.

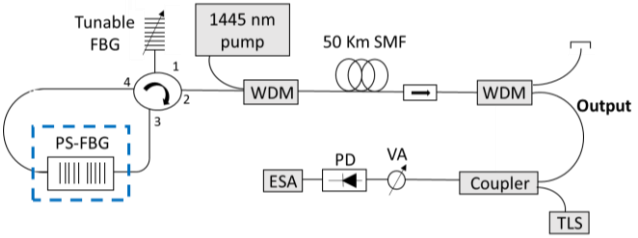

Figure 3. 2. Experimental setup of the proposed laser for temperature measurements.

A laser cavity consists of reflectors or a loop that recirculates light into a gain media. The first reflector in our system is a distributed mirror along 50 Km of SMF, providing a weak feedback due to Rayleigh scattering. A wavelength division multiplexer (WDM) injects the pump laser power (IPG RLD 3-1445) into the fiber, which acts as the active medium for the Raman amplification induced by the stimulated scattering effect (see Chapter II section 2.1.3). A fiber loop composes the second reflector, which collects the back-scattered

(and amplified) light and re-injects it into the cavity. Light enters into the loop mirror through the port 2 of a four-port optical circulator.

The typical line-width of an RDFB-FL without filtering is several nanometers wide [42]. Since a narrower laser line is required in this scheme, various filtering elements are employed. The main purpose of this loop is to allocate these filtering elements. Two different types of FBGs operate together to achieve this: a PS-FBG and a tunable FBG. The transmitted central peak of the PS-FBG filtered with a tunable FBG selects and narrows the emission line, as displayed in Figure 3. 3.

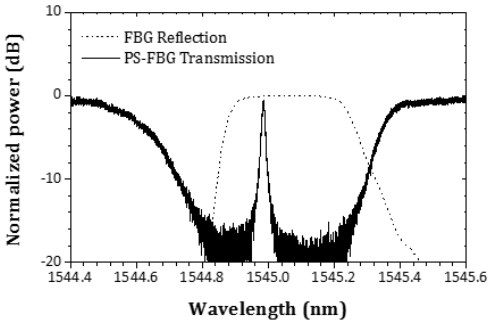

Figure 3. 3. Filtering spectrum given by the tunable and the phase-shifted fiber Bragg gratings.

It must be noted that the PS-FBG is working in transmission and the tunable FBG in reflection. The full width at half maximum of the tunable FBG is 0.35 nm and it is located at the port 3 of the optical circulator. The PS-FBG is the sensing element of the set-up, acting as a filter and as a sensor at the same time. Its wavelength transfer function is shifted with temperature. As a result, temperature variations can be measured by tracking the wavelength of the emission line of the laser. It should be noticed that the role of the tunable FBG is just to filter the transmission peak of the PS-FBG and has not influence on the sensing process.

An isolator is placed at the output of the laser to avoid undesired reflections that could destabilize it. Finally, a WDM 1550/1445 is located after the isolator to remove the residual pump power from the cavity. Although the output of the laser can also be located at the header, it is established at the end of the fiber cavity. At this point, a higher peak power emission line is obtained, enhancing the detection process.

Heterodyne detection technique

In order to obtain a higher resolution in the measurements, a heterodyne detection process is chosen to monitor the PS-FBG wavelength shift. This method was previously proposed in [43], where a narrow erbium-doped fiber single longitudinal mode laser was beaten and detected in the electrical domain.

The resolution given by electrical devices, such as an electrical spectrum analyzer (ESA), is several orders of magnitude higher than the given by optical spectrum analyzers (OSA). To take advantage of this, an external tunable laser source (TLS), with a line-width of 100 kHz, is mixed with the output signal of the laser using an optical coupler. The combined signal is detected by a 12 GHz bandwidth photodetector and measured by the ESA. In order to protect the photodetector, a variable attenuator limits the received power at its input.

Using this technique, the detected beat signal will be placed at a frequency given by the difference between the TLS and the frequency of the laser. If the TLS is positioned at a frequency shifted from the emission line, a beat signal located at this frequency difference will be detected within the ESA. Since the TLS remains steady at a set frequency, any variation in the frequency of the electric beat signal will be caused by a temperature change in the PS-FBG.

RDFB-FL are especially suited for their use in combination with the heterodyne detection technique, taking advantage of their mode-less behavior (Chapter II, section 2.2.3). If heterodyne detection is applied with conventional fiber lasers, the maximum resolution is limited by the intermodal distance between the longitudinal modes. From the theory, the lasing longitudinal modes of a fiber laser are fixed by the cavity and they are spaced by the intermodal distance. Since the cavity length in RDFB-FL is indefinite, it does not limit the maximum resolution of the system.

b. Experimental results

Let us first start with the RDFB-FL optical spectrum, shown in Figure 3. 4. The output spectrum was measured with the external TLS switched OFF. A signal-to-noise ratio of more than 40 dB was reached with a peak power of 11 dBm and a line width of 4 pm.

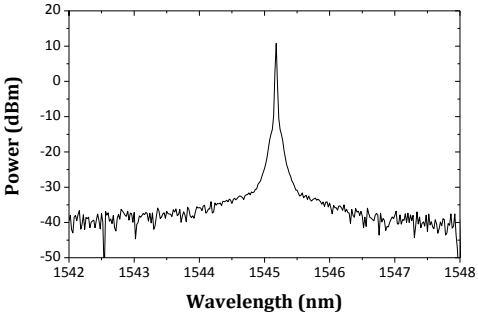

Figure 3. 4. Optical spectrum of the RDFL used for temperature sensing.

Two initial experiments were carried out to demonstrate that the emission line obtained corresponds to a RDFB-FL. First, the variation of the peak power with the increasing pump power was measured, see Figure 3. 5. An abrupt power increase is noticeable at 1.32 W, corresponding to the lasing threshold of the system.

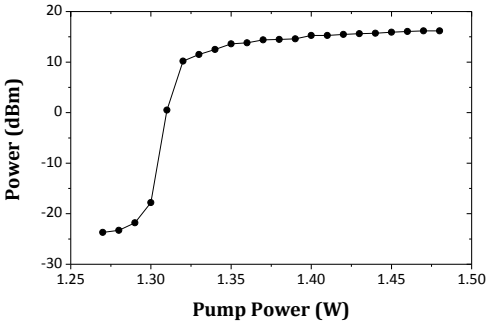

Figure 3. 5. Study of the output power vs pump power injected for the temperature sensor system.

Secondly, the lack of longitudinal modes was verified by observing the self-heterodyne signal of the laser in the electrical domain. Figure 3. 6 presents the self-beating electrical spectrum of the laser measured with the ESA (black line). The distributed nature of the cavity is demonstrated by the continuous spectrum measured at any resolution. Otherwise, longitudinal-modes (peaks) would arise. The noise floor of the detector is also represented (grey line) in the same figure to avoid any misunderstanding due to the continuous spectrum of the random laser.

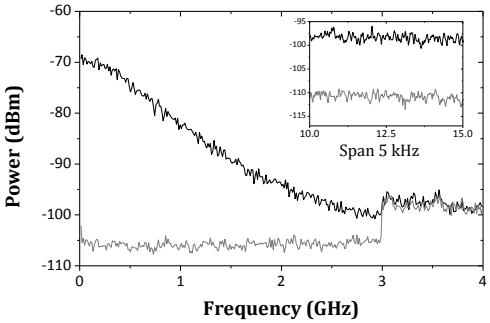

Figure 3. 6. Electrical spectrum of the laser´s self-beating for different spans (4 GHz and 5 kHz inset) and resolutions (10 MHz and 300 Hz inset) in the temperature sensor setup (black line). Noise floor of the detector (grey line).

After verifying the adequate behavior of the system as a RDFB-FL, the high-resolution temperature measurements were carried out. In order to determine the response of the sensor to temperature, it was placed in a climatic chamber. During the temperature increase in the chamber, the peak frequency of the beat signal was monitored. Figure 3. 7 shows an example of the electrical spectrum of the beat signal detected with the ESA. The obtained results are presented in Figure 3. 8, obtaining a linear temperature sensitivity of 0.837 GHz/°C.

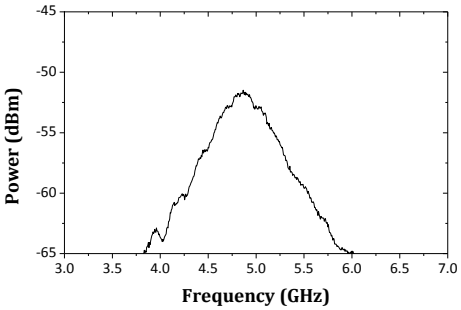

Figure 3. 7. Electrical spectrum of the beat signal received.

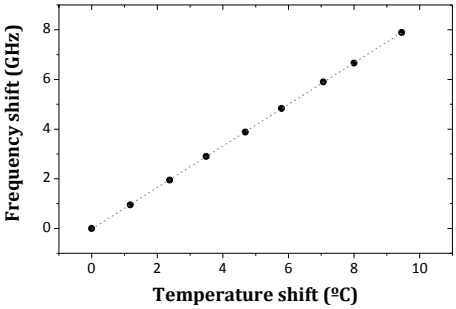

Figure 3. 8. Frequency shift of the PS-FBG with temperature.

To demonstrate that the developed system is valid for high resolution temperature measurement, an additional experiment was performed. In this test, the PS-FBG sensor was placed inside a partially isolated chamber, so the temperature change is minimized. This action was necessary to obtain a sufficient temperature control in the measurement process. A reference probe with a maximum resolution of 0.01 °C was placed together with the PS-FBG inside the chamber. A slow increase in temperature induced by different temperatures between the chamber and the laboratory was measured. The reference temperature given by the probe and the frequency shift of the beat signal were recorded for 10 min, every 5 s and 30 s, respectively. In the experiment, the frequency resolution of the ESA was 1.5 MHz. However, this factor did not limit the performance of the system since the maximum resolution of the ESA is 1 Hz.

The frequency shifts of the beat signal were converted to temperature variations using the previously measured sensitivity (0.837 GHz/°C). In this manner, the results acquired with both systems can be compared. From Figure 3. 9, we can infer that the proposed technique using a PS-FBG in a RDFB-FL surpasses the probe resolution of 0.01 °C.

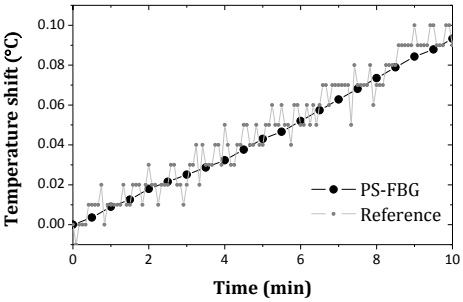

Figure 3. 9. Temperature measured by the PS-FBG (black) and a reference sensor (grey).

Given the values of sensitivity and resolution, a frequency stability study would complete the characterization of the RDFB-FL system. However, it cannot be directly measured due to its dependence on temperature. From the experimental results, a frequency instability lower than 8.37 MHz can be inferred. In the present study, a maximum temperature variation of 10 °C has been measured. The temperature range of the system is limited by the photodetector's bandwidth. As a result, this range can be selected by choosing a suitable photodetector. Another option for increasing the temperature range could be to tune the external TLS, although the accuracy of this device should be taken into account in the measuring process.

3.2.2. Study of optical fiber sensors for cryogenic temperature measurements

In the following section, the performance of four different fiber optic sensors at cryogenic temperatures is examined. The RDFB-FL system presented in the previous section is also tested for cryogenic temperatures measuring. In addition, four more fiber optic sensors were attached in the same cryogenic set-up to offer a broader comparative study. A photonic crystal fiber (PCF) Fabry-Pérot interferometer and two Sagnac interferometers complete the group of sensors analyzed. Additionally, their behavior is compared with a classical FBG sensor and a distributed sensor based on a commercial optical backscatter reflectometer.

The outline of this subsection is as follows: a description of the sensors is provided, followed by a detailed explanation of the experiment to obtain

cryogenic temperatures. Then, a comparison of all the analyzed sensors is carried out and future work improvements are proposed.

a. Description of the sensors

Interferometric fiber optic sensors

We will briefly define the technique used to interrogate the interferometric sensors before entering into their detailed description. The technique is based on the fast Fourier transform (FFT) of the optical spectrum as in [44]. This approach was selected due to the higher resolution offered if compared to conventional techniques, such as monitoring the wavelength shift of a fringe of the interference. A commercial interrogator (SM125, SMARTEC) is used to monitor the response of the sensors. The FFT of the measured optical spectrum is computed every second by using Matlab, offering real-time information of the sensor system. Each sensing element is represented by a component located at a certain spatial frequency in the FFT. Temperature changes can be monitored by tracking the corresponding FFT phase in the spectrum.

PCF-FP

The PCF Fabry-Pérot interferometer, see Chapter II Section 2.1.2, is formed of a linear cavity made by splicing a standard single mode fiber to a four-bridge double-Y-shape-core micro-structured optical fiber (MOF), shown in Figure 3. 10. The MOF is cleaved at the other end, obtaining a cavity length of 570 µm [45].

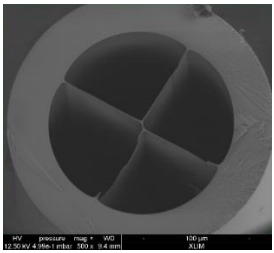

Figure 3. 10. Four-bridge double-Y-shape-core microstructured optical fiber (MOF).

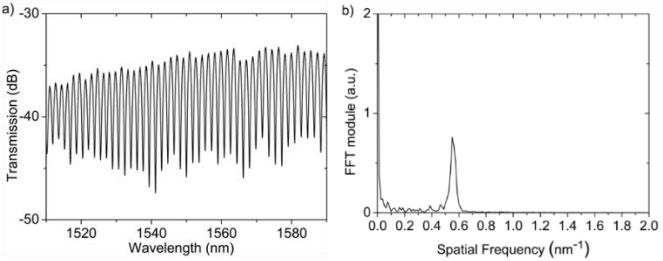

Figure 3. 11. Fiber based Fabry-Pérot (PCF-FP) sensor: (a) Optical spectrum and (b) its fast Fourier transform (FFT) module.

The optical spectrum of the PCF-FP and its Fast Fourier transform (FFT) are shown in Figure 3. 11. During the experiment, the FFT phase corresponding to the spatial frequency located at 0.575 nm^{-1} was monitored.

Sagnac interferometers

Both of the Sagnac interferometers consist of a high-birefringence fiber loop mirror fully made of polarization-maintaining (PM) Panda fiber, Chapter II Section 2.1.2. Their design is based on [44], using the three section analysis. They comprise two PM fibers fused to the sensing fiber with a 45° rotation angle offset. These fibers act as communication channels. In the first interferometer (Sagnac 1), the communication fibers present a length of 0.97 and 0.61 m each, while the sensing fiber is 0.57 m long. The communication fibers that are used in Sagnac 2 have the same length (0.3 m), while the sensing fiber is 0.45 m long.

The optical spectra of the Sagnac interferometers and their FFT are shown in Figure 3. 12. In the case of Sagnac 1, several components are generated in the FFT magnitude spectrum, corresponding to the sensing fiber, the virtual section given by the different length of the communication fibers and their combination [44]. In the second case, with Sagnac 2, the contributions of the communication fibers are suppressed. As a result, only birefringence changes on the sensing fiber are detected. The temperature measurement is retrieved by monitoring the contributions given by the sensing fibers. Then, the FFT phases located at 0.125 nm^{-1} and 0.1 nm^{-1} were tracked for Sagnac 1 and 2, respectively.

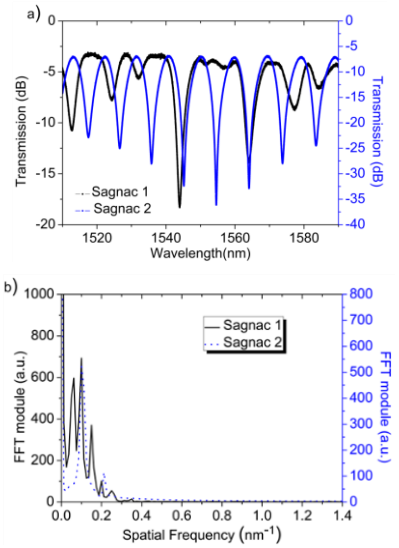

Figure 3. 12. Sagnac interferometers: (a) Optical spectrum and (b) its FFT module.

FBG-based fiber optic sensors

PS-FBG in RDFB-FL configuration

As previously stated, the system presented in Section 3.2.1 was tested to measure cryogenic temperatures. The original scheme was slightly adapted to satisfy the requirements of the new experiment. In particular, the fiber loop at the laser header was modified as shown in Figure 3. 13. The tunable FBG which filters the transmission spectrum of the PS-FBG was replaced by a programmable filter (Wave Shaper Finisar 1000S) with a tunable band-pass of 0.1 nm. It was inserted in the fiber loop, in series before the PS-FBG. It should be noted that the position of the programmable filter inside the fiber loop, before or after the PS-FBG, does not affect the final emission line.

Both elements, programmable filter and tunable FBG, perform exactly the same function. The first one presents higher insertion losses, although this does not prevent from laser generation. The aim for this variation is to facilitate taking measurements over a wider temperature range. It should be noticed that if the temperature change is high enough, the transmission peak of the PS-FBG will leave the bandwidth of the band-pass filter. As a result,

laser generation will cease. In order to avoid this, the central wavelength of the filter must move according to the displacement of the PS-FBG transmission peak. In this experiment, a wide range of temperatures is measured, from -160 to 80 °C. Although the tunable FBG could be also employed, the modified scheme with a programmable filter facilitates the measuring process.

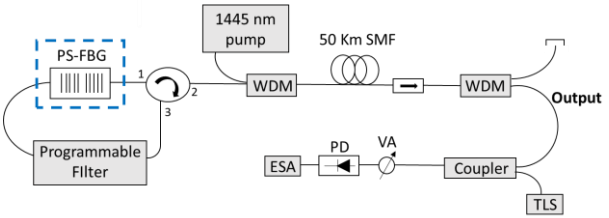

Figure 3. 13. Schematic diagram of the proposed random distributed feedback fiber laser (RDFB-RL) using a π-phase shifted fiber Bragg grating (PSFBG) sensor.

Commercial FBG

A commercial FBG with no coating was chosen to act as a reference. FBGs are representative wavelength selective sensors whose behavior at cryogenic temperatures were previously studied and is widely known [23]-[33]. Comparing its behavior to the ones obtained with the other sensors gives a notion of the reliability of their performance as cryogenic sensors. Its central wavelength, 1544.9 nm at room temperature, was directly monitored every second employing the FBG interrogator.

Distributed Sensing Using an OBR

Distributed temperature measurements were obtained using a three-meter long SMF fiber and a commercial OBR (OBR 4600, LUNA TECHNOLOGIES) whose operation is based on optical frequency domain reflectometry [46]. The OBR uses swept wavelength interferometry (SWI) [47] to measure the Rayleigh backscatter as a function of length with ultra-high spatial resolution (10 µm in a span of 30 m) and a backscatter-level sensitivity. If an external stimulus is applied to the sensing fiber, like a variation in temperature or strain, spectral and temporal shifts in the Rayleigh backscatter pattern are induced. When using the OBR for distributed temperature and strain measurements, the device is able to measure these shifts in a span of 70 m,

with a spatial resolution of 1 cm. Then, it scales them, giving a distributed temperature or strain measurement, with 0.1 °C and 1 με resolutions, respectively.

An example of the reflected signal detected by the OBR that is used in the experiments is shown in Figure 3. 14. The fiber is placed in an Expanded Polystyrene (EPS) box used for measurements that is fully described in 3.2.2.b. Different sections of the fiber under study can be identified: the first two meters correspond to the pigtail connected to the OBR. Then, a reflection peak at 2 m. determines the position of the first connector and the beginning of the sensing fiber, which ends at 5.2 m. The zone located inside EPS box is framed in blue (from 2.8 m to 3.9 m). Finally, the region where the fiber is rolled upwards a copper cylinder, located inside the box and which has a total length of around 38 cm, is highlighted in red color.

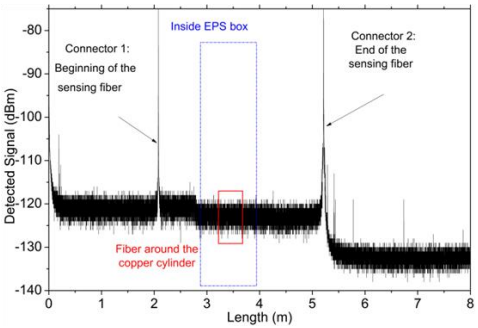

Figure 3. 14. Trace detected by the optical backscatter reflectometer (OBR).

b. Description of the experiment

The purpose of the experiment is to prove the feasibility of using different FOS to measure cryogenic temperatures. In fact, one of the analyzed sensors was not been previously used for this intent, such as the PCF-FP. As discussed above, sensitivity is significantly reduced at cryogenic temperatures due to the low thermal sensitivity of fiber. The PS-FBG in a RDFB-FL scheme [16] and the Sagnac interferometers [48] have demonstrated high resolutions at room temperature, 0.01 °C and 6.2 × 10-4 °C, respectively. Despite the reduction in sensitivity, their high resolution could make them suitable to perform measurements at low temperatures.

The scheme used to attain cryogenic temperatures is shown in Figure 3. 15. It consists of an Expanded Polystyrene (EPS) box and a solid copper cylinder, located inside the box. A solid copper cylinder was selected because of its high thermal conductivity. Its diameter and height are 4 cm and 5.2 cm, respectively. In order to have an effective transmission of the temperature, the point sensors were fixed on top of the cylinder, directly in contact with the copper. Due to their length, the Sagnac interferometers were coiled around the top part of the cylinder, as seen in Figure 3. 15. All of the sensors were analyzed simultaneously in this work. A thermocouple type K was placed next to the sensors to provide a temperature reference in real-time. That thermocouple was connected to a data acquisition system and temperature was recorded every second. The FBG and all of the interferometric sensors were interrogated by the commercial FBG interrogator, Smartec SM125, with a spectral range from 1510 to 1590 nm, a scan frequency of 1 Hz, and a resolution of 5 pm.

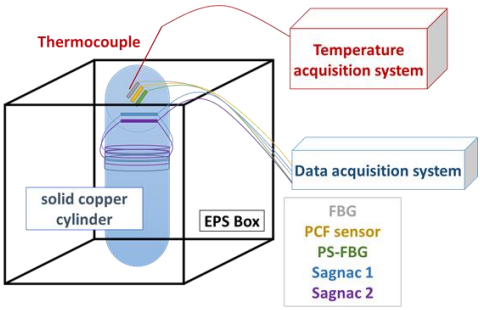

Figure 3. 15. Schematic setup for cryogenic measurements.

In order to study the temperature distribution along the copper cylinder and to have a clear view of the temperature differences inside the setup, distributed measurements were carried out. Since the transmission of temperature in the copper cylinder is not perfect, several points at different heights were chosen to verify the temperature variations along the cylinder, taking into account that lower temperatures are expected at the point that is closest to liquid nitrogen. The SMF fiber that was used for distributed sensing was rolled upwardly around the copper cylinder in four loops, as it is shown in Figure 3. 16. Four measurement points were selected (R1 to R4), forming a vertical line, R1 being at the lowest position (closer to the liquid nitrogen) and R4 at the highest one.

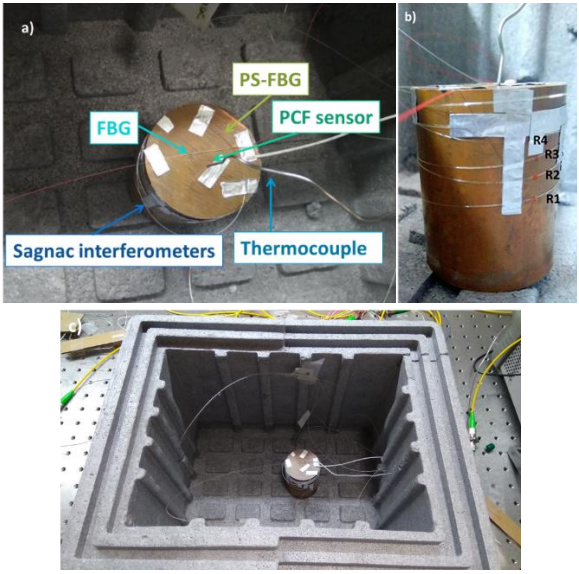

Figure 3. 16. Photographs of the setup: (a) placement of the sensors used in the experiment (b) placement of the fiber used for distributed measurements and (c) EPS box and copper cylinder.

With the aim of characterizing the behavior of the sensors, a temperature sweep was performed at higher temperatures. For this purpose, the copper cylinder was located inside a climatic chamber Binder FD23 together with the sensors, measuring the temperature range between room temperature and 80 °C.

Cooling process

A simple technique was used to decrease the temperature of the sensors to cryogenic temperatures. The EPS box was partially filled up with pure liquid nitrogen, so that the liquid did not reach the sensors. In this manner, the temperature of the copper cylinder gradually decreased. The sensors were placed on the top part of the copper cylinder, having a homogenized temperature on its surface. Since the sensors were located close to each other, a single thermocouple was used as the temperature reference for all of them.

After adding the liquid nitrogen, the box was covered to avoid the condensation around the sensors, temperature gradients and also to reduce as much as possible the evaporation rate of the nitrogen, which would lead to fast temperature changes. This fact was verified after several tests. Following this procedure, a stable temperature of -160°C was achieved. Although liquid nitrogen's boiling temperature is -195.8°C at one atmosphere, the copper cylinder could not reach such a temperature because the box was not perfectly isolated. Furthermore, the transmission of the temperature in the copper cylinder is not ideal. To reach such temperatures, all of the sensors should be submerged in liquid nitrogen, which could damage the sensors in some cases.

When the box is filled with liquid nitrogen, the temperature decreases and remains at around -160°C until all of the nitrogen is evaporated. This process can take several hours. Once the liquid nitrogen is fully evaporated, the temperature rises until it reaches the room temperature, at around 100°C/h. Measurements were carried out during the heating process of the copper cylinder, since it is a gradual process without sudden temperature changes.

Even though the previous experiment provides an idea of the response time of the sensors, an additional test was carried out to offer an approximate numerical value for the response time of each sensor. In this simple test, the EPS box was filled with liquid nitrogen, which boiling temperature is -195.8°C, and the sensors were submerged in the liquid. All of them were interrogated by the commercial FBG interrogator, using a scan frequency of 2Hz. In this manner, the time it takes for each sensor to respond to the change in temperature (200°C temperature gradient) was measured.

c. Experimental results

Characterization at temperatures below 0°C

The results of the characterization of the sensors from –160°C to 0°C are shown in Figure 3. 17 (a), for all of the interferometric sensors, and in Figure 3. 17 (b), for both FBG-based optical fiber sensors. The measured data is represented as a function of the temperature given by a thermocouple type K, which has a standard limit error of ± 2.2°C.

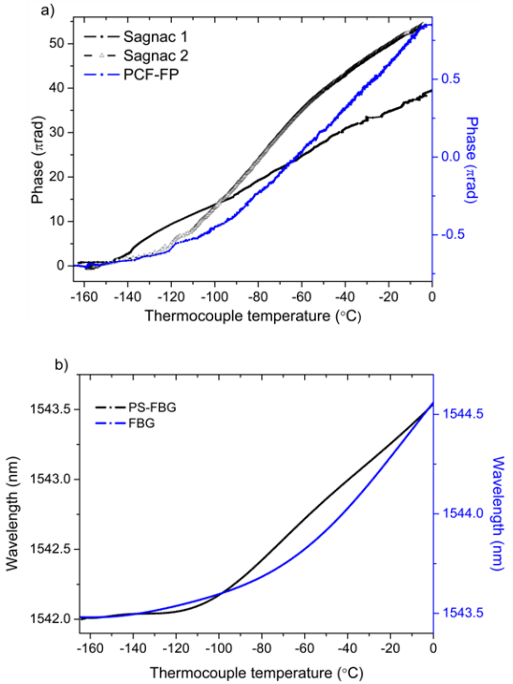

Figure 3. 17. (a) Interferometric, (b) FBG-based fiber optic sensors response versus temperature.

Figure 3. 18 provides the results obtained in the secondary experiment. The point sensors like the FBG, the PS-FBG and the PCF-FP present similar response times, approx. 3 s with a temperature gradient of more than 200 °C. The Sagnac interferometer sensor presents a longer response time, around 15 s. In order to compare their performance as cryogenic sensors, a summary table gathering some relevant features is displayed in Table 3. 3. Sensitivity, resolution and response time are analyzed.

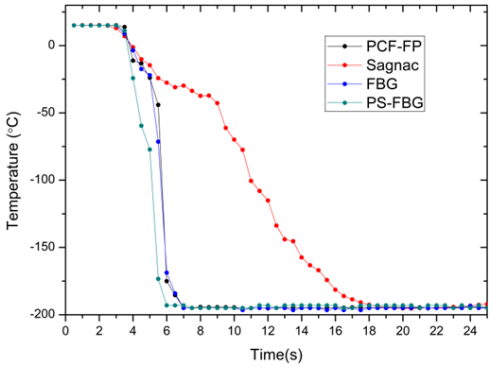

Figure 3. 18. Response time of the sensors.

Type of Sensor	Sensor	Sensitivity above –100 °C	Resolution above –100 °C	Response time (200 °C gradient)
FBG-based	Commercial FBG	11.6 pm/°C	0.4 °C	~3 s
	PS-FBG random laser	9.5 pm/°C	0.21 °C	~3 s
Interfero-metric	PCF Fabry-Pérot	0.0147 π rad/°C	1.15 °C	~3 s
	Sagnac 1	0.185 π rad/°C	0.38 °C	~15 s
	Sagnac 2	0.4023 π rad/°C	0.1 °C	~15 s

Table 3. 3. Summary of the results.

From the results shown in Figure 3. 17, it can be inferred that all the sensors except the Sagnac interferometers present similar behavior with temperature. From 0 °C to -100 °C, a linear trend is observed. From -100 °C to -160 °C, the slopes of the curves are significantly reduced with an exponential decay, becoming almost flat at -160 °C. The fast reduction of the coefficient of thermal expansion below -100 °C [23] justifies this fact, leading to lower sensitivities and resolutions in the measurements. Concerning the Sagnac interferometers, two main linear trends are distinguished. This performance

is caused by the slow response of the sensor (see Figure 3. 18) and the likely coupling of some axial strain, due to the copper cylinder expansion with the increasing temperature. In Figure 3. 17 (a), where the response of both Sagnac is represented, the effect of the possible parasite strain due to the thermal expansion of the cylinder has not been compensated.

Characterization at temperatures above 0 °C

The results of the characterization of the sensors from 0 °C to 80 °C are shown in Figure 3. 19 for the FP-PCF and for both FBG-based optical fiber sensors. However, the performance of the Sagnac interferometers is not included. The measurements in the climatic chamber were not performed under the same conditions with regard to the placement of the sensors that are coiled around the cylinder. The inherent characteristics of the materials that are employed in the experiment did not allow for achieving identical placement conditions. A different location of the sensors would lead to the generation of a parasite strain related with the expansion of the cylinder, altering the measurements. For this reason, we decided not to include that results.

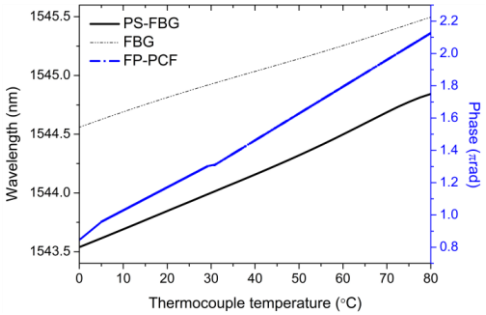

Figure 3. 19. Fiber optic sensors response versus temperature above 0 °C.

Distributed Temperature Measurements

Distributed measurements were carried out in a total span of 3 m, with a spatial resolution of 1 cm using a 3 m length SMF fiber and Luna's Distributed Temperature and Strain Software. The SMF fiber was rolled upwards the copper cylinder, in order to determine how the temperature varies at different heights of the cylinder. Some examples of the distributed temperature traces taken during the heating of the cylinder are shown in Figure 3. 20 represented in different colors. The temperature evolution of the four reference points along the distributed sensing fiber is represented in

Figure 3. 21. Despite the good thermal conductivity of the copper cylinder, the zones of the sensing fiber that are closer to the liquid nitrogen were expected to experience lower temperatures. Different sections can be identified in Figure 3. 20: the section outside the EPS box is located from 2.5 m to 2.8 m and from 3.9 to 4.5 m. The temperature in this zone remains stable at an ambient temperature (around 25 °C). The area after 2.8 m is located inside the EPS box, but it is not in contact with the copper cylinder. Nevertheless, it detects the decrease of temperature inside the box, which is almost constant in every point. Finally, the four reference points are located from 3.2 m to 3.6 m, which are in direct contact with the copper cylinder. In this last section, peaks and valleys are observed in specific points, which amplitudes increase at lower temperatures. Since the sensing fiber is attached with aluminum tape to the cylinder (Figure 3. 16), parasitic strain may be applied at these points of the fiber, originating a noisy profile. However, the shape of the traces remains constant at the four reference points, whose temperature trend was monitored and is represented in Figure 3. 21.

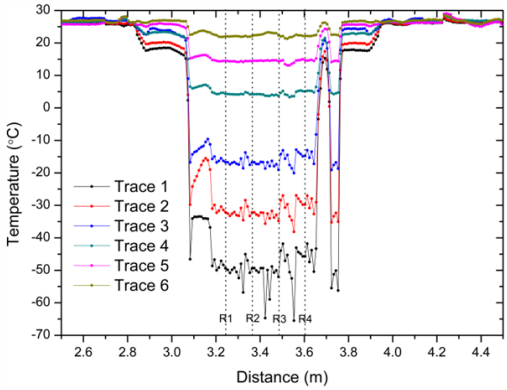

Figure 3. 20. Example of optical backscatter reflectometer (OBR) traces: distributed temperature sensing. R1 to R4 represent the reference points (see also Figure 3. 16 (b)).

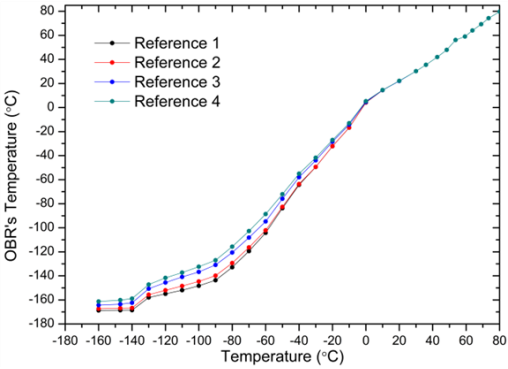

Figure 3. 21. Temperature evolution at the reference points measured with the OBR versus thermocouple temperature.

From the multiple experiments carried out, several key factors that are worth mentioning were noted when measuring cryogenic temperatures. Firstly, the response time of the sensors is directly related to the size of the sensor and the presence or absence of coating. The Sagnac interferometers present a much higher response time, mainly because they are ten times longer than the other sensors (which can be considered as punctual sensors). All of the sensors lack of coating except the Sagnac interferometers. As a consequence, the last ones present a higher response time. Moreover, it has been noticed a direct influence on the results related to the placement of Sagnac interferometers in the setup: the number of turns around the cylinder, the strain caused by the adhesive tape that holds the sensors, the overlap of the fiber turns one on top of another, etc. All these aspects affect the results and need to be considered when using this type of sensors in practical applications at cryogenic temperatures.

In terms of the sensitivity and resolution, Sagnac interferometers offer greater sensitivity and resolution than PCF-FP because of their higher length. Their sensing capability is based on the phase shift generated by the high-birefringence fiber, which is directly related with the fiber length. Then, longer fiber lengths generate larger phase shifts, i.e. higher sensitivities. As a consequence, higher temperature resolutions can be attained employing the same interrogation equipment [48]. However, the use of these sensors at cryogenic temperatures is extremely affected by the placement of the sensing fiber. This fact limits their use, not being the most suitable sensors for

reduced spaces because of the large curvatures to which the fiber is subjected.

On the other hand, the size of the PCF-FP allows its use in compact spaces and its location does not significantly affect the measurements, giving the temperature of a single point at a time. Its properties, like the absence of coating and size, give a significantly lower response time to the detriment of the sensitivity and endurance. The condensed vapor inside the sensor may solidify at cryogenic temperatures and cause the breakage of the photonic crystal fiber or modify the interference that occurs in the FP cavity, thus avoiding its use.

With regard to the FBG-based fiber optic sensors, the PS-FBG used in a RDFB-FL configuration and the FBG present comparable sensitivities. This fact is intrinsically related to the properties of the gratings used and independent from the interrogation technique. Using the heterodyne detection technique of the narrow RDFB-FL, two times higher resolution is obtained. Below -160 °C, the sensitivity of both the gratings is expected to decrease, and so increase the error in the measurement when using a commercial interrogator. On the contrary, if the heterodyne-based technique in the electrical domain is used, temperatures below -160 °C are expected to be accurately measured. In future works, these results could be improved simply by automating the measuring method employed, since is a limiting factor in dynamic measurements. It should be noticed that enhanced resolution at ultra-low temperatures could be obtained if this measurement technique is combined with coatings and substrates applied to the gratings [25]-[29].

Regarding the distributed measurements, the results confirmed the expected behavior. Point R1, which is located in the lowest position around the cylinder, experienced the lowest temperature, and as the distance from the nitrogen increases, the temperature also increases. When comparing the OBR's temperature traces with the temperature given by the thermocouple, which is closer to Reference 4, a similar behavior is observed when compared to the sensors analyzed previously. From room temperature to -100 °C all of the curves follow a linear trend. Then, the slope of the curves is reduced and below -140 °C almost any change in temperature is detected. Improved measurements could be obtained by adjusting the scaling coefficients that are used in the Luna's OBR software for distributed temperature measurements.

3.3. High resolution strain system

This section proposes a scheme for axial high resolution strain measurements. As in the previous system for high resolution temperature measurements, two emission lines are generated and beaten between them. In this approach no external source is required and the detected signal in the electrical domain reflects the strain variations, and self-compensating is possible when temperature changes. The strain resolution attained in this setup is under 0.2 με.

a. Description of the system

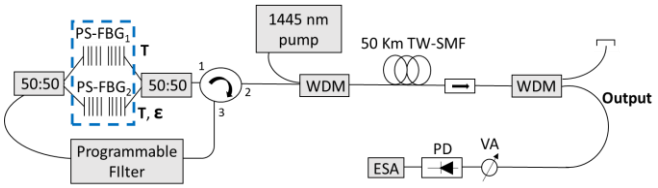

Figure 3. 22. Experimental schematic of the proposed laser for strain measurements.

Fiber Bragg gratings not only react to temperature variations but also to axial strain changes. For this reason, axial strain cannot be measured directly due to the influence of temperature. Figure 3. 22 shows the proposed scheme to avoid temperature crosstalk and achieve high resolution strain monitoring. Two emission lines are generated by two twin phase-shifted FBGs (PS-FBG_1 and PS-FBG_2). PS-FBG_2 is exposed to the same temperature than PS-FBG_1, but it is also subject to axial strain. In this manner, both PS-FBGs shift their wavelength simultaneously with temperature but only the PS-FBG_2 reflects the strain changes. The use of a second grating avoids doubling the whole setup to compensate temperature variations.

These gratings differ from the used in the high resolution temperature system previously presented in section 3.2.1, being narrower and located at 1545.25 nm. For this experiment, a programmable filter with a tunable band-pass of 0.1 nm was chosen to filter the transmission peak of the PS-FBGs. Due to the programmable filter and the couplers inserted in the fiber loop, loss inside the cavity increased considerably (around 12 dB) with respect to Figure 3. 13

scheme. To compensate this deficit without increasing excessively the pump power, 50 km of True Wave single-mode fiber are used for the laser's cavity.

Summarizing, two emission lines are obtained at the output of the scheme: one located at a wavelength affected by temperature and a second one placed at a wavelength affected by both temperature and axial strain. As a result, the electrical signal detected at the output of the set-up appears at a frequency given by the frequency difference between the two emission lines. I.e. the frequency will be driven by the strain applied at the PS-FBG$_2$. It should be noted that temperature does not affect the frequency of the beat signal since both emission lines shift equally (the frequency difference between them remains constant).

b. Experimental results

The generated emission lines are presented in Figure 3. 23. They were measured independently using a pump power of 1.5 W. They are displayed in individual graphs for the sake of clarity since they overlap during the operation of the laser. The peak power of the emission lines is 3.2 and 4.1 dBm, corresponding to PS-FBG$_1$ and PS-FBG$_2$ respectively. Their line-widths are 3.3 and 4.5 pm and the signal-to-noise ratio (SNR) is around -15 dB. The pronounced Stokes and anti-Stokes waves induced by the Brillouin scattering (Chapter II, section 2.1.3) cause a reduction in the SNR.

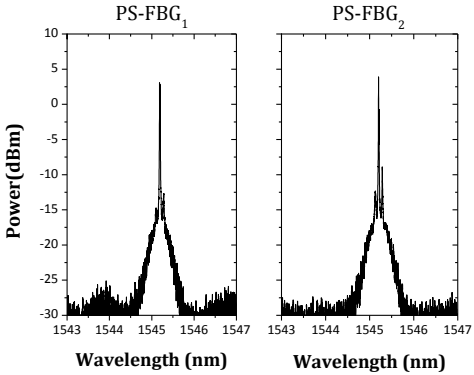

Figure 3. 23. Optical spectrum of the emission lines generated by the PS-FBG$_1$ and (b) PS-FBG$_2$.

Again, a previous test was carried out to confirm that the emission lines correspond to a multi-wavelength RDFB-FL. As in Section 3.2.1, the lasing

threshold and the absence of longitudinal modes were verified. The laser behavior of both emission lines is confirmed by Figure 3. 24, showing a lasing threshold at 1.39 and 1.4 W for PS-FBG$_1$ and PS-FBG$_2$, respectively. Figure 3. 25 depicts the self-beating signal of both emission lines detected at the ESA, proving again the absence of longitudinal modes.

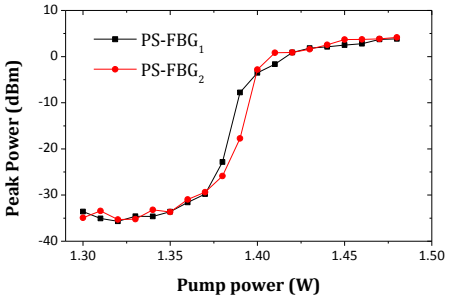

Figure 3. 24. Study of the output power vs pump power injected for the strain sensor system.

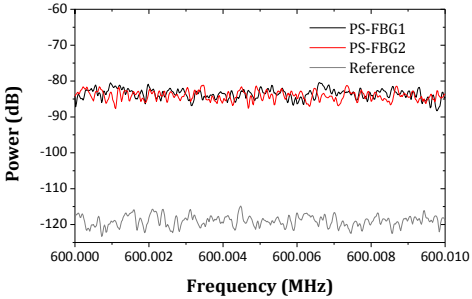

Figure 3. 25. Electrical spectrum of the laser´s self-beating for a resolution of 300 Hz.

Finally, the appropriate operation of the system as high resolution strain sensor system was verified. For this purpose, the sensor PS-FBG$_2$ was fixed to a translation stage controlled by a computer. In order to minimize the temperature difference between gratings, the PS-FBG$_1$ was placed nearby PS-FBG$_2$. Otherwise, a temperature difference between them may cause a frequency shift unrelated to the axial strain. In the test, an axial strain sweep of 2.6 με with steps of 0.2 με was carried out. The frequency shift of the electrical beat between the two emission lines (see Figure 3. 26) was recorded

every step. It can be seen that the SNR is smaller than in Figure 3. 7, mainly due to the high quality of the reference laser used for the beating in the high resolution temperature system and the effect of the ASE noise. Further work in this regard could probably improve the results, for instance, by including filtering elements before the detection. Figure 3. 27 depicts the results of the strain response of the system, showing a linear behavior with a sensitivity of 0.151 GHz/με.

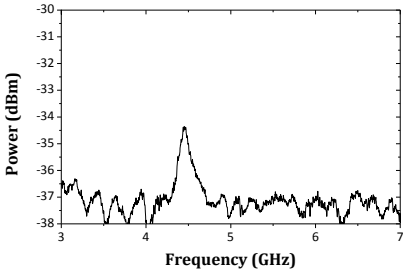

Figure 3. 26. Electrical spectrum of the beat signal for the strain setup.

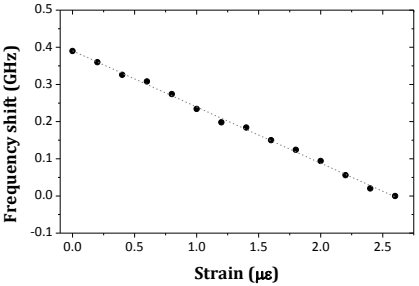

Figure 3. 27. Frequency response to strain variations.

Note that the negative slope of the sensitivity is due to the relative position of the PS-FBG$_2$ with respect to PS-FBG$_1$, but it has no influence in the performance of the system. The translation stage gives an error that varies from 0.1 to 0.12 με in each step. This fact is due to the short distances moved, close to the accuracy limit of the translation stage. To show this effect, the axial strain set in the translation stage (with the error provided) versus the measured strain is showed in Figure 3. 28.

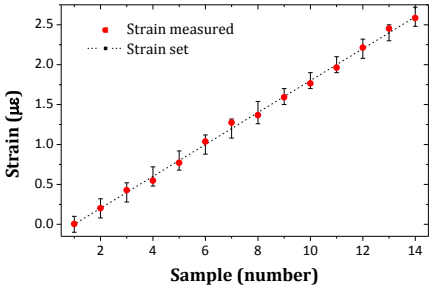

Figure 3. 28. Comparison between measured and set axial strain in the translation stage.

From the graph it can be noticed that the measured strain is under the error given by the translation stage. As a result, the axial strain applied to the sensor can be determined with a resolution under 0.2 με.

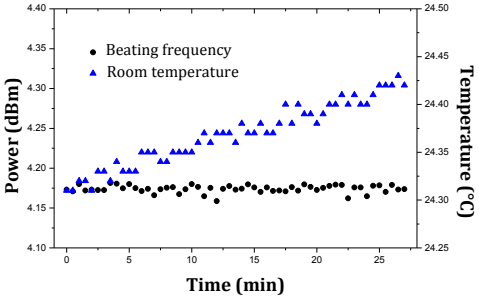

Figure 3. 29. Results of the stability test of the strain setup.

To quantify the stability of the system, a final set of measurements was carried out. The frequency of the beat signal was recorded every 30 s for 28 minutes while the setup was kept at a constant strain. In addition, the room temperature was monitored during the test using an electrical reference probe with a resolution of 0.01 °C. The obtained results are shown in Figure 3. 29. The beat frequency remains stable regardless of the temperature rise of the sensors, demonstrating the adequate behavior of the self-compensating setup. The average measured instability of the beat signal is 22.7 MHz with a 95% of the samples presenting a deviation under 14 MHz. However, this instability is mainly affected by vibrations coupled to the

experimental setup. Then, better results would be expected if the sensors were fixed to a rigid element.

3.4. High resolution transversal load system

In this section, a high resolution transversal load system based on a RDFB-FL is demonstrated, obtaining a sensitivity of 3.95 GHz/Kg and a resolution of 1 g. The modeless behavior of the laser provides high frequency stability and eliminates instabilities related to mode hopping and mode competition, which are present in previous approaches [15][49]-[52]. A full description of the system and experimental results are provided.

a. Description of the system

The presented setup (Figure 3. 30) is a modified version of the scheme presented before in Figure 3. 13 . A polarization controller and a polarizer are included at the output of the laser, just after the variable attenuator. These elements were used to adjust the power of the two generated emission lines and thus enhance the beating between them in the detection stage. The signal was firstly monitored in the optical domain using a BOSA (Brillouin Optical Spectrum Analyzer). Then, it was filtered, detected by a 12 GHz-bandwidth photodetector and finally monitored on an ESA. A variable attenuator was used at the output of the laser to limit the power received and protect the devices.

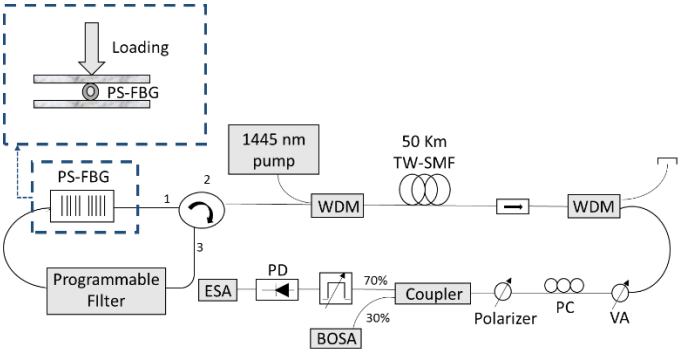

Figure 3. 30. Schematic diagram of the proposed laser for transversal load measurements; inset is the loading configuration.

Sensing principle

Typically, PS-FBGs present two transmission peaks due to the different refractive indexes along the orthogonal directions. When a transverse force is applied to the sensor, those transmission lines will separate due to the change in the PS-FBG birefringence. The frequency spacing between the two transmission peaks along the two orthogonal polarization states is given by [53]:

$$\Delta\upsilon = \upsilon_x - \upsilon_y = \frac{c \cdot B}{n_0 \cdot \lambda_0} \qquad (3.1)$$

Where n_0 is the average index of the fiber, λ_0 is the Bragg wavelength of the fiber grating and B is the load-induced birefringence, given by

$$B = \frac{2 \cdot n_0^{\,3} \cdot (p_{11} - p_{12})(1 + \upsilon_p)\cos(2\theta) \cdot F}{\pi E r} \qquad (3.2)$$

And p_{11} and p_{12} are the components of the strain-optical tensor of the optical material, υ_p is the Poisson's ratio, E is the Young's modulus of the fiber, ϑ is the angle between the direction of the force and the polarization axis of the fiber, r is the radius of the fiber and F is the linear transverse load (force per unit length). Thanks to the load-interrelated transmission lines along the orthogonal polarization directions, two emission lines are generated at different frequencies. The beating between these two signals generates a third signal whose frequency is a function of the load induced birefringence. As a result, the transverse load applied to the PS-FBG can be determined by measuring the beat frequency.

b. Experimental results

In the experiment, a PS-FBG with transmission peaks located around 1545.3 nm was used. A programmable filter with a tunable band-pass of 0.1 nm filtered the transmission peaks of the PS-FBG. As in previous sections, the verification of achieving a RDFB-FL was carried out. Firstly, Figure 3. 31 (a) shows the abrupt increase of the peak power corresponding to the lasing threshold of the system (1.32 W). Additionally, the lack of longitudinal modes was verified by observing the self-heterodyne signal of the laser in the electrical domain (see Figure 3. 31 (b)).

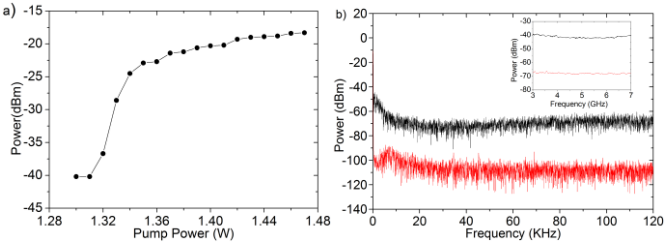

Figure 3. 31.(a) Study of the output power vs pump power injected in the system and (b) electrical spectrum of the laser´s self-beating for different spans (120 KHz and 4 GHz inset) (black line). Noise floor of the detector (red line).

The optical spectrum of the laser can be seen in Figure 3. 32 measured by means of a BOSA. A pump power of 1.46 W was injected and a peak power of -13.7 dBm was obtained, with an optical signal to noise ratio of around 10 dB.

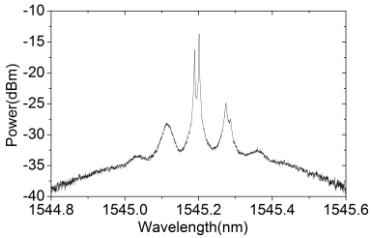

Figure 3. 32. Optical spectrum of the random DFB fiber laser used for transversal load sensing.

After demonstrating the adequate behavior of the system as a RDFB-FL, the transversal load measurements were carried out. When transversal load is applied, the wavelength spacing between the two polarization peaks increases as seen in Figure 3. 33 (a); consequently, the electrical beating moves to higher frequencies (see Figure 3. 33 (b)).

Thus, it is possible to measure transversal load in both optical and electrical domain. However, measuring in the electrical domain with an ESA has two important advantages. The first is its higher resolution. The second is the simplicity of the measurement process, since the frequency of a single peak has to be monitored. For this reason, transversal load was measured following the electrical beating of the emission lines in the ESA. These measurements were taken at room temperature with a load step of 65 grams.

The results, displayed in Figure 3. 34 (a), show a clear linear behavior with a sensor sensitivity of 3.95 GHz/Kg. It can be observed a good linear fitting of the measurements with an error R^2= 0.996.

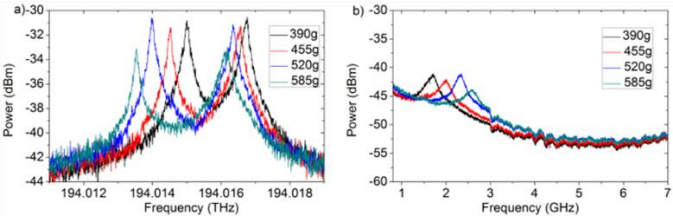

Figure 3. 33. (a) Measured optical spectra of the two emission lines and (b) measured electrical spectra of the beating signal when different transversal loading is applied.

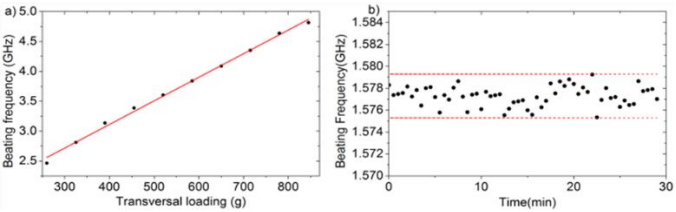

Figure 3. 34. (a) Variation of the beating frequency between the two emission lines versus transversal loading and (b) Stability measurements of the beating frequency at constant loading during 30 min.

The main reason of the mismatch with the linear fitting is mainly caused by the experimental setup itself. The employed method did not allow to keep constant the angle of the load applied on the PS-FBG during the measurement process. As a result, possible variations of this angle could have caused a small mismatch in the measurements. Accordingly, to quantify the maximum possible resolution of the system, the instability of the laser was measured at room temperature and at a constant load. The beating of the two emission lines was measured every 30 s for a total period of 30 min. The laser instability results are shown in Figure 3. 34 b), from which a resolution of 4 MHz can be derived. Thus, a maximum resolution of 1 g can be obtained using this system.

3.5. Distributed systems

The ability to detect internal failures and provide early warnings of structural damages or decays becomes crucial in engineering constructions. The main parameters to consider when interrogating the health condition of structures are load, deformation, strain, temperature and vibration. Optical fiber sensors present specific advantages to be exploited in structural health monitoring (SHM) systems. Among them, FBGs offer a huge capacity for mechanical sensing applications [54]. In addition, they allow multiplexing and then multipoint sensing schemes, placing many gratings within a single optical fiber. However, the number of sensing points is limited by the spectral ranges of the emitting and detecting devices. One way to solve this restriction is by using distributed optical fiber sensing systems.

Several previous works confirm that fiber optic distributed systems are especially suited for structural health monitoring (SHM) applications [55]-[58]. They show a large-scale monitoring range, large number of monitored points, simple deployment, and geometric versatility if compared with point sensors [59]. Among the existing distributed systems, phase-sensitive optical time domain reflectometry (phase-OTDR, or ϕ-OTDR) has proven to be a powerful tool for real-time distributed sensing. Various events can be monitored, such as borderline intrusion, seismic waves and train movement [60]-[62]. In phase-OTDR systems, a light source with a narrow linewidth and minimum frequency shift is employed. Light is pulsed and later injected into a conventional single-mode fiber. The multiple scattering centers within the resolution cell generate backscattered light components that interfere coherently at the phase-OTDR detector. By measuring the variation of the coherent superposition of the backscattered light, any perturbation can be identified and localized along the sensing fiber.

However, the SNR of a phase-OTDR is limited by the weak Rayleigh backscattering generated in the fiber. The utilization of an FBG array can improve the SNR in certain zones of the sensing fiber and also provides a high-precision dynamic strain measurement capability [63]-[65]. FBGs can act as individual scattering centers with well-defined positions and reflectivities. Therefore, the phase-OTDR is required to register the FBG reflections rather than the Rayleigh backscattered light from the fiber. By interrogating an array of FBGs, it is possible to detect any phase variation appearing between two of them, as long as they are separated by a distance smaller than the resolution cell and the resolution cell only covers two FBGs at a time [66][67].

In this manner, we prevent signals from more than two FBGs to interfere simultaneously [66].

This section is divided in two main parts. In the first one, the performance of a phase-OTDR sensing system based on the concatenation of identical low-reflective fiber Bragg gratings is investigated. Then, a post-processing procedure to reduce spectral shadowing crosstalk, which represents an undesirable effect in these systems, is presented and validated.

3.5.1. Performance evaluation of Phase-OTDR sensing system

We present a performance analysis of a phase-OTDR sensing system based on the succession of identical low-reflective FBGs. In addition, the performance limit of the system is estimated by means of simulations, identifying the influence of the design parameters such as FBG reflectivity, dynamic range, spatial resolution and SNR.

a. Description of the system

The proposed sensor scheme is shown in Figure 3. 35. An equally spaced sequence of N+1 identical FBGs are illuminated by optical pulses (of width *W*) injected by the phase-OTDR source.

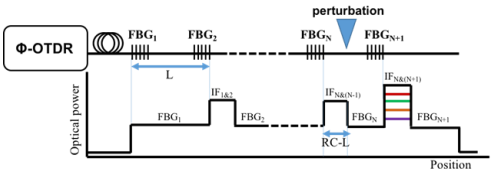

Figure 3. 35. Proposed sensor scheme of (N+1) cascaded FBG sensors, including power levels of the corresponding phase-OTDR signature.

When the resolution cell (*RC=W/2*) is greater than the distance *L* between two successive FBGs in the array, the reflected signals interfere over trace sections of a particular length equal to *RC-L*. Due to the narrow linewidth of the laser, the coherence is maintained when the reflected signals overlap at the detector and interference occurs. These interference sections, represented as *IF* in Figure 3. 35, together with the zones between them (where the signal is reflected from only one FBG) form the phase-OTDR signature.

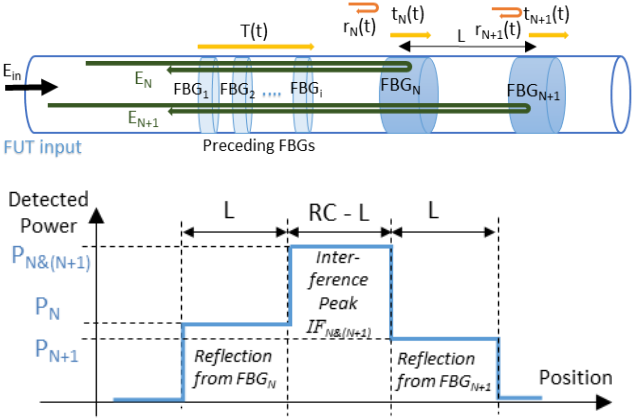

Figure 3. 36. Scheme of the theoretical analysis of reflected signals from a single FBG pair, including power levels of the corresponding phase-OTDR signature.

Let us analyze one of these interference sections, $IF_{N\&(N+1)}$, created by the superposition of the electric fields E_N and E_{N+1} (i.e. optical signals reflected from FBG_N and FBG_{N+1}, see Figure 3. 36). The optical power of the reflected signal from FBG_N (FBG_{N+1}) detected by the phase-OTDR is denoted by P_N (P_{N+1}) and the optical power of the interference signal by $P_{N\&(N+1)}$. The complex reflection coefficient, r_N, and the complex transmission coefficient t_N for FBG_N are determined as a function of known parameters, namely grating length, grating pitch, and average refractive index modulation 1.2. Given a complex electric field E_{in} at the Fiber under test (FUT) input, the electric fields E_N and E_{N+1} can be represented as

$$E_N = E_{in}T^2(t)r_N(t) \qquad (3.\ 3)$$

$$E_{N+1} = E_{in}T^2(t)t_N^2(t)r_{N+1}(t)e^{-i\Delta\phi(t)} \qquad (3.\ 4)$$

where $T(t)$ is the complex transmission coefficient of the FUT between its input and FBG_N and $\Delta\phi(t)$ is twice the phase difference between FBG_N and FBG_{N+1}. Using *(3. 3)* and *(3. 4)*, the interference signal $E_{N\&(N+1)}$ at the detector resulting from E_N and E_{N+1} is given by:

$$E_{N\&(N+1)} = E_N + E_{N+1} = E_{in}T^2(t)r_N(t) + E_{in}T^2(t){t_N}^2(t)r_{N+1}(t)e^{-i\Delta\phi(t)} \qquad (3.\ 5)$$

The power reflected from the FBG pair and detected by the phase-OTDR shows three different zones (see Figure 3. 36) with corresponding powers P_N, P_{N+1} and $P_{N\&(N+1)}$:

$$P_N = E_N E_N{}^* = |E_{in}|^2 |T(t)|^4 |r_N(t)|^2 \quad (3.\ 6)$$

$$P_{N+1} = E_{N+1} E_{N+1}{}^* = |E_{in}|^2 |T(t)|^4 |t_N(t)|^4 |r_{N+1}(t)|^2 \quad (3.\ 7)$$

The detected power corresponding to the interference region can be calculated as

$$\begin{aligned} P_{N\&(N+1)} &= (E_N + E_{N+1})(E_N + E_{N+1})^* = \\ &= |E_{in}|^2 |T(t)|^4 |r_N(t)|^2 + |E_{in}|^2 |T(t)|^4 |t_N(t)|^4 |r_{N+1}(t)|^2 + \\ 2|E_{in}|^2 |T(t)|^4 |t_N(t)|^2 \, &|r_N(t)||r_{N+1}(t)| \cos(\Delta\phi(t) + \theta(t)) \end{aligned} \quad (3.\ 8)$$

where $\theta(t) = \arg(r_{N+1}(t)/r_N(t))$. When a perturbation is applied somewhere along the FUT, it may result in fiber strain and/or a local change in refractive index. In our simulations, the expression developed in equation *(3. 8)* is implemented based on the setup of Figure 3. 37 a). The first perturbation (SHR1) is applied on FBG_4, while the second one (SHR2) influences the fiber section between FBG_5 and FBG_6. The vibration induced by the shakers is simulated by introducing local variations in the effective refractive index. On the one hand, if the perturbation is directly applied on the grating, e.g. FBG_4 in Figure 3. 37 a), the *r* and *t* coefficients of this FBG vary. This will also cause a phase change in the neighboring gratings, as observed for the zones $IF_{3\&4}$, FBG_4, and $IF_{4\&5}$ (see Figure 3. 37 b). On the other hand, if a perturbation is applied on the fiber section between two FBGs, the result will be a modulation of the phase difference $\Delta\phi\ (t)$ between them. This effect is tested between FBG_5 and FBG_6 (see Figure 3. 37 a)) and can be noticed in the $IF_{5\&6}$ zone in Figure 3. 37 (b).

Performing a Fourier analysis of the phase-OTDR signature at the perturbation-influenced positions over many successive measurements allows determining the frequency content of the perturbation. This procedure is known as slow-time analysis.

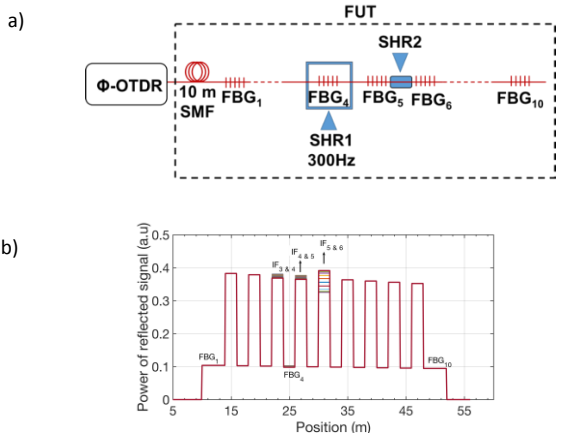

Figure 3. 37. (a) Simulated sensor scheme, (b) successive simulated phase-OTDR traces for N=10, two perturbations are applied: directly on FBG_4, and on the fiber section between FBG_5 and FBG_6. SHR: Shaker.

b. Experimental results

Experimental work was carried out to validate the vibration frequency extraction scheme. A direct detection phase-OTDR was used to interrogate ten cascaded FBGs that were placed after a lead fiber of 1.5 km. The center wavelength of each identical FBG is 1552.5 nm with a bandwidth of 0.2 nm. The gratings were manufactured using Noria FBG manufacturing facilities (phase mask technique). A Draka BendBright G.657 single mode fiber was employed, showing an effective refractive index of 1.4471. Re-coating was not implemented after inscription. The FBGs presented a length of 4 mm, a grating periodicity of 535 nm and an average refractive index modulation of ~10^{-5}. The reflectivity of the FBGs was 0.02%.

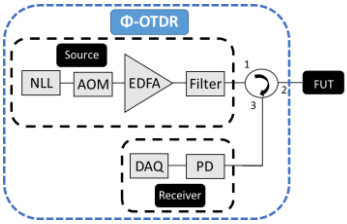

Figure 3. 38. Phase-OTDR Source and receiver structure.

The phase-OTDR interrogator structure is represented in Figure 3. 38. A highly coherent ultra-narrow linewidth laser (NLL) is used as the light source, giving a signal with 0.1 kHz linewidth centered at 1552.51 nm and 40 mW continuous output power. Later, the input signal is modulated by an acousto-optic modulator (AOM), which applies a frequency shift of 160 MHz to emit probe pulses with a repetition frequency of 20 kHz. These pulses are amplified by an Erbium doped fiber amplifier (EDFA), followed by a 0.9 nm band-pass filter. These four elements form the source unit. Finally, the receiver unit is composed by a photo-detector (PD) and a data acquisition card (DAQ). The reflected signature of the FBG array is detected by the PD, with a 5 MHz electrical bandwidth, and then is sampled at 1 GHz using the DAQ. 1850 consecutive traces were recorded for each measurement, resulting in a slow-time window of about 90 ms. The total measurement time is given as the number of pulses times the pulse separation.

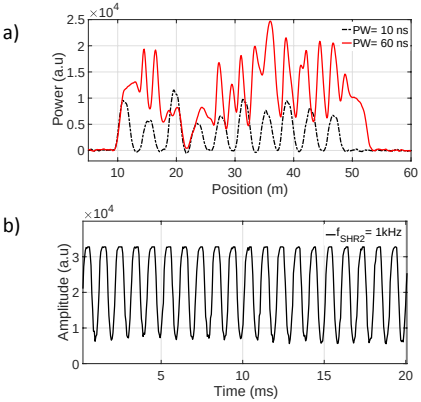

Figure 3. 39. (a) Comparison of experimental traces for the pulse-widths of 10 ns (RC=1 m) and 60 ns (RC=6 m), (b) variation of phase-OTDR trace over slow-time window (zoomed at 0-20 ms portion) at 32 m ($IF_{5\&6}$).

To perform the vibration experiments, the fiber section between FBG_5 and FBG_6 was glued onto a 2 m long, 16 mm diameter plastic tube that was clamped at both ends. The distance between the FBGs was 4 m, and consequently the resolution cell was chosen between 4 m and 8 m. The measurements were therefore carried out with a pulse width of *PW*= 60 ns, corresponding to a 6-m resolution cell. Perturbations were applied at two different positions as indicated in Figure 3. 37 a). A shaker SHR1 applied 300 Hz, 1 g acceleration vibrations on FBG_4. In addition, the midpoint of the plastic

tube between FBG_5 and FBG_6 was excited by shaker SHR2, giving an acceleration of 0.1 g at frequencies 1 - 6 kHz. A reference trace was taken with *PW*=10 ns to determine the FBG positions in the FUT. For the sake of simplicity, only the last 60 m section of the FUT including the 10 FBGs is shown in Figure 3. 39 (a).

In order to obtain the frequency components of the applied vibrations, a Fourier analysis was performed on certain zones of the OTDR signature. The frequency of shaker SHR2 can be identified in the $IF_{5\&6}$ zone (at the position 32 m in the analyzed section shown in Figure 3. 40 a), while the frequency of shaker SHR1 was observed in three different sections ($IF_{3\&4}$, FBG_4, $IF_{4\&5}$). The FFT analysis performed in the FBG_4 zone is shown in Figure 3. 40 b). The provided graphs verify the ability of the proposed scheme to monitor the presence and the frequency content of the perturbations along the FUT.

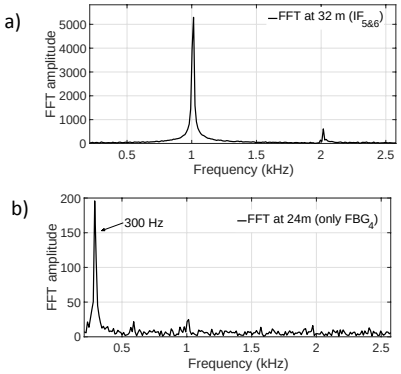

Figure 3. 40. (a) FFT at 32 m for $IF_{5\&6}$, (b) FFT at 25 m for the FBG_4 - only reflection zone.

So as to offer a more complete study of the system, the theoretical number of FBGs that can be interrogated was estimated. Given the present phase-OTDR system, at least 4000 FBGs could be interrogated, maximizing the dynamic range of the system and having more than 5 dB margin to the RMS noise level (see Figure 3. 41). This estimation was carried out considering a maximum detectable reflected power of 100 µW, a fiber loss of 0.2 dB/km, an FBG reflectivity of 0.02% and an experimental RMS noise level of 0.50 µW.

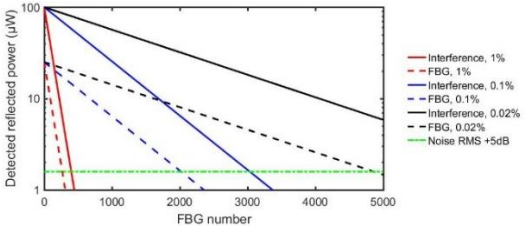

Figure 3. 41. Maximum number of FBGs possible to interrogate with the setup using 0.02%, 0.1% and 1% reflectivity FBGs, respectively.

This maximum number of FBGs is based on identical FBGs inscribed along the fiber, assuming no splices or connectors along the way giving additional loss. In addition, the pulse quality is assumed to be good enough for the 5 dB noise margin to enable power detection from the last FBG. It is also based on the fact that not only all the interference powers but also the reflected powers from all individual FBGs should be measured. Under the same conditions, a setup with identical 1% (0.1%) reflectivity FBGs results in a maximum of 250 (2000) FBGs in the array.

3.5.2. Spectral shadowing suppression in Phase-OTDR sensing systems

Spectral shadowing 1.2 is a limiting factor in phase-OTDR systems using arrays of FBGs. The interrogating light needs to pass all upstream FBGs to reach a specific FBG. As a result, the light illuminating a certain FBG in the array carries the spectral features of all the previous ones, shadowing the response of the actual FBG. The resulting error was studied in [69] in the context of a quasi-distributed fiber sensor interrogated by an OFDR (Optical Frequency Domain Reflectometer). The parasitic effects present in the scheme were simulated and enhancement treatments proposed.

In this section, the spectral shadowing effect in a phase-OTDR system based on an array of FBG pairs is analyzed. A detailed study of the signals involved in the scheme allowed the development of a post-processing method which reduces the spectral shadowing effect. The performance of the compensation technique is demonstrated by simulations and then experimentally for vibration measurements.

a. Description of the system

For this study, an adaptation of the system proposed in the previous section is used. For this reason, the theoretical study of the signals involved, see Figure 3. 36, and the already presented mathematical analysis set the starting point to develop the post-processing technique.

First, it is important to remark that *T(t), which* is the complex transmission coefficient of the FUT between its input and FBG_N, depends on the spectral properties of the preceding FBGs. For this reason, it has an influence on the power detected for the interference signal $P_{N\&(N+1)}$. Using equations *(3. 6) and (3. 7)*, the expression *(3. 8)* can be re-written as:

$$P_{N\&(N+1)} = P_N(t) + P_{N+1}(t) + \\ +2|E_{in}|^2|T(t)|^4|t_N(t)|^2\,|r_N(t)||r_{N+1}(t)|\cos(\Delta\phi(t)+\theta(t)) \qquad (3.\ 9)$$

And then developing *(3. 9)*, the following formula can be calculated:

$$cos(\,\Delta\phi(t)+\theta(t)) = \frac{P_{N\&(N+1)}(t)-P_N(t)-P_{N+1}(t)}{2\left[(P_N(t))^{1/2}(P_{N+1}(t))^{1/2}\right]} \qquad (3.\ 10)$$

By reading out the three power values from the phase-OTDR trace, e.g. P_N, P_{N+1} and $P_{N\&(N+1)}$, the change in the phase component $\Delta\phi(t)+\theta(t)$ occurring upon any events between FBG_N and FBG_{N+1} can be monitored. As a direct consequence, the undesired spectral shadowing from preceding FBGs can be eliminated.

In Figure 3. 42, the experimental setup proposed to validate the post-processing method is presented. It shows the same structure as the previous scheme in Figure 3. 38. In this case, a NLL with a linewidth of 0.1 kHz and a central wavelength of 1553.1 nm was employed. As before, the probe pulses generated after the AOM are amplified and filtered before entering the FUT. The backscattered/reflected light in the FUT is directed to the receiver through port 3 of a 3-port optical circulator for detection. The receiver remains the same as in the previous set-up. Finally, the variation in detected power over time is registered and analyzed.

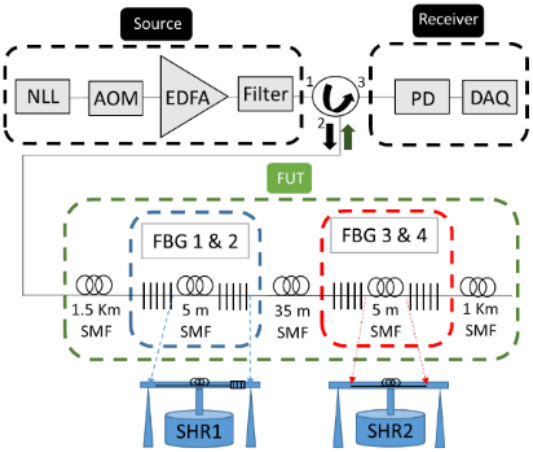

Figure 3. 42. Experimental set-up.

Spectral shadowing crosstalk becomes relevant when a light source illuminates a concatenation of FBGs with overlapping spectral features. Consequently, distortion builds up along the fiber. To study its effects, two pairs of low reflectivity (~1%) FBGs have been employed. The four FBGs inscribed in the FUT essentially share the same characteristics, having a center wavelength of ~1553.4 nm, a 3 dB bandwidth of ~1 nm and a length of 4 mm. The grating pitch is 536.73 nm and the average refractive index modulation is $1.6x10^{-5}$ with an effective refractive index of 1.4471. A lead-in fiber spool of 1.5 km is followed by the set of FBGs and a terminating fiber spool of 1 km length. The two pairs are separated by approximately 35 m and the two FBGs in each pair are separated by 5 m. In the present study, the large distance applied between the FBG pairs is for visibility reasons. However, the formalism and suppression technique developed can directly be applied to equidistant FBG arrays. The 5 m fiber length between the first two FBGs (FBG_1 and FBG_2) and FBG_2 itself are attached to a plastic tube connected at its midpoint to a shaker (SHR1), leaving FBG_1 static. Additionally, the 5 m section between FBG_3 and FBG_4 is attached to another plastic tube connected at its midpoint to shaker SHR2, while FBG_3 and FBG_4 are static. Both plastic tubes have their ends clamped. In the experiment, SHR1 and SHR2 are driven by a sinusoidal signal at 300 Hz and 2 kHz, respectively, with a 1 g (0.04 g) acceleration amplitude.

b. Experimental results

Simulations were performed based on the setup in Figure 3. 42 to validate the spectral shadowing compensation technique. They were performed in Matlab by computing 1000 phase-OTDR traces with a time separation of 50 μs and a sampling resolution of 0.1 m. Each trace was computed as a function of the pulse position using equations *(3. 6)-(3. 8),* considering a rectangular pulse shape and neglecting the Rayleigh backscattering signal as well as the fiber attenuation. The vibration induced by the shakers was simulated by introducing variations in the effective refractive index, $\Delta n(t)= \Delta n_m \sin(2\pi f t)$, in each part of the FUT being subject to vibration. As in the experimental setup, the frequency of vibration f was set to 300 Hz (2 kHz) for SHR1 (SHR2), assuming a maximum refractive index change Δn_m of 10^{-6} (10^{-8}) induced by the vibration.

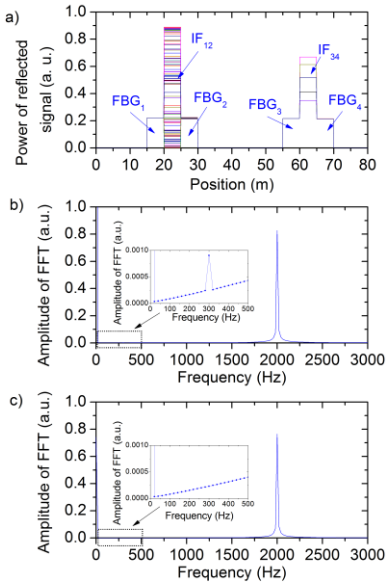

Figure 3. 43. Simulated (a) reflected signal power versus position over time (b) FFT for zone IF_{34} at 62.5 m (inset: zoom around 300 Hz) (c) FFT for zone IF_{34} at 62.5 m after applying the compensation formula (inset: zoom around 300 Hz) with a 300 Hz (2 kHz) vibration applied at the first (second) FBG pair.

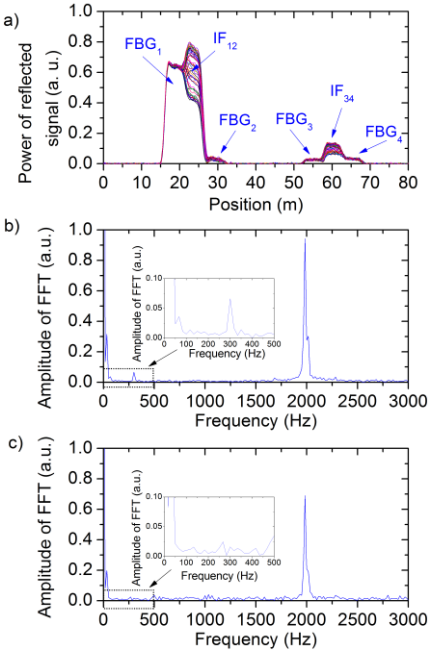

Figure 3. 44. Detected (a) reflected signal power versus position over time (b) FFT for zone S34 at 60 m (inset: zoom around 300 Hz) (c) FFT for zone S34 at 60 m after applying the compensation formula (inset: zoom around 300Hz) with a 300 Hz (2 kHz) vibration applied at the first (second) FBG pair.

Figure 3. 43 a) shows the superposed phase-OTDR traces obtained from a simulation with the given parameters. The characteristic reflection zone can be identified for the two FBG pairs, with the interference zones IF_{12} = 20-25 m and IF_{34} = 60-65 m showing the largest change in detected power over time. As before, FFT analysis was applied at a position within the IF_{34} zone to determine the frequency of the applied vibration. Likewise, the frequency of vibration at other points of the FUT can be determined. In zone IF_{34} spectral shadowing may appear due to the perturbation applied on FBG_2 by shaker SHR1, resulting in a time-varying transmission coefficient t_2 of FBG_2. Figure 3. 43 b) shows the FFT result at 62.5 m, i.e. at the midpoint of the interference zone IF_{34}. Two frequencies are distinguished: 2 kHz and 300 Hz, the last one with a lower amplitude. The optical signal transmitted through the first FBG pair reaches the second FBG pair, modulating the input signal of FBG_3. As the FBGs have overlapping spectral properties, the interference signal generated

by the second pair contains the spectral information of the previous FBG. For this reason, the 300 Hz component is noticed in the FFT although no vibration of that frequency is present at that position.

In order to avoid this undesirable effect, equation *(3. 10)* is applied to eliminate the influence of spectral shadowing, using the simulated detected power $P_{N\&(N+1)}$, P_N and P_{N+1} over time at the midpoints of the three zones (IF_{34}, FBG_3 and FBG_4) around 62.5 m. The signal obtained after applying the compensation formula, Figure 3. 43 c), is dimensionless and power variations are cancelled out. Spectral information about the local perturbation is not removed since it is contained in the phase term $\Delta\phi(t) + \theta(t)$. As shown in Figure 3. 43 c), the 300 Hz component is suppressed.

The above analysis procedure was also applied on experimental phase-OTDR traces recorded under similar conditions. The experimental traces and the FFTs obtained for the IF_{12} and IF_{34} zones are presented in Figure 3. 44 a) and Figure 3. 44 b), respectively. As in the simulation analysis, the compensation formula *(3. 12)* was applied to the detected power over time $P_{N\&(N+1)}$, P_N and P_{N+1} at the midpoints of the three zones IF_{34}, FBG_3 and FBG_4, demonstrating its capability to suppress the 300 Hz FFT component as shown in Figure 3. 44 c). The experimental results agree with the simulations and show the feasibility of employing this technique for the suppression of the spectral shadowing effect.

3.6. Conclusions

The main purpose of Chapter III was to present a novel set of applications of RDFB-FL for high resolution measurements. In Figure 3. 2, an initial scheme is proposed to measure temperature with a resolution as high as 0.01 °C. Then, three variations of this primary scheme were developed to perform high resolution cryogenic temperature (Figure 3. 13), strain (Figure 3. 22) and transversal load (Figure 3. 30) measurements.

In summary, this chapter aims to offer a possible answer to two main problems of high resolution systems, taking advantage of the intrinsic properties of RDFB-FL.

- First, sensing schemes based on fiber lasers commonly present an inherent limited resolution. This fact is mainly caused by instabilities given by effects like mode hopping and mode competition.
- Secondly, the resolution provided by optical devices is reduced if compared to the one offered by electrical devices. Heterodyne detection is a simple implementation solution, but it requires a narrow and stable laser line width.

In this regard, the main part of fiber lasers do not satisfy these requirements but RDFB-FL can contribute to solve these issues. Their mode-less behavior and high stability, in both frequency and amplitude, allows the creation of high resolution sensor systems compatible with heterodyne detection.

In the proposed scheme and its variations, the spectrum of the laser was narrowed by several filtering elements, depending on each application. PS-FBGs were chosen to filter and reduce the line width to a few picometers. Since the filtering elements are gratings, the wavelength of the emission line is sensitive to all the parameters to which a grating reacts. Consequently, temperature, strain and transversal load can be measured just by tracking the displacement of the emission line of the laser. In this manner the intrinsic properties of RDFB-FL were exploited in pursuit of the objective: to perform high resolution measurements.

After explaining the main motivation of the chapter and the solutions provided to carry out our objective, we can draw some conclusions from the accomplished experiments as following:

- The proposed system in section 3. 2. 1 demonstrated its capability to perform high resolution temperature measurements. Variations under 0.01 °C were successfully detected although the maximum resolution of the system was limited by the resolution of the temperature probe used

as reference. In future work, the accuracy of the system could be improved by further narrowing the line-width of the emission line or combining this system with improved-sensitivity FBGs (coated or bonded FBGs).

- In section 3. 3, a high resolution axial strain sensor system with a measured resolution of 0.2 με is presented. One of the main advantages of this setup is that there is no need of using an external laser source to beat the output of the laser. In addition, its structure self-compensates temperature variations, avoiding crosstalk with the axial strain measurements.
- Transversal load measurements were also performed, completing the range of parameters measured with this RDFB-FL system. A resolution of 1 g was obtained, although it could be further improved by simply modifying the technique which apply load to the sensor. This set-up has a margin of improvement; however, it offers twice or more sensitivity compared with other previously published works, being a system with great potential.

The subsection 3. 2. 2 is dedicated to examine the performance of four different fiber optic sensors at cryogenic temperatures. As a general conclusion, performing measurements at cryogenic temperatures is complex for the following reasons:

- Firstly, the reduced spaces needed to perform the measurements might cause large power losses and sometimes damage the sensors due to the difficult handling.
- Although the presented approach is very simple, it cannot reach pure cryogenic temperatures. Several attempts were carried out to reach lower temperatures using a cryostat and liquid Helium, which presents a boiling temperature of -269 °C. However, the technical difficulties associated with the equipment used, such as the reduced space and the large temperature gradients in the cryostat, did not allow to obtain reliable measurements.
- The isolation plays a significant role since temperature does not remain constant for long periods of time and a fast response of the sensors is required in dynamic measurements. Accordingly, sensors with high response time are not suitable for dynamic measurements at cryogenic temperatures using the proposed cooling technique.
- In addition, temperature gradients in the measuring locations, affect the temperature detected by the sensors, and so the accuracy of the results, which limit the resolution of the measurements.

From the experiments carried out in this work, the most outstanding aspects of each sensor are grouped in Table 3. 4. Two main categories are distinguished: advantages and drawbacks in relation to their application in cryogenic temperature measurements.

Studied sensor	Advantages	Drawbacks
PCF-FP	✓Reduced size ⬇ ✓Usable in reduced spaces ✓Low response time	× Lower sensitivity × Reduced endurance
Sagnac	✓Larger size ⬇ ✓Higher sensitivity	× Non-usable in reduced spaces × High response time × Greatly influenced by placement
PS-FBG in RDFB-FL	✓Reduced size ⬇ ✓Usable in reduced spaces ✓Low response time	× More complex measuring technique - requires further automation × Extreme bends must be avoided to guarantee laser operation

Table 3. 4. Comparison of the sensors.

Finally, several conclusions can be drawn from the work done on distributed systems.

- The results presented in section 3. 6 verify that quasi-distributed systems are a powerful tool to monitor all types of structures. The proposed system was capable of detecting where fiber vibration occurs, as well as extracting the vibrational frequency at that particular point and along the entire sensing fiber. The use of weak-FBGs inscribed along the fiber allowed to improve the SNR and the general precision of the vibration detection system. A maximum number of 4000 gratings with identical 0.02% reflectivity has been estimated to be interrogated with the available devices.
- In addition, an extensive theoretical analysis of the signals involved in the system has allowed to develop a post-processing method that reduces the spectral shadowing crosstalk and improved the overall performance of the structure. It is important to remark that only two pair of gratings were monitored to verify in a simple manner the validity of the proposed technique. However, the formalism and suppression technique developed can directly be applied to equidistant FBG arrays. In the case of interrogating an array of dozens of gratings, the spectral shadowing crosstalk accumulated at the end of the fiber may degrade the quality of the detected signal and can lead to poor fault detection. For this reason, the proposed method would be an interesting technique to implement in this type of applications.

These results have originated the publications in references [16][17][70][71][72].

3.7. References

[1] Udd, E., & Spillman Jr, W. B. (Eds.). (2011). *Fiber optic sensors: an introduction for engineers and scientists*. John Wiley & Sons.

[2] Lee, B. (2003). Review of the present status of optical fiber sensors. Optical fiber technology, 9(2), 57-79.

[3] Alwis, L., Sun, T., & Grattan, K. T. V. (2016). *Developments in optical fibre sensors for industrial applications*. Optics & Laser Technology, 78, 62-66.

[4] Krohn, D. A., MacDougall, T., & Mendez, A. (2014). *Fiber optic sensors: fundamentals and applications*. Bellingham, WA: Spie Press.

[5] Urban, G., Jachimowicz, A., Kohl, F., Kuttner, H., Olcaytug, F., Kamper, H., & Schönauer, M. (1990). *High-resolution thin-film temperature sensor arrays for medical applications*. Sensors and Actuators A: Physical, 22(1-3), 650-654.

[6] Zhang, L., Fallon, R., Everall, L. A., Williams, J. A. R., & Bennion, I. (1998, September). *Large-dynamic-range and high-resolution from a strain sensing system using long-period grating interrogating FBG strain sensor. In Optical Communication*, 1998. 24th European Conference on (Vol. 1, pp. 609-610). IEEE.

[7] Koyamada, Y., Eda, Y., Hirose, S., Nakamura, S., & Hogari, K. (2006). *Novel fiber-optic distributed strain and temperature sensor with very high resolution. IEICE transactions on communications*, 89(5), 1722-1725.

[8] Shao, L. Y., Dong, X., Zhang, A. P., Tam, H. Y., & He, S. (2007). *High-resolution strain and temperature sensor based on distributed Bragg reflector fiber laser*. IEEE photonics technology letters, 19(20), 1598-1600.

[9] Gatti, D., Galzerano, G., Janner, D., Longhi, S., & Laporta, P. (2008). *Fiber strain sensor based on a π-phase-shifted Bragg grating and the Pound-Drever-Hall technique*. Optics express, 16(3), 1945-1950.

[10] Chen, D., Liu, W., Jiang, M., & He, S. (2009). *High-resolution strain/temperature sensing system based on a high-finesse fiber cavity and time-domain wavelength demodulation*. Journal of lightwave technology, 27(13), 2477-2481.

[11] Koyamada, Y., Imahama, M., Kubota, K., & Hogari, K. (2009). *Fiber-optic distributed strain and temperature sensing with very high measurand resolution over long range using coherent OTDR*. Journal of Lightwave Technology, 27(9), 1142-1146.

[12] Liu, Q., He, Z., Tokunaga, T., & Hotate, K. (2010, September). *An ultra-high-resolution FBG static-strain sensor for geophysics applications*. In Fourth European Workshop on Optical Fibre Sensors (Vol. 7653, p. 76530W). International Society for Optics and Photonics.

[13] Huang, Y., Wei, T., Zhou, Z., Zhang, Y., Chen, G., & Xiao, H. (2010). *An extrinsic Fabry–Perot interferometer-based large strain sensor with high resolution. Measurement science and technology*, 21(10), 105308.

[14] Liu, Q., Tokunaga, T., & He, Z. (2011). *Ultra-high-resolution large-dynamic-range optical fiber static strain sensor using Pound–Drever–Hall technique*. Optics letters, 36(20), 4044-4046.

[15] Yu, K., Wu, C., Sun, M., Lu, C., Tam, H. Y., Zhao, Y., & Shao, L. (2015). *Fiber laser sensor for simultaneously axial strain and transverse load detection. Measurement*, 62, 137-141.

[16] Leandro, D., deMiguel-Soto, V., & Lopez-Amo, M. (2016). *High-Resolution Sensor System Using a Random Distributed Feedback Fiber Laser*. Journal of Lightwave Technology, 34, 4596-4602.

[17] DeMiguel-Soto, V., Leandro, D., & Lopez-Amo, M. (2016, May). *High-resolution transversal load sensor using a random distributed feedback fiber laser*. In Sixth European Workshop on Optical Fibre Sensors (Vol. 9916, p. 991606). International Society for Optics and Photonics.

[18] Tan, S., Wang, S., Saraf, S., & Lipa, J. A. (2017). Pico-kelvin thermometry and temperature stabilization using a resonant optical cavity. Optics Express, 25(4), 3578-3593.

[19] Zhang, H., Shi, W., Duan, L., Fu, S., Sheng, Q., & Yao, J. (2017, February). High-resolution temperature sensor through measuring the frequency shift of single-frequency Erbium-doped fiber ring laser. In Laser Resonators, Microresonators, and Beam Control XIX (Vol. 10090, p. 1009016). International Society for Optics and Photonics.

[20] Duan, L., Zhang, H., Shi, W., Yang, X., Lu, Y., & Yao, J. (2018). High-resolution temperature sensor based on single-frequency ring fiber laser via optical heterodyne spectroscopy technology. Sensors, 18(10), 3245.

[21] Wada, A., Tanaka, S., & Takahashi, N. (2018). Fast and High-Resolution Simultaneous Measurement of Temperature and Strain Using a Fabry–Perot Interferometer in Polarization-Maintaining Fiber With Laser Diodes. Journal of Lightwave Technology, 36(4), 1011-1017.

[22] Yeager, C.J.; Courts, S.S. *A review of cryogenic thermometry and common temperature sensors*, IEEE Sens. J. 2001, 1, 352–360.

[23] Rajinikumar, R., Nyilas, A., Süsser, M., & Narayankhedkar, K. G. (2006). *Investigation of fiber Bragg grating sensors with different coating materials for high sensitivity*. Proc ICEC, 21, 467-70.

[24] Mishra, V., Lohar, M., & Amphawan, A. (2016). *Improvement in temperature sensitivity of FBG by coating of different materials*. Optik-International Journal for Light and Electron Optics, 127(2), 825-828.

[25] Lupi, C., Felli, F., Brotzu, A., Caponero, M. A., & Paolozzi, A. (2008). *Improving FBG sensor sensitivity at cryogenic temperature by metal coating. IEEE Sensors Journal*, 8(7), 1299-1304.

[26] Rajinikumar, R., Süßer, M., Narayankhedkar, K. G., Krieg, G., & Atrey, M. D. (2009). *Design parameter evaluation of a metal recoated Fiber Bragg Grating sensors for measurement of cryogenic temperature or stress in superconducting devices*. Cryogenics, 49(5), 202-209.

[27] Mizunami, T., Tatehata, H., & Kawashima, H. (2001). *High-sensitivity cryogenic fibre-Bragg-grating temperature sensors using Teflon substrates.* Measurement Science and Technology, 12(7), 914.

[28] Wu, M. C., & DeHaven, S. L. (2006, April). *High-sensitivity cryogenic temperature sensors using pressurized fiber Bragg gratings*. In Optical Sensing II (Vol. 6189, p. 61890O). International Society for Optics and Photonics.

[29] Rajini-Kumar, R., Suesser, M., Narayankhedkar, K. G., Krieg, G., & Atrey, M. D. (2008). *Performance evaluation of metal-coated fiber Bragg grating sensors for sensing cryogenic temperature*. Cryogenics, 48(3-4), 142-147.
[30] Monteiro, J., Martins, R., Caldas, P., & Rego, G. (2011). *Fiber optic sensor based on long period fiber grating to monitor cryogenic temperatures*. Proc. IX SEONS.
[31] Sengupta, D., Shankar, M. S., Reddy, P. S., Prasad, R. S., Narayana, K. S., & Kishore, P. (2011, November). *An improved low temperature sensing using PMMA coated FBG*. In Asia Communications and Photonics Conference and Exhibition (p. 831103). Optical Society of America.
[32] Habisreuther, T., Hailemichael, E., Ecke, W., Latka, I., Schroder, K., Chojetzki, C., Schuster, K., Rothhardt, M. & Willsch, R. (2012). *ORMOCER coated fiber-optic Bragg grating sensors at cryogenic temperatures*. IEEE Sensors Journal, 12(1), 13-16.
[33] Martins, R., Caldas, P., Teixeira, B., Azevedo, J., Monteiro, J., Belo, J. H., Araujo, J. P., Santos, J. L. & Rego, G. (2015). *Cryogenic temperature response of reflection-based phase-shifted long-period fiber gratings*. Journal of Lightwave Technology, 33(12), 2511-2517.
[34] Mishra, V., Lohar, M., & Amphawan, A. (2016). Improvement in temperature sensitivity of FBG by coating of different materials. Optik-International Journal for Light and Electron Optics, 127(2), 825-828.
[35] Ramalingam, R., & Atrey, M. D. (2017, December). Theoretical analysis and coating thickness determination of a dual layer metal coated FBG sensor for sensitivity enhancement at cryogenic temperatures. In IOP Conference Series: Materials Science and Engineering (Vol. 278, No. 1, p. 012075). IOP Publishing.
[36] Sampath, U., Kim, D., Kim, H., & Song, M. (2018). Polymer-coated FBG sensor for simultaneous temperature and strain monitoring in composite materials under cryogenic conditions. Applied optics, 57(3), 492-497.
[37] Ukil, A., Braendle, H., & Krippner, P. (2012). *Distributed temperature sensing: review of technology and applications*. IEEE Sensors Journal, 12(5), 885-892.
[38] Inaudi, D., & Glisic, B. (2006, July). *Distributed fiber optic strain and temperature sensing for structural health monitoring*. In Proceedings of the Third International Conference on Bridge Maintenance, Safety and Management, Porto, Portugal (pp. 16-19).
[39] Chen, T., Wang, Q., Chen, R., Zhang, B., Lin, Y., & Chen, K. P. (2012). *Distributed liquid level sensors using self-heated optical fibers for cryogenic liquid management*. Applied optics, 51(26), 6282-6289.
[40] Thévenaz, L., Fellay, A., Facchini, M., Scandale, W., Niklès, M., & Robert, P. A. (2002, June). *Brillouin optical fiber sensor for cryogenic thermometry*. In Smart Structures and Materials 2002: Smart Sensor Technology and Measurement Systems (Vol. 4694, pp. 22-28). International Society for Optics and Photonics.
[41] Lu, X., Soto, M. A., & Thévenaz, L. (2014, June). *MilliKelvin resolution in cryogenic temperature distributed fibre sensing based on coherent*

Rayleigh scattering. In 23rd International Conference on Optical Fibre Sensors (Vol. 9157, p. 91573R). International Society for Optics and Photonics.

[42] Turitsyn, S. K., Babin, S. A., El-Taher, A. E., Harper, P., Churkin, D. V., Kablukov, S. I., Ania-Castañón, J.D., Karalekas, V & Podivilov, E. V. (2010). *Random distributed feedback fibre laser*. Nature Photonics, 4(4), 231.

[43] Ahmad, H., Latif, A. A., Zulkifli, M. Z., Awang, N. A., & Harun, S. W. (2012). *Temperature sensing using frequency beating technique from single-longitudinal mode fiber laser*. IEEE Sensors Journal, 12(7), 2496-2500.

[44] Leandro, D., Bravo, M., Ortigosa, A., & Lopez-Amo, M. (2015). *Real-time FFT analysis for interferometric sensors multiplexing*. Journal of Lightwave Technology, 33(2), 354-360.

[45] Lopez-Aldaba, A., Pinto, A. M. R., Lopez-Amo, M., Frazão, O., Santos, J. L., Baptista, J. M., Baierl, H., Auguste, J.L.& Roy, P. (2015). *Experimental and numerical characterization of a hybrid Fabry-Pérot cavity for temperature sensing*. Sensors, 15(4), 8042-8053.

[46] Eickhoff, W., & Ulrich, R. (1981). *Optical frequency domain reflectometry in single-mode fiber*. Applied Physics Letters, 39(9), 693-695.

[47] Gifford, D. K., Kreger, S. T., Sang, A. K., Froggatt, M. E., Duncan, R. G., Wolfe, M. S., & Soller, B. J. (2007, October). *Swept-wavelength interferometric interrogation of fiber Rayleigh scatter for distributed sensing applications*. In Fiber Optic Sensors and Applications V (Vol. 6770, p. 67700F). International Society for Optics and Photonics.

[48] Leandro, D., Bravo, M., & Lopez-Amo, M. (2015). *High resolution polarization-independent high-birefringence fiber loop mirror sensor*. Optics express, 23(24), 30985-30990.

[49] Fu, H., Shu, X., Mou, C., Zhang, L., He, S., & Bennion, I. (2009). *Transversal loading sensor based on tunable beat frequency of a dual-wavelength fiber laser*. IEEE Photonics Technology Letters, 21(14).

[50] Wang, Y., Li, N., Huang, X., & Wang, M. (2015). *Fiber optic transverse load sensor based on polarization properties of π-phase-shifted fiber Bragg grating*. Optics Communications, 342, 152-156.

[51] Chen, L., Huang, L., Gao, L., & Chen, X. (2012, November). *Fiber laser sensor for load measurement based on beat frequency demodulation technique*. In Communications and Photonics Conference (ACP), 2012 Asia (pp. 1-3). IEEE.

[52] Sun, Z., Mou, C., Yan, Z., Zhou, K., Wang, X., Li, J., & Zhang, L. (2015). *Optical loading sensor based on ring-cavity fiber laser incorporating a 45°-tilted fiber polarizing grating*. Applied Optics, 54(13), 4267-4272.

[53] Guan, B. O., Jin, L., Zhang, Y., & Tam, H. Y. (2012). *Polarimetric heterodyning fiber grating laser sensors*. Journal of lightwave technology, 30(8), 1097-1112.

[54] Majumder, M., Gangopadhyay, T. K., Chakraborty, A. K., Dasgupta, K., & Bhattacharya, D. K. (2008). *Fibre Bragg gratings in structural health monitoring—Present status and applications*. Sensors and Actuators A: Physical, 147(1), 150-164.

[55] López-Higuera, J. M., Cobo, L. R., Incera, A. Q., & Cobo, A. (2011). *Fiber optic sensors in structural health monitoring*. Journal of lightwave technology, 29(4), 587-608.
[56] Li, H. N., Li, D. S., & Song, G. B. (2004). *Recent applications of fiber optic sensors to health monitoring in civil engineering*. Engineering structures, 26(11), 1647-1657.
[57] Tennyson, R. C., Mufti, A. A., Rizkalla, S., Tadros, G., & Benmokrane, B. (2001). *Structural health monitoring of innovative bridges in Canada with fiber optic sensors.* Smart materials and Structures, 10(3), 560.
[58] Liu, X., Jin, B., Bai, Q., Wang, Y., Wang, D., & Wang, Y. (2016). *Distributed fiber-optic sensors for vibration detection*. Sensors, 16(8), 1164.
[59] Bao, X., & Chen, L. (2012). *Recent progress in distributed fiber optic sensors*. Sensors, 12(7), 8601-8639.
[60] Juarez, J. C., Maier, E. W., Choi, K. N., & Taylor, H. F. (2005). *Distributed fiber-optic intrusion sensor system*. Journal of lightwave technology, 23(6), 2081-2087.
[61] Peng, F., Duan, N., Rao, Y. J., & Li, J. (2014). *Real-time position and speed monitoring of trains using phase-sensitive OTDR*. IEEE Photonics Technology Letters, 26(20), 2055-2057.
[62] Wang, Z., Lu, B., Zheng, H., Ye, Q., Pan, Z., Cai, H., Ronghui, Q., Fang, Z. & Zhao, H. (2017, April). *Novel railway-subgrade vibration monitoring technology using phase-sensitive OTDR*. In Optical Fiber Sensors Conference (OFS), 2017 25th (pp. 1-4). IEEE.
[63] Liu, T., Wang, F., Yuan, Q., Liu, Y., Zhang, L., & Zhang, X. (2017, August). *Simulation of the performance of phase-sensitive OTDR based on Ultra-weak FBG array using double pulses*. In Optical Communications and Networks (ICOCN), 2017 16th International Conference on (pp. 1-3). IEEE.
[64] Wang, C., Shang, Y., Zhao, W. A., Liu, X. H., Wang, C., Yu, H. H., Yang, M. H. & Peng, G. D. (2018). *Distributed Acoustic Sensor Using Broadband Weak FBG Array for Large Temperature Tolerance*. IEEE Sensors Journal, 18(7), 2796-2800.
[65] Zhang, X., Sun, Z., Shan, Y., Li, Y., Wang, F., Zeng, J., & Zhang, Y. (2017). *A high performance distributed optical fiber sensor based on Φ-OTDR for dynamic strain measurement*. IEEE Photonics J., 9(3), 1-12.
[66] Zhu, F., Zhang, Y., Xia, L., Wu, X., & Zhang, X. (2015). *Improved Φ-OTDR sensing system for high-precision dynamic strain measurement based on ultra-weak fiber Bragg grating array*. Journal of Lightwave Technology, 33(23), 4775-4780.
[67] Wang, C., Shang, Y., Liu, X. H., Wang, C., Yu, H. H., Jiang, D. S., & Peng, G. D. (2015). *Distributed OTDR-interferometric sensing network with identical ultra-weak fiber Bragg gratings*. Optics express, 23(22), 29038-29046.
[68] Erdogan, T. (1997). *Fiber grating spectra*. Journal of lightwave technology, 15(8), 1277-1294.
[69] Yuksel, K., Moeyaert, V., Mégret, P., & Wuilpart, M. (2012). Complete analysis of multireflection and spectral-shadowing crosstalks in a quasi-

distributed fiber sensor interrogated by OFDR. IEEE Sensors Journal, 12(5), 988-995.

[70] De Miguel-Soto, V., Leandro, D., Lopez-Aldaba, A., Beato-López, J. J., Pérez-Landazábal, J. I., Auguste, J. L., Jamier, R., Roy, P. & Lopez-Amo, M. (2017). Study of Optical Fiber Sensors for Cryogenic Temperature Measurements. Sensors, 17(12), 2773.

[71] de Miguel Soto, V., Jason, J., Kurtoğlu, D., Lopez-Amo, M., & Wuilpart, M. (2019). Spectral shadowing suppression technique in phase-OTDR sensing based on weak fiber Bragg grating array. Optics letters, 44(3), 526-529.

[72] Kivilcim, Y., Per-Johan, J. , De Miguel Soto, V., Lopez-Amo, M., Mégret, P. and Wuilpart, M. , "Performance evaluation of phase-OTDR sensing system based on weak fiber Bragg grating array" in IEEE Photonics Society Benelux Chapter 2018, 20-23, Bruxelles, Belgique, 2018

CHAPTER IV

Random distributed-feedback fiber lasers optimization studies for remote sensor monitoring applications

In this chapter, two optimization studies of RDFB-FL structures are presented. Firstly, the performance of a tunable multi-wavelength fiber laser is optimized for later use in a sensor multiplexing network. Secondly, the operation of a novel scheme that combines a double-pumped RDFB-FL and second-order amplification has been analyzed. The objective of this last study is to maximize the output power of the system, allowing to increase the interrogation distance of a remote sensor network. [1]

---

[1]This Chapter has been partially published in the papers entitled: *Fully switchable multi-wavelength fiber lasers based on random distributed feedback for sensors interrogation* in *Journal of Light. Tech.*, *Fully switchable multiwavelength fiber laser assisted by a random mirror* in *Optics Letters* and *Ultra-long (290 km) remote interrogation sensor network based on a random distributed feedback fiber laser* in *Optics Express*.

Chapter IV. Random distributed-feedback fiber lasers optimization studies for remote sensor monitoring applications.

4.1. Introduction

Multi-wavelength fiber lasers (MWFL) have attracted a lot of interest recently due to their great potential in a variety of applications. Among them are included: communications based on wavelength-division-multiplexing (WDM), high resolution spectroscopy and sensor monitoring [1]-[5]. Several researchers have focused their attention on proposing new multi-wavelength sources which allow tuning the output spectrum for sensing purposes [6][7]. In fact, the use of this type of fiber lasers to multiplex fiber optic sensors allows reducing the total cost of the system, by sharing a number of devices of the network.

MWFL can be classified by their gain medium, as well as by the generation process of the emission lines. Some of the gain media used in previous works are: erbium doped fiber [8]-[10], stimulated Raman scattering (SRS) [11]-[13], stimulated Brillouin scattering (SBS) [14] or a hybrid combination of the above [15][16]. Besides, the emission lines can be generated passively or actively. Within the first category, passive filtering systems such as fiber Bragg gratings (FBGs) [17], Fabry-Pérot filters [18], Sagnac loop mirrors [19], and Lyot filters [20]. Then, some examples that would enter into the category of active generation are SBS or four wave mixing [21].

When the emission lines are generated by passive elements, the central wavelength and separation between lines can be simply configured. The reconfiguration of the distance between emission lines is very useful for the aforementioned applications of MWFL. Thus, fiber lasers that can generate a comb of multiple wavelengths with a tunable separation are suitable candidates for dense-wavelength division multiplexing (DWDM) systems [22].

In Table 4. 1, recent works on fixed and tunable multi wavelength lasers are collected. It gathers parameters such as maximum number of emission lines, wavelength range and if power equalization of the emitted lines is applied or not. Finally, the spacing flexibility is also compared.

Year Ref	Princ. Operation	Number emission lines	Range (nm)	Spacing	Equalization
2004 [23]	Semiconductor (SOA)	17	13	Fixed (0.8nm)	No
2012 [24]	Erbium	17	15	Fixed (0.8 or 1nm)	No
2007 [25]	Brillouin-Erbium	70	11	Fixed (0.088nm)	No
2007 [26] [34]	Erbium	11	50	Fixed (0.8nm)	No
2007 [27]	Raman+ Erbium	17 (for 0.4nm spacing)	10	Tunable 0.2,0.4 and 0.8nm	No
2008 [28]	Broadband source	8	19	1.6-9.6nm	No
2009 [29]	Brillouin	5	35	Fixed (0.08nm)	No
2010 [30]	Parametric Amplification	129	25.6	Fixed (0.2nm)	No
2011 [31]	Brillouin-Erbium	150	6	Fixed (0.075nm)	No
2011 [32]	Random DFB-FL	160	16	Fixed (0.09nm)	No
2012 [33]	Erbium	28	10	0.3-1.5nm	No
2014 [34]	**Random DFB-FL**	**18**	**15**	**Tunable**	**Yes**
2015 [35]	**Random DFB-FL**	**25**	**30**	**Tunable**	**Yes**
2016 [36]	Brillouin-Erbium	4	1.1	Tunable	No
2017 [37]	Erbium	4	8	Fixed (1.1nm)	No
2017 [38]	Erbium	14	13	Tunable	No
2017 [39]	Erbium	4	36	Tunable	No
2018 [40]	Erbium	60	5	Tunable	No
2018 [41]	Erbium	48	13	Tunable	No
2018 [42]	Brillouin	7	50	Fixed (0.088nm)	No

2018 [43]	Erbium	11	23	Fixed (1.9nm)	No

Table 4. 1. State of art of reconfigurable multi-wavelength fiber lasers.

As well as multiplexing several sensors, another important challenge in sensor networks is to increase the maximum interrogation distance. Optical amplification is frequently applied in order to reach hundreds of kilometers, such as Erbium doped fiber or semiconductor amplifiers, or those based on Brillouin or Raman effects, or hybrid combinations [44]. Several attempts have been carried out during the last years. For instance, four fiber Bragg gratings were interrogated at a 250 km distance using Raman amplification in [45]. The largest distance reached up to 2018 was 253 km, monitoring only one displacement sensor in [46]. In order to extend the monitoring distance, schemes that use two pump lasers simultaneously have been proposed [47]-[50]. In the same line, higher-order pumping structures [51][52] have been proposed because this procedure reduces the difference between the gain and loss coefficients along the propagation. For instance, it has been exploited in second-order Raman amplification schemes, obtaining quasi-lossless transmission along the fiber [53][54].

Random distributed feedback fiber lasers (RDFB-FL) [55], previously explained in Chapter II Section 2.2.3, have been subject of many studies and experimental investigations during the last years due to their particular properties compared to conventional fiber lasers [56]. Due to the long cavities commonly used, they are especially well suited for ultra-long remote sensing applications [57]-[59]. For this reason, in the present work we have tried to combine the advantages of RDFB-FL for remote sensor monitoring with double-pumped and second order amplification schemes. In this manner, the purpose of our experiments is to extend the interrogation distance of the remote sensor network, surpassing the limits established in previous approaches.

In the following sections, two main optimization experiments are developed. In Section 4.1, a tunable multi-wavelength fiber laser baser on a RDFB-FL is analyzed. The main features of the multi-wavelength fiber laser source such as number of emission lines, output power, separation between lines and wavelength range are examined. Then, a new double-pumped second-order amplification scheme based on a RDFB-FL is detailed in Section 4.2. With the aim of its later use to interrogate a remote sensor network, its optimum point of operation has been obtained.

4.2. Optimization of a fully-switchable multi-wavelength fiber laser source based on a RDFB-FL

In this section, an optimization study of a reconfigurable multi-wavelength fiber laser (MWFL) based on a RDFB-FL is presented. With the aim of using this MWFL to multiplex a remote sensor network, the following parameters have been optimized: wavelength range, number of lines generated, line width and power stability. Although any multi-wavelength configuration can be created with the proposed schemes, the specifications of the ITU grid have been taken as reference. In particular, the separation distances of 200, 100 and 50 GHz between the generated lines were tested.

a. Description of the system

First, two schemes were proposed to carry out the following optimization studies, see Figure 4. 1. Both consist of a forward pumped RDFB-FL, see Chapter II section 2.2.3. In the first one, the Raman gain medium consists of a 50 km SMF coil. In the second one, a fiber spool of 2.5 km of dispersion compensating fiber (DCF) forms the gain medium, presenting a -343ps/(nm·km) first order dispersion coefficient and an effective area of 21μm².

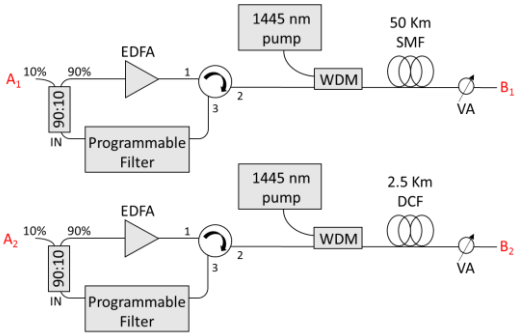

Figure 4. 1. MWFL schemes using two different Raman gain medium.

Both active media act also as a distributed mirror in the laser cavity. The other mirror limiting the cavity is located on the left part of the schemes. It is formed by a fiber loop created by connecting the input and output ports of a circulator, as shown in Figure 4. 1. It performs the filtering of the light in the cavity and selects the profile of the laser spectrum. The dynamic filtering is

achieved by a programmable filter (Finisar 1000S). In addition, an erbium doped fiber amplifier (EDFA) was included in the loop after the filter so a wider combined spectrum is obtained (up to ~30nm), with an output power of 10 dBm. A customized program was developed to control the programmable filter, selecting the comb of desired wavelengths.

b. Experimental results

To begin with, the spectra generated at the output of the proposed schemes were measured, in both cases, with the programmable filter disconnected and injecting a pump power of 1.6 W. The main difference between both spectra is the greater width of the spectrum obtained with the SMF. However, the peak power is reduced compared to the DCF spectrum. The obtained results are shown in Figure 4. 2 a). Besides, the output power evolution with the increasing pump power (see Figure 4. 2 b)) and the power stability (Figure 4. 2 c)) were also obtained. For these measurements, a non-equalized filter of 23 emission lines separated by a distance of 100 GHz was applied (see Figure 4. 6 a)).

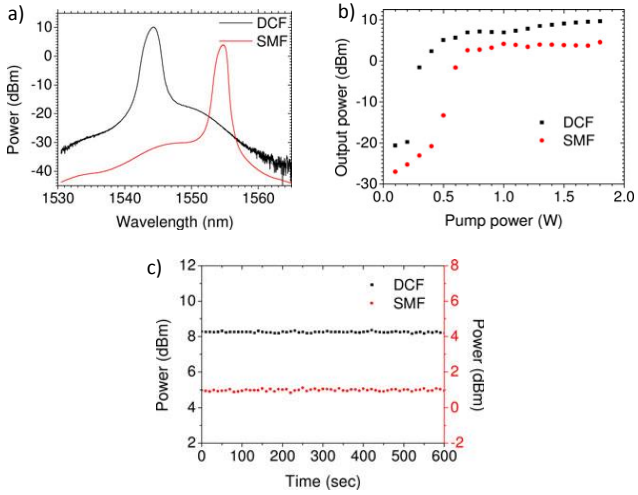

Figure 4. 2. a) Laser spectrum when the programmable filter is off b) laser power evolution versus pump power and c) power stability evolution obtained with both fibers.

The emission line with the highest peak power was tracked. A lower lasing threshold (~200mW) is observed when using DCF instead of SMF as the gain

media. This is due to the fact that the non-linearities are more prominent in the DCF, so the Raman amplification effect is enhanced when this fiber is used. In both cases, the laser behavior is verified. The measured instability of the output power is less than 0.2 dB in both cases, which is in accordance with the usual behavior of RDFB fiber lasers. In order to reduce the power instability of the generated lines, this parameter was analyzed with respect to the injected pump power and depicted in Figure 4. 3.

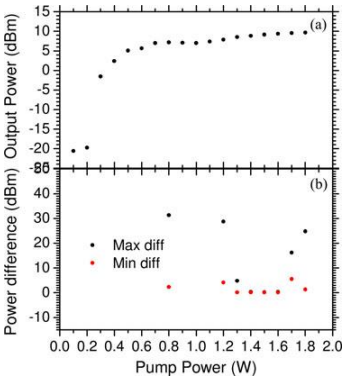

Figure 4. 3. Graphical demonstration of the pump power choice. The lasing power evolution versus the pump power (a) is compared with the system stability (b), which depicts the emitted power difference for the best and worst cases.

From the graph, we can verify that the minimum instability is achieved with pump powers of 1.5 and 1.6 W. Although these pump powers reduce the efficiency of the scheme, greater stability is obtained. For this reason, a pump power of 1.6 W was selected for the following experiments. The power instability at low pump powers is due to the gain competition between the emission lines, caused by a prevalence of the EDFA gain.

Once determined the pump power that minimizes the instability of the system, we continued with the study of the line width. This parameter is of great importance in the design of the fiber laser, since its behavior is related to its line width. The generation of Brillouin scattering and other nonlinear effects are accentuated as the line width is narrowed. This effect cause a greater line depletion as it propagates through the fiber. However, the

greater the width of the emission line, the lower the amplification efficiency, establishing a compromise.

In Figure 4. 4 a), the evolution of the output power with respect to the line width is shown for both fibers at a fixed 1.6W pump power. Optimum values of 0.2 nm and 0.25 nm were obtained for the cases of DCF and SMF, respectively. Nevertheless, more factors must be taken into account when optimizing a MWFL, such as the maximum number of lines generated, stability and pump power needed. For this reason, optimum values of 0.24 nm and 0.17 nm were selected for DCF and SMF, respectively. These values offer the best laser performance, maximizing the number of lines generated and maintaining the power stability. Finally, the emission lines were measured using a high resolution Brillouin optical spectrum analyzer (BOSA), see Figure 4. 4 b). Each line shows a Gaussian distribution, with a measured full width at half maximum (FWHM) of 72.8 pm and a separation between peaks of 0.789 nm. These results confirm a perfect fit with the ITU grid 100 GHz specification.

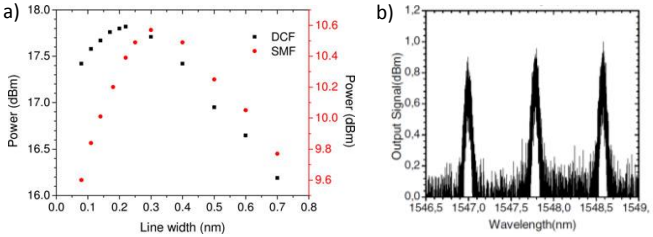

Figure 4. 4. a) One emission line output power evolution when the line width is varied and b) high-resolution measuring of the lasing wavelengths by the BOSA (DCF fiber).

The proposed schemes allow to extract the output signal of the laser both in the header (point A) and at the end of the gain medium (point B), as shown in Figure 4. 1. The results obtained in both points are depicted in Figure 4. 5, with a maximum number of 18 emission lines equalized in power with a separation of 100 GHz between them. Several differences are perceived between both graphs. The most evident is the difference in power, since only 10% of the power present in the laser cavity is detected at point A. On the contrary, all the power is detected in point B. The only advantage of taking point A as the output port is the reduction of noise as well as contributions from four-wave mixing. Considering its use in remote interrogation

applications, it is more interesting to use point B as the output port. For this reason, point B is considered the output port for all the following measurements.

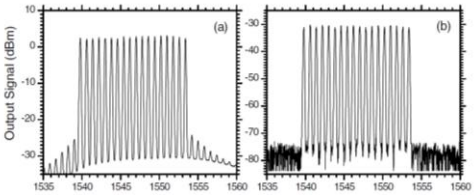

Figure 4. 5. Equalized results for the 100 GHz ITU grid measured in points "B" (a) and "A" (b) labeled in red in Figure 3. 1. with DCF fiber as gain media.

As previously advanced, the developed programmable filter control software includes the function of equalizing the power of the different emission lines. This is a key factor of the system, since it allows to increase the number of emission lines and maintain a flat multi-wavelength spectrum. The operating principle is as follows: the software compares the difference in power between all the lines and the one with the lowest power. Then, it applies a proportional attenuation to each line so that they all present the same power. This process is repeated until the power difference between lines is less than a limit set by the user. This value establishes the precision in the equalization process. It is important to emphasize that the software does not introduce unjustified losses in the cavity.

For the sake of clarity, Figure 4. 6 shows the initial spectrum without equalization, followed by the attenuation profile calculated dynamically by the software and the final spectrum equalized. These graphs were obtained for 23 and 25 emission lines with a separation of 100 GHz for DCF and SMF, respectively. The maximum power difference between lines was fixed to 0.5 dB, considering that this limit should not be lower than the system worst instability. In the same manner, in Figure 4. 7 the maximum number of equalized emission lines with separation of 200 and 100 GHz are shown for both fibers. Finally, the graphs obtained with a 50GHz separation between lines are represented Figure 4. 8. The main differences detected in the graphs comparing both fibers are: the number of emission lines and the output power. Using SMF as the gain media allows a higher number of emission lines, while using DCF provides higher output power.

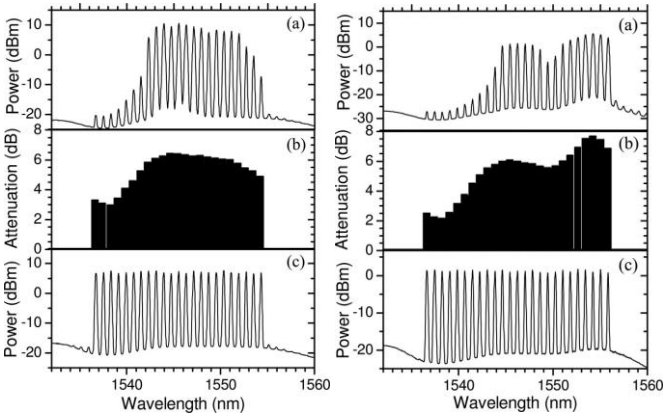

Figure 4. 6. Maximum number of emission lines for the DCF (left column) and SMF (right column) without equalization and the attenuation profile to equalize the spectrum with the result illustrated below.

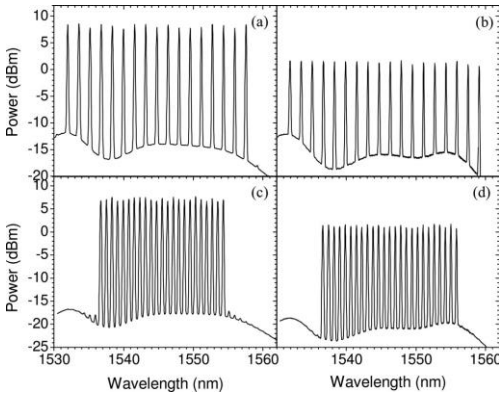

Figure 4. 7. Maximum number of emission lines for the 200 and 100 GHz ITU grid measured for (a) and (c) the DCF and (b) and (d) the SMF.

When the distance between emission lines is reduced, the equalization process becomes more complicated. Due to this fact, a greater difference is observed in the maximum number of equalized lines (11 lines of difference using SMF or DCF fiber) when the separation between lines is 50 GHz. This variance may be caused by the different gain spectra of each fiber, as well as

the arising non-linear effects. In the case of DCF, the amplification is concentrated in a smaller effective area, enhancing the non-linear effects and making the equalization process more challenging. On the contrary, these effects are distributed over a greater fiber length in the SMF case, thus affecting the output spectrum to a minor extent.

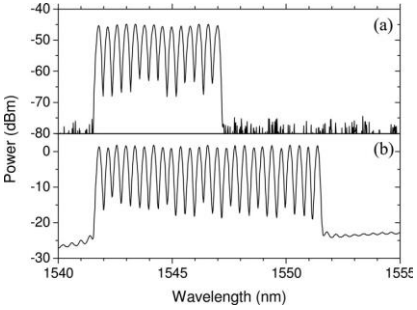

Figure 4. 8. Maximum number of emission lines for the 50 GHz ITU grid measured for the (a) DCF and (b) the SMF.

To conclude this study, we present the experiment that justifies the use of a gain system that combines RDFB and EDFA amplification. First, the stability of both cavities were analyzed individually: the distributed mirror based cavity and the EDFA based linear cavity. A filter of 30 emission lines with a separation of 100 GHz was applied. The output power of the emission lines was monitored for 60 minutes, obtaining the results presented in Figure 4. 9. Gain competition between emission lines is higher in the EDFA based linear cavity causing large instabilities, in contrast to the stable response obtained with RDFB amplification.

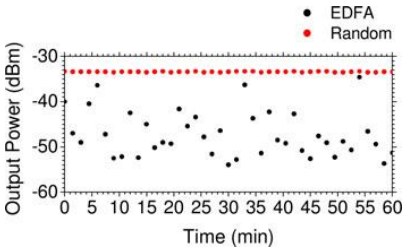

Figure 4. 9. Output power variations of the multi-wavelength random laser in comparison with a non-distributed (EDFA based) laser cavity.

In addition, the spectra obtained with each of the amplification methods were analyzed individually and also combining both, see Figure 4. 10. In this latter case, a wider amplified spectrum is obtained. These results demonstrate the importance of the mixture of both amplification methods to achieve a more stable and wider performance.

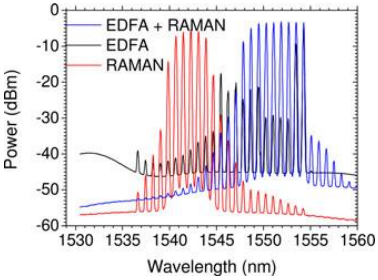

Figure 4. 10. Comparison of different spectra when different amplification media is used.

4.3. Optimization of a double pumped fiber laser source based on a RDFB-FL

In this section, a fully experimental optimization study of a double-pump scheme based on RDFB-FL is presented. The main objective is to determine the configuration that maximizes the output power of the system, for its later use in remote interrogation of sensor networks.

a. Description of the system

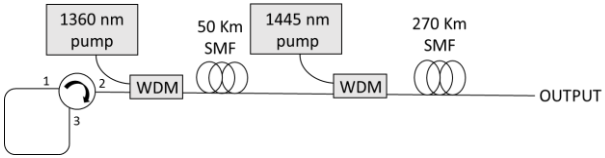

Figure 4. 11. Scheme with two pump lasers analyzed.

A separation distance of 50 Km of SMF between pump lasers was introduced. Previous experiments confirmed the need to use a distance of tens of kilometers between pump lasers to satisfy the laser condition: the distributed gain generated along the fiber must exceed the losses introduced by it. Bearing this in mind, the behavior of the scheme depicted in Figure 4. 11 was analyzed. In addition, the performance of a similar set-up was also tested by inverting the order of the serial pump lasers, i.e. first 1445 nm followed by a 1360 nm pump laser. The results acquired did not improved the ones measured with the previous configuration and led to an unstable laser behavior. As a consequence, we decided to continue with the initial order of pump lasers.

This configuration is a single-arm forward-pumped distributed fiber laser, where a loop mirror recirculates the scattered light back into the cavity. This loop redirects light through port 2 of a 3-port optical circulator. A distributed mirror is formed by the 50 km + 270 km of standard single-mode fiber (Sterlite OH-Lite-E, with an attenuation of 0.19 dB / km), which provides a weak feedback along the fiber due to the effect of Rayleigh scattering, see Chapter II section 2.1.5. Two wavelength division multiplexers (WDM) were used to inject two pump lasers (RLD-5K-1360 and RLD-5K-1445) into the distributed

cavity. As stated before, both WDM are connected in series separated by a reel of 50 Km of SMF fiber.

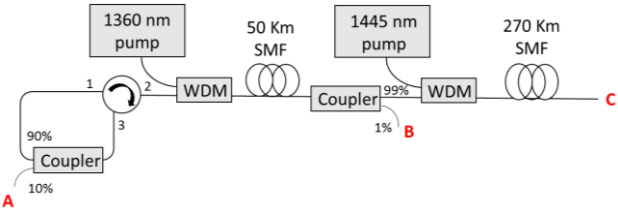

Figure 4. 12. Scheme employed to measure the spectrum at various points of the laser cavity.

The evolution of the spectrum was analyzed by including three measurement points distributed along the laser cavity, i.e. A, B and C in Figure 4. 12 The first one (A) is located in the header. A coupler was employed to extract 10% of the backscattered power, obtaining the results showed in Figure 4. 13. The second measurement point was set just before the WDM injecting the second pump laser (point B in the scheme). Finally, it has been measured the spectrum at the end of the cavity (point C).

b. Experimental results

The graphs depicted in Figure 4. 13 and Figure 4. 14 show the evolution of the spectra for different values of the injected pump powers and the purpose of using a 50 km reel between pump lasers. This fiber allows the generation of a secondary pump near 1445 nm (first Stokes) and initiates the generation of a second Stokes line near 1550 nm. The latter is assisted by the 1445 nm pump laser. In this way, the laser pump at 1445 nm is combined with the first Stokes wave generated by the pump at 1360 nm. The resulting emission generates and amplifies an emission line at 1550 nm along the cavity.

Since this scheme is intended to be used for the remote interrogation of sensor networks, the maximum output peak power detected along the 1550nm- 1560nm band was measured for different pumping combinations with the available pump lasers.

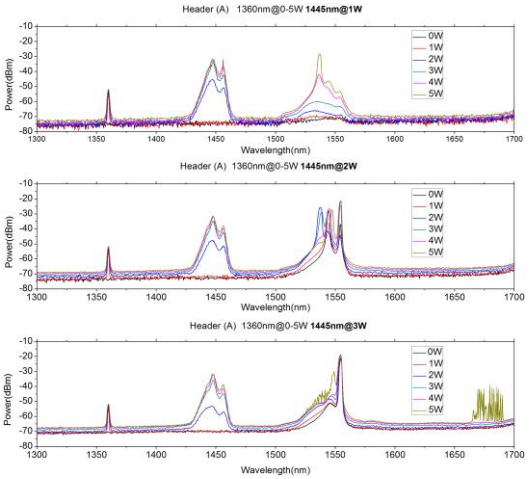

Figure 4. 13. Measured spectra at A, the header of the laser cavity for several pump power combinations.

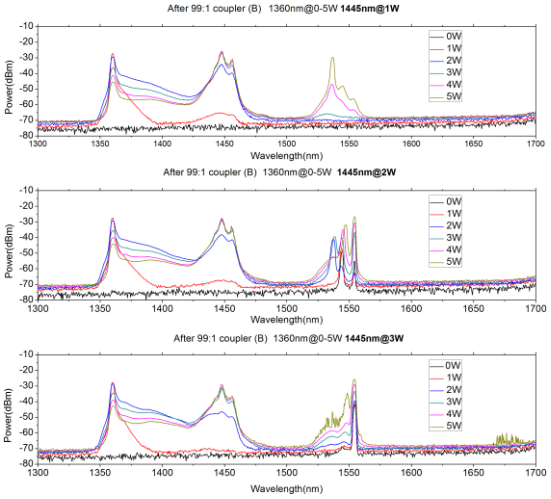

Figure 4. 14. Measured spectra at B, an intermediate point of the laser cavity for several pump power combinations.

In the graphs below, see Figure 4. 15, the maximum power reaching the sensors after 270 km is shown. The graph on the right is just a zoom of the one on the left. Higher pump powers contribute to the generation of gain in the 1650nm-band (third Stokes), which is not desirable for this concrete application. Among all the combinations that provide the same maximum output peak power (1445 nm @3W and 1360nm @≥3W) we have chosen the one that need the lower pump power to get the maximum output power. More pump values could have been tested, and also theoretical analysis could bring more accurate results. However, we considered that experimental results were clear enough to choose adequate values, since differences between the most evident combinations were small.

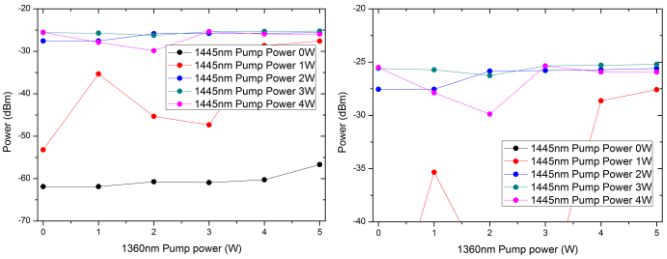

Figure 4. 15. Maximum output peak power measured at point C for many pump power combinations.

4.4. Conclusions

The main objective of this chapter was to optimize RDFB-FL structures for their use in remote sensor interrogation applications. Two studies have been carried out, improving two important aspects in this field, such as increasing the interrogation distance and enhancing the multiplexing capacity of the network.

In section 4.2, a multi-wavelength fiber laser scheme is presented. This study aims to maximize the number of emission lines in the L-band. Two different fibers have been employed as the gain medium of the laser. Although the DCF guaranteed a higher output power, the SMF ended being the best candidate in this particular case. With this fiber, the number of multiplexed sensors can be greater and its low losses per km make it more suitable for long haul applications. Some of the conclusions drawn from the experiments developed are as follows:

- It is of great importance the choice of the gain-media fiber in the RDFB-FL. Due to the nature of this type of lasers, based on Rayleigh scattering along a length of fiber, it affects notably the generated spectrum. In fact, each fiber can lead to a different shape, power and central wavelength of the spectrum, as well as to modify the lasing threshold. This fact need to be considered so the laser cavity is adapted according to the requirements of the application.
- The software developed to control the programmable filter provides great versatility, improving the overall performance of the system. In addition, this method has demonstrated an easy integration and control from the header fiber loop.
- It should be noted that thanks to this software, the MWFL generated can be employed in optical communications applications as well as in multiplexing of sensor networks. The customized filters satisfy the ITU grid specifications, meeting both the separation and width requirements of the channels. The system showed a more convenient performance for separations greater than 100 GHz between lines. Smaller distances enhanced non-linear effects, which decrease the power stability of the emission lines.
- To increase the number of emission lines and thus extend the multiplexing capacity of the system, two methods have been combined. First, a hybrid amplification scheme was tested: RDFB-FL together with EDFA amplification. The results showed a wider output spectrum. However, its non-flat profile leaves the lines located at the lower and upper ends of the gain spectrum unusable. This inconvenient has been solved through the power equalization of the emission lines, exchanging power between them and thus increasing the number of usable lines.

In section 4.3, an experimental optimization study of a RDFB-FL structure for long-haul applications is presented. On this occasion, the aim of the experiment was to increase the output power so greater monitoring distances can be applied. In previous works, sensors located at a distance of 250 Km were interrogated using a single pump laser at 1445nm. In other proposals, second order laser generation or double pumped schemes were employed to improve the monitoring distance [47]-[54]. As a result, the work presented in this section offers a new scheme that increases the interrogation distance, combining the two ideas mentioned before. This system uses two pump lasers connected in series and takes advantage of second-order laser generation. The order of the pump lasers, their separation distance as well as the pump powers injected were optimized. The conclusions derived from this optimization study are:

- There must be a distance of tens of kilometers between the pump lasers connected in series. First Stokes laser generation must be achieved in the fiber section that separates both pump lasers. In this manner, the generated signal (first stokes) will be reinforced by the following pump laser.
- Theoretical and simulation studies could be carried out to try to improve the obtained results.

As a final conclusion, the studies presented in this chapter improve some features of previous works, such as the number of emission lines, flexibility, bandwidth, low gain competition between lines and output powers. All these progresses can be used for remote interrogation applications of sensor networks, improving the results reported previously.

These results have originated the publications in references [34][35][60].

4.5. References

[1] Staring, A. A. M., Spiekman, L. H., Binsma, J. J. M., Jansen, E. J., Van Dongen, T., Thijs, P. J. A., ... & Verbeek, B. H. (1996). A compact nine-channel multiwavelength laser. IEEE Photonics Technology Letters, 8(9), 1139-1141.

[2] Zirngibl, M., Joyner, C. H., Doerr, C. R., Stulz, L. W., & Presby, H. M. (1996, April). A 18 channel multi frequency laser. In Integrated Photonics Research (p. IMG1). Optical Society of America.

[3] De Matos, C. J. S., Chestnut, D. A., Reeves-Hall, P. C., Koch, F., & Taylor, J. R. (2001). Multi-wavelength, continuous wave fibre Raman ring laser operating at 1.55/spl mu/m. Electronics Letters, 37(13), 825-826.

[4] Han, Y. G., Kim, C. S., Kang, J. U., Paek, U. C., & Chung, Y. (2003). Multiwavelength Raman fiber-ring laser based on tunable cascaded long-period fiber gratings. IEEE Photonics Technology Letters, 15(3), 383-385.

[5] An, H. L., Lin, X. Z., Pun, E. Y. B., & Liu, H. D. (1999). Multi-wavelength operation of an erbium-doped fiber ring laser using a dual-pass Mach–Zehnder comb filter. Optics communications, 169(1-6), 159-165.

[6] Talaverano, L., Abad, S., Jarabo, S., & Lopez-Amo, M. (2001). Multiwavelength fiber laser sources with Bragg-grating sensor multiplexing capability. Journal of lightwave technology, 19(4), 553-558.

[7] Han, Y. G., Tran, T. V. A., Kim, S. H., & Lee, S. B. (2005). Multiwavelength Raman-fiber-laser-based long-distance remote sensor for simultaneous measurement of strain and temperature. Optics letters, 30(11), 1282-1284.

[8] Bellemare, A., Karásek, M., Rochette, M., Lrochelle, S. A. L. S., & Têtu, M. (2000). Room temperature multifrequency erbium-doped fiber lasers anchored on the ITU frequency grid. Journal of lightwave technology, 18(6), 825-831.

[9] Dong, X. P., Li, S., Chiang, K. S., Ng, M. N., & Chu, B. C. B. (2000). Multiwavelength erbium-doped fibre laser based on a high-birefringence fibre loop mirror. Electronics Letters, 36(19), 1609-1610.

[10] Moon, D. S., Paek, U. C., & Chung, Y. (2004). Multi-wavelength lasing oscillations in an erbium-doped fiber laser using few-mode fiber Bragg grating. Optics Express, 12(25), 6147-6152.

[11] Han, Y. G., Kim, C. S., Kang, J. U., Paek, U. C., & Chung, Y. (2003). Multiwavelength Raman fiber-ring laser based on tunable cascaded long-period fiber gratings. IEEE Photonics Technology Letters, 15(3), 383-385.

[12] Dong, X., Shum, P., Ngo, N. Q., & Chan, C. C. (2006). Multiwavelength Raman fiber laser with a continuously-tunable spacing. Optics express, 14(8), 3288-3293.

[13] Chen, D., Qin, S., Shen, L., Chi, H., & He, S. (2006). An all-fiber multi-wavelength Raman laser based on a PCF sagnac loop filter. Microwave and optical technology letters, 48(12), 2416-2418.

[14] Shirazi, M. R., Shahabuddin, N. S., Aziz, S. N., Thambiratnam, K., Harun, S. W., & Ahmad, H. (2008). A linear cavity Brillouin fiber laser with multiple wavelengths output. Laser Physics Letters, 5(5), 361-363.
[15] Cowle, G. J., & Stepanov, D. Y. (1996). Multiple wavelength generation with Brillouin/erbium fiber lasers. IEEE Photonics Technology Letters, 8(11), 1465-1467.
[16] Han, Y. G., Lee, J. H., Lee, S. B., Potì, L., & Bogoni, A. (2007). Novel multiwavelength erbium-doped fiber and Raman fiber ring lasers with continuous wavelength spacing tunability at room temperature. Journal of lightwave technology, 25(8), 2219-2225.
[17] Wang, Z., Cui, Y., Yun, B., & Lu, C. (2005). Multiwavelength generation in a Raman fiber laser with sampled Bragg grating. IEEE photonics technology letters, 17(10), 2044-2046.
[18] Pan, S., Lou, C., & Gao, Y. (2006). Multiwavelength erbium-doped fiber laser based on inhomogeneous loss mechanism by use of a highly nonlinear fiber and a Fabry-Perot filter. Optics express, 14(3), 1113-1118.
[19] Kim, C. S., Sova, R. M., & Kang, J. U. (2003). Tunable multi-wavelength all-fiber Raman source using fiber Sagnac loop filter. Optics communications, 218(4-6), 291-295.
[20] Kim, C. S., & Kang, J. U. (2004). Multiwavelength switching of Raman fiber ring laser incorporating composite polarization-maintaining fiber Lyot-Sagnac filter. Applied optics, 43(15), 3151-3157.
[21] Han, Y. G., Tran, T. V. A., & Lee, S. B. (2006). Wavelength-spacing tunable multiwavelength erbium-doped fiber laser based on four-wave mixing of dispersion-shifted fiber. Optics letters, 31(6), 697-699.
[22] Kartalopoulos, S. V. (2003). DWDM: networks, devices, and technology. Wiley: IEEE Press.
[23] Lee, Y. W., Jung, J., & Lee, B. (2004). Multiwavelength-switchable SOA-fiber ring laser based on polarization-maintaining fiber loop mirror and polarization beam splitter. IEEE Photonics Technology Letters, 16(1), 54-56.
[24] Han, Y. G., & Lee, S. B. (2005). Flexibly tunable multiwavelength erbium-doped fiber laser based on four-wave mixing effect in dispersion-shifted fibers. Optics express, 13(25), 10134-10139.
[25] Zhang, Z., Zhan, L., & Xia, Y. (2007). Tunable self-seeded multiwavelength Brillouin-erbium fiber laser with enhanced power efficiency. Optics express, 15(15), 9731-9736.
[26] Feng, X., Lu, C., Tam, H. Y., & Wai, P. K. A. (2007). Reconfigurable microwave photonic filter using multiwavelength erbium-doped fiber laser. IEEE Photonics Technology Letters, 19(17), 1334-1336.
[27] Chen, D., Qin, S., & He, S. (2007). Channel-spacing-tunable multi-wavelength fiber ring laser with hybrid Raman and Erbium-doped fiber gains. Optics Express, 15(3), 930-935.
[28] Liu, D., Ngo, N. Q., & Tjin, S. C. (2008). A reconfigurable multiwavelength fiber laser with switchable wavelength channels and tunable wavelength spacing. Optics Communications, 281(18), 4715-4718.

[29] Ajiya, M., Mahdi, M. A., Al-Mansoori, M. H., Mokhtar, M., & Hitam, S. (2009). Broadly tunable multiple wavelength Brillouin fiber laser exploiting erbium amplification. JOSA B, 26(9), 1789-1794.
[30] Li, J., & Chen, L. R. (2010). Tunable and reconfigurable multiwavelength fiber optical parametric oscillator with 25 GHz spacing. Optics letters, 35(11), 1872-1874.
[31] Tang, J., Sun, J., Zhao, L., Chen, T., Huang, T., & Zhou, Y. (2011). Tunable multiwavelength generation based on Brillouin-erbium comb fiber laser assisted by multiple four-wave mixing processes. Optics express, 19(15), 14682-14689.
[32] Pinto, A. M., Frazão, O., Santos, J. L., & Lopez-Amo, M. (2011). Multiwavelength Raman fiber lasers using Hi-Bi photonic crystal fiber loop mirrors combined with random cavities. Journal of Lightwave Technology, 29(10), 1482-1488.
[33] Abreu-Afonso, J., Díez, A., Cruz, J. L., & Andrés, M. V. (2012). Continuously tunable microwave photonic filter using a multiwavelength fiber laser. IEEE Photonics Technology Letters, 24(23), 2129-2131.
[34] DeMiguel-Soto, V., Bravo, M., & Lopez-Amo, M. (2014). Fully switchable multiwavelength fiber laser assisted by a random mirror. Optics letters, 39(7), 2020-2023.
[35] Bravo, M., de Miguel Soto, V., Ortigosa, A., & Lopez-Amo, M. (2015). Fully Switchable Multi-Wavelength Fiber Lasers Based on Random Distributed Feedback for Sensors Interrogation. Journal of Lightwave Technology, 33(12), 2598-2604.
[36] Wang, X., Yang, Y., Liu, M., Yuan, Y., Sun, Y., Gu, Y., & Yao, Y. (2016). Frequency spacing switchable multiwavelength Brillouin erbium fiber laser utilizing cascaded Brillouin gain fibers. Applied optics, 55(23), 6475-6479.
[37] Lian, Y., Ren, G., Zhu, B., Gao, Y., Jian, W., Ren, W., & Jian, S. (2017). Switchable multiwavelength fiber laser using erbium-doped twin-core fiber and nonlinear polarization rotation. Laser Physics Letters, 14(5), 055101.
[38] Li, Y., Tian, J., Quan, M., & Yao, Y. (2017). Tunable multiwavelength Er-doped fiber laser with a two-stage Lyot filter. IEEE Photonics Technology Letters, 29(3), 287-290.
[39] He, W., Shangguan, C., Zhu, L., Dong, M., & Luo, F. (2017). Tunable and stable multi-wavelength erbium-doped fiber laser based on a double Sagnac comb filter with polarization-maintaining fibers. Optik-International Journal for Light and Electron Optics, 137, 254-261.
[40] Luo, X., Tuan, T. H., Saini, T. S., Nguyen, H. P. T., Suzuki, T., & Ohishi, Y. (2018). Spacing-adjustable multi-wavelength erbium-doped fiber laser using a fiber Michelson interferometer. Applied Physics Express, 11(8), 082501.
[41] Li, Y., Xu, Z., Luo, Y., Xiang, Y., Yan, Z., Liu, D., & Sun, Q. (2018). Tunable multiwavelength fiber laser based on a θ-shaped microfiber filter. Applied Physics B, 124(6), 109.
[42] Ji, Z., Deng, Y., Wan, H., & Zhang, Z. (2018, October). Tunable multiwavelength Brillouin random fiber laser. In 2018 Asia Communications and Photonics Conference (ACP) (pp. 1-3). IEEE.

[43] Xu, Z., Yu, C., Huang, W., & Chen, D. (2018). Tunable multi-wavelength Er-doped fiber laser based on a fiber taper. Journal of Optics, 20(8), 085701.
[44] Fernandez-Vallejo, M., & Lopez-Amo, M. (2012). Optical fiber networks for remote fiber optic sensors. Sensors, 12(4), 3929-3951.
[45] M. Fernandez-Vallejo, S. Rota-Rodrigo, M. Lopez-Amo, "Remote (250 km) fiber Bragg grating multiplexing system, "Sensors, 11(9), 8711-8720, (2011).
[46] M. Bravo, J. M. Baptista, J. L. Santos, M. Lopez-Amo, O. Frazão, "Ultralong 250 km remote sensor system based on a fiber loop mirror interrogated by an optical time-domain reflectometer," Optics letters, 36(20), 4059-4061, (2011).
[47] Jia, X. H., Rao, Y. J., Wang, Z. N., Zhang, W. L., Jiang, Y., Zhu, J. M., & Yang, Z. X. (2012, October). Towards fully distributed amplification and high-performance long-range distributed sensing based on random fiber laser. In OFS2012 22nd International Conference on Optical Fiber Sensors (Vol. 8421, p. 842127). International Society for Optics and Photonics.
[48] El-Taher, A. E., Alcon-Camas, M., Babin, S. A., Harper, P., Ania-Castanón, J. D., & Turitsyn, S. K. (2010). Dual-wavelength, ultralong Raman laser with Rayleigh-scattering feedback. Optics letters, 35(7), 1100-1102.
[49] Ania-Castanón, J. D., Ellingham, T. J., Ibbotson, R., Chen, X., Zhang, L., & Turitsyn, S. K. (2006). Ultralong Raman fiber lasers as virtually lossless optical media. Physical review letters, 96(2), 023902.
[50] Turitsyn, S. K., Ania-Castañón, J. D., Babin, S. A., Karalekas, V., Harper, P., Churkin, D., ... & Mezentsev, V. K. (2009). 270-km ultralong Raman fiber laser. Physical review letters, 103(13), 133901.
[51] Bouteiller, J. C., Brar, K., & Headley, C. (2002, September). Quasi-constant signal power transmission. In Optical Communication, 2002. ECOC 2002. 28th European Conference on (Vol. 3, pp. 1-2). IEEE.
[52] Chestnut, D. A., de Matos, C. J. S., Reeves-Hall, P. C., & Taylor, J. R. (2002). Copropagating and counterpropagating pumps in second-order-pumped discrete fiber Raman amplifiers. Optics letters, 27(19), 1708-1710.
[53] Martin-Lopez, S., Alcon-Camas, M., Rodriguez, F., Corredera, P., Ania-Castañon, J. D., Thévenaz, L., & Gonzalez-Herraez, M. (2010). Brillouin optical time-domain analysis assisted by second-order Raman amplification. Optics express, 18(18), 18769-18778.
[54] Ania-Castañón, J. D. (2004). Quasi-lossless transmission using second-order Raman amplification and fibre Bragg gratings. Optics Express, 12(19), 4372-4377.
[55] Turitsyn, S. K., Babin, S. A., El-Taher, A. E., Harper, P., Churkin, D. V., Kablukov, S. I., ... & Podivilov, E. V. (2010). Random distributed feedback fibre laser. Nature Photonics, 4(4), 231.
[56] Turitsyn, S. K., Babin, S. A., Churkin, D. V., Vatnik, I. D., Nikulin, M., & Podivilov, E. V. (2014). Random distributed feedback fibre lasers. Physics Reports, 542(2), 133-193.

[57] Fernandez-Vallejo, M., Bravo, M., & Lopez-Amo, M. (2013). Ultra-long laser systems for remote fiber Bragg gratings arrays interrogation. IEEE Photonics Technology Letters, 25(14), 1362-1364.
[58] Leandro, D., deMiguel Soto, V., Perez-Herrera, R. A., Acha, M. B., & López-Amo, M. (2016). Random DFB fiber laser for remote (200 km) sensor monitoring using hybrid WDM/TDM. Journal of Lightwave Technology, 34(19), 4430-4436.
[59] Wang, Z. N., Rao, Y. J., Wu, H., Li, P. Y., Jiang, Y., Jia, X. H., & Zhang, W. L. (2012). Long-distance fiber-optic point-sensing systems based on random fiber lasers. Optics express, 20(16), 17695-17700.
[60] DeMiguel-Soto, V., Leandro, D., & Lopez-Amo, M. (2018). Ultra-long (290 km) remote interrogation sensor network based on a random distributed feedback fiber laser. Optics express, 26(21), 27189-27200.

Some figures included in this chapter are reprinted with permission from ref [34], OSA.

CHAPTER V

Random distributed-feedback fiber lasers for remote monitoring applications

In this chapter, new systems are proposed to improve both the multiplexing capacity and the remote monitoring distance of fiber optic sensor networks. All the presented schemes have in common the use of random distributed-feedback fiber lasers for the interrogation of the sensor structure. The advantageous features of this type of lasers for long distance applications are exploited to reach a maximum monitoring distance of 290 km, establishing a new distance milestone in remote sensing networks.[1]

---

[1]This Chapter has been partially published in the papers entitled: *Fully switchable multi-wavelength fiber lasers based on random distributed feedback for sensors interrogation* and *Random DFB fiber laser for remote (200 km) sensor monitoring using hybrid WDM/TDM* both in *Journal of Light. Tech.* and *Ultra-long (290 km) remote interrogation sensor network based on a random distributed feedback fiber laser* in *Optics Express*.

Chapter V. Random distributed-feedback fiber lasers for remote monitoring applications.

5.1. Introduction

A remote monitoring system presents the ability to observe and verify the performance or quality of any structure located hundreds of kilometers away from a central station. This capability can be exploited in many applications for the control of structures as well as to avoid possible disasters. Some of the most widespread ones include structural health monitoring of bridges, tunnels and oil or gas pipelines [1]-[8], tsunami detection [9]-[10], railway maintenance [11]-[12] and geodynamic control [13]-[14], to name but a few.

Optical fiber offers helpful features for these applications, fulfilling a double functionality. Not only can it be part of the sensor structure but it also forms the communication channel between the detection site and the central station. Thus, it removes the logistical inconvenience of electrical power supply in remote locations. However, increasing the interrogation distance can become a challenge. Another important property of sensor networks is their competence for recovery or self-healing, as well as multiplexing as many sensors as possible. Resilience guarantees the continuity of the service in case of failure of the network. This is of great importance when the monitored structure is of high value or in critical human safety situations. Some work has been done to improve this capacity [15]-[18], although more research should be addressed combining long distance and resilience [16]. Multiplexing allows to interrogate two or more sensors using a single monitoring station [19]-[26]. As a result, the cost per sensor and the network complexity are reduced. In addition, some constructions present large dimensions so numerous sensors are needed to monitor the entire structure.

Sensor networks can be classified by different criteria (Chapter II, section 2.1): types of sensors used (point or distributed), amplification mechanism (Raman, Brillouin, SOAs, Erbium or hybrid combinations), network topology (star, bus and double-bus/ladder) as well as multiplexing technique (Wavelength division multiplexing (WDM), time division multiplexing (TDM), frequency division multiplexing (FDM), coherence division multiplexing (CDM), polarization division multiplexing (PDM) or a combination of them).

In previous reviews [27]-[30], the most outstanding contributions about sensor networks have been gathered. In this chapter, we will focus on remote sensor networks that involve random distributed feedback fiber lasers (RDFB-FL). In Table 5. 1, the state of art of RDFB-FL sensor networks is presented. The references in bold refer to the work developed in this thesis.

Year Ref	Amplif. Method	Type sensor	Num. of sensor	Mux tech.	Network topology	Network length (km)
2011 [31]	Raman	FBG	1	-	Bus	150
2012 [32]	Raman	FBG	2	WDM	Bus	100
2013 [33]	Raman	FBG	11	WDM	Ladder	200
2015 [34]	**Raman+ EDFA**	**FBG+ Inter.**	**7+11**	**WDM/ TDM**	**Ladder**	**50**
2016 [35]	**Raman**	**FBG**	**9 10**	**WDM/ TDM**	**Bus**	**170 200**
2016 [36]	**Raman+ EDFA**	**Inter.**	**1**	**-**	**Ladder**	**225**
2018 [37]	**Raman**	**Inter.**	**1 2**	**CDM**	**Ladder**	**290 270**

Table 5. 1. State of art of remote sensing networks with RDFB-FL

In the following sections, several fiber optic sensor networks based on RDFB-FL are proposed. Different types of sensors and multiplexing techniques have been combined, offering enough flexibility to get an optimal scheme for each required application. The previous longest distance achieved by Bravo et al. in [38] has been surpassed in this work, establishing a new distance milestone. In addition, the compatibility of RDFB-FL with a large variety of multiplexing techniques has been demonstrated.

The developed works are presented from the shortest to the largest monitoring distance achieved, detailing in each case the multiplexing techniques employed.

5.2. Fully switchable multi-wavelength fiber laser for remote (50 km) sensor interrogation

Multi-wavelength lasers show a great potential for communication channels that implement wavelength division multiplexing (WDM) and also for sensor networks. In Chapter IV section 4.1, a brief state of the art of this type of lasers is presented. Below, the characterization and experimental demonstration of a fully-switchable multi-wavelength fiber laser (MWFL) based on a RDFB-FL is performed. In addition, it has been used for the first time as proof of concept for the multiplexing of two remote sensor networks of different technologies.

a. Description of the system

The scheme of the laser structure proposed is shown in Figure 5. 1. The programmable filter selects the profile of the spectrum and allows an easy reconfiguration of it. On the other hand, the EDFA contributes with its broad gain spectrum and widens the initial bandwidth of the generated RDFB-FL, as it was explained in Chapter IV Section 4.2. This allows multiplexing a greater number of sensors and facilitates the power equalization of all the generated channels. The distributed mirror for the laser generation is formed by a SMF spool, achieving a remote monitoring distance of 50 km.

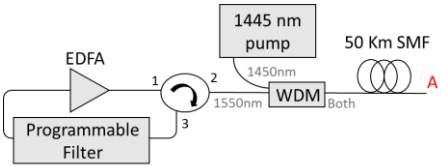

Figure 5. 1. Schematic representation for the multi-wavelength RDFB-FL.

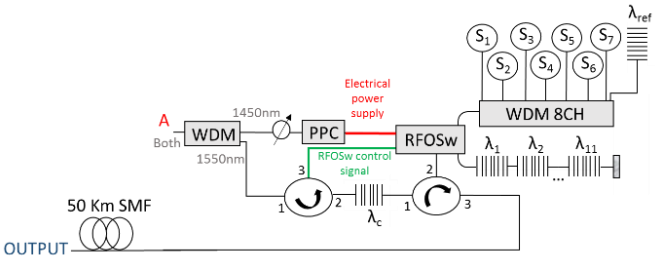

Figure 5. 2. Schematic setup: proof of concept of the remote sensor network.

Figure 5. 2 displays the proposed remote multiplexing sensor networks. These networks are connected to the RDFB-FL in Figure 5. 1 at point A. Both sensor networks are based on completely different operation modes: 7 high birefringence photonic crystal fiber (Hi-Bi PCF) intensity based strain sensors (SN_1) and an array of 11 fiber Bragg gratings (FBG) temperature/strain sensors (SN_2). They are both connected to a remote powered by light fiber optic switch (RFOSw), which commutes and selects the network to be monitored. The residual Raman pump, extracted from the distributed mirror by the 1445 port of a 1445/1550 WDM, feeds the RFOSw, as previously reported in [39]. The RFOSw converts 125 mW of the residual Raman pump into 35 mW of electrical power using a photovoltaic power converter (PCC) PCC9LW made by JDSU. The laser signal enters an optical circulator and illuminates the selected sensor network. Only if SN_1 wants to be monitored, a control signal centered at λ_c will be generated in the multi-wavelength RDFB-FL and enter the first circulator. Then, it would be reflected by the FBG located afterwards and redirected to the control port of the optical switch. Therefore, when the control signal is ON, the Hi-Bi PCF sensor network is selected (SN_1) and when is OFF, the FBG sensors array is interrogated (SN_2). The second circulator illuminates and collects the responses of the selected sensor network. This information is send to the output of the system placed at the header through a 50 km SMF spool.

Hi-Bi sensor Network

The Hi-Bi PCF sensor network consists of seven PCF interferometric strain sensors. They are formed of ~1.5 m of Hi-Bi PCF (PM-1550-01 from NKT Photonics) connected into a Sagnac loop mirror structure (Chapter II, section 2.1.2). A fixed wavelength illuminates each interferometer connected to an 8-channel WDM (from 1536.61 to 1547.72 in 200 GHz ITU grid spec.). The free channel was connected to a FBG which acts as a reference. When strain is applied to the fiber loop, a shift in the interference pattern is caused. Accordingly, the amplitude of the incident wavelength is modulated proportionally to the interference position. Measuring the intensity variation of each wavelength, the applied strain can be determined.

FBG sensor Network

In this case, the laser performs a discrete wavelength sweep to interrogate the 11 FBGs, with a resolution of 0.01 nm. A total of 1500 emission lines are needed to scan the total bandwidth of the sensor network.

a. Experimental results

Figure 5. 3 shows some examples of the spectra that we can generate using this laser structure. On the one hand, Figure 5. 3 a) shows the emission line generated to interrogate the SN_2, performing a wavelength sweep. On the other hand, Figure 5. 3 b) shows the spectrum of the emission lines generated to interrogate SN_1. It displays the 7 lines that monitor each of the interferometric sensors and the emission line corresponding to the reference FBG. Figure 5. 3 c) and d) are examples of some of the emission lines combinations that can be obtained with this laser scheme, demonstrating its high versatility. It is important to note that an equalization of the generated emission lines has been carried out thanks to the development of a customized software implemented in the programmable filter. This technique has allowed to increase the number of emission lines generated, achieving a better use of the total power of the system, as explained previously in Chapter IV section 4.2.

The characterization of the 7 interferometers as strain sensors is depicted in Figure 5. 4. To perform the strain measurements, 10 cm of each sensing fiber was glued to a high precision translation stage with a resolution of 0.017 mε/step. The results show a sensitivity of ~2.23 dB/mε with a measurement uncertainty of 0.09 mε. The use of a WDM allows multiplexing all the sensors without crosstalk, which is demonstrated in Figure 5. 5.

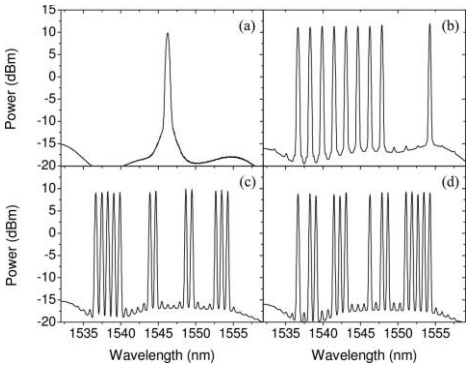

Figure 5. 3. Different emission lines configurations measured in A. (a) Single wavelength, (b) nine wavelengths, (c) 11 wavelengths, (d) 14 wavelengths.

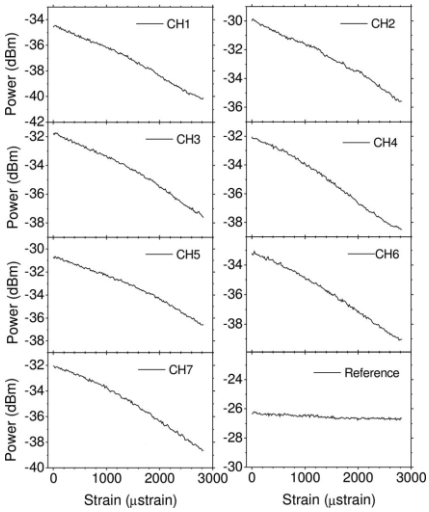

Figure 5. 4. Seven HiBi PCF strain sensors power evolution versus strain and reference channel's FBG reflection.

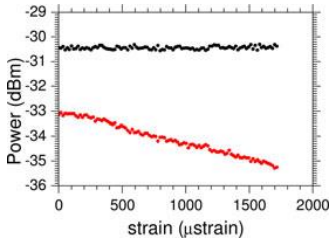

Figure 5. 5. System's crosstalk free demonstration. It is illustrated the CH6 strain sensor result (red line) and CH1 sensor response (black line) while it is not stressed.

In the same manner, the behavior of the FBG sensor network was analyzed. Eleven wavelength sweeps were carried out to identify the position of each FBG maximum. A reconstruction of the 11 FBG reflection spectra is presented in Figure 5. 6, when the discrete wavelength sweep emission line fit each FBG maximum. Since all the FBGs present a similar behavior, we will show only the response to the temperature of one of them (centered at 1546.4nm at room temperature). Figure 5. 7 represents the maximum wavelength measured for the increasing temperature applied to the sensor. The obtained thermal

sensitivity of ~0.01 nm/°C agrees with the expected. A maximum resolution of 1°C was estimated. Therefore, the presented results validate this proof of concept sensor network for remote sensor multiplexing applications.

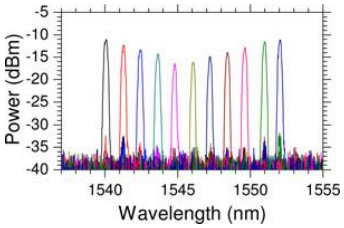

Figure 5. 6. Spectral composition of the FBG sensors network interrogation result.

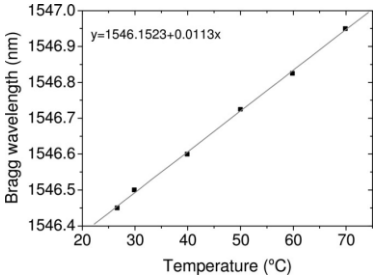

Figure 5. 7. Temperature response of the 1546.4 nm FBG sensor.

5.3. Remote (200 km) sensor monitoring using hybrid WDM/TDM

One of the main drawbacks of ultra-long range remote sensing applications is their limited multiplexing capability. For instance, WDM is limited by the available bandwidth of the light sources employed. In the same manner, TDM systems suffer from transmission loss and are limited by the intensity of the light source. For this reason, the combination of two or more multiplexing techniques may help to overcome the limitations that each technique presents individually. Hybrid WDM/TDM schemes have been validated theoretically to multiplex hundreds of sensors in a single network. In fact, it has been demonstrated through simulations that optical wave time domain reflection technology (OWTDR) can be used to multiplex up to 1000 Bragg gratings of weak reflection into a single fiber [40]. The use of Optical time domain reflectometry (OTDR) allows to achieve fully distributed sensing along a fiber. However, this technique is limited in distance because of the compromise between the pulse-width and the sensing distance.

Bearing this in mind, the combination of OTDR techniques with RDFB-FL could present a great advantage for remote sensing applications. Here, the modulation of the cavity of a RDFB-FL has allowed to identify up to 10 sensors by means of time-domain reflectometry, reaching a 200 km monitoring distance. Two experiments have been developed in the context of this work. The first approach aims to demonstrate the validity of the system to interrogate remote sensors that operate in reflection and monitor them using time and wavelength-division multiplexing. On the contrary, the objective of the second experiment is to increase the wavelength range of the system as well as the distance to the sensors.

a. Description of the system

The sensor multiplexing scheme developed in this work can be divided in two parts: the laser and the sensor network. They are described in the following subsections together with the principle of operation of the interrogation technique.

Lasers design

As in previous schemes, a single-arm forward-pumped RDFB-FL is used as the light source (Chapter II, section 2.2.3). The distributed laser cavity is part of the sensor network, in which numerous sensors can be multiplexed. The

scheme of the laser used in both experiments is essentially the same, changing the technique that selects the central wavelength of the laser. First, a tunable FBG connected to a 4-port circulator filters and selects the laser wavelength, as shown in Figure 5. 8 a). In the second experiment, see Figure 5. 8 b), a programmable filter connected to a 3-port circulator performs the filtering function.

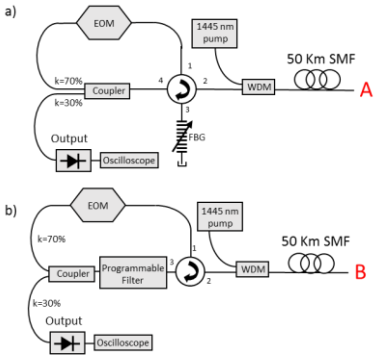

Figure 5. 8. Experimental setup of the proposed fiber laser in the (a) first and (b) second experiment using hybrid WDM/TDM. EOM: Electro-optical modulator, WDM: Wavelength division multiplexer, SMF: Single mode fiber, FBG: Fiber Bragg grating.

Then, an optical coupler is employed to extract 30% of the power that circulates inside the loop, which is later detected and analyzed in an oscilloscope. The remaining 70% of the light is redirected to the loop to be modulated by an electro-optical amplitude modulator (EOM). A signal generator is connected to the modulator creating a train of pulses with a repetition frequency of 450 Hz and a pulse duration of 0.83 and 0.44 µs for the first and second experiment, respectively. Finally, the light passes through the circulator to the laser cavity where it is combined with the 1445 nm pump laser. The cavity consists of a total of 170 and 200 km of single-mode fiber for the first and second experiments, respectively. Therefore, a tunable and amplitude-modulated RDFB-FL emission is obtained at point A and B of each laser scheme.

Sensor networks configuration

Two different sensor networks were designed to perform the validation experiments. The sensor networks include fiber Bragg gratings centered at

diverse wavelengths and located at different distances from the monitoring station. It is worth mentioning that the design of the network allows to include sensors in any position of the cavity up to 200 km, depending on the requirements of the application. Optical couplers are placed throughout the cavity, which allows a percentage of the transmitted light to be extracted to interrogate each group of sensors. Besides, the coupling ratio is an important factor to take into account. If a high percentage of the transmitted power is extracted (high values of *k*), the maximum range of the system would be reduced. In addition, it is important to avoid strong reflections so as to ensure a stable operation of the laser in a random regime. Hence, a stable laser operation is achieved by appropriately choosing the coupling percentages. In addition, every fiber end was submerged in refractive index matching gel so undesired reflections are avoided. These actions are of great importance since, as explained afterwards, the principle of operation of the system lies in the detection of reflection peaks.

Below are described the specific features of the sensors used in each of the networks. On the one hand, four groups of sensors complete the first sensor network, located at the kilometers 50, 100, 150, and 170 km, see Figure 5. 9 a). The coupling ratios used in this experiment were 1%, 5%, and 30% for the optical couplers located at the kilometer 50, 100, and 150 as displayed in Figure 5. 9 a). In order to demonstrate the TDM feature, the sensors are composed by four pairs of FBGs with the same Bragg wavelengths: λ_1 = 1545.6 nm, λ_2 = 1550 nm, λ_3 =1547 nm, and λ_4 = 1548.6 nm. It is also placed a single FBG which has a Bragg wavelength of λ_5 = 1545.1 nm. The reflectivity of the FBGs is higher than 90% and the full-width at half-maximum (FWHM) is 0.2 nm except for the tunable FBG used in λ_4 that is 0.3 nm.

On the other hand, the monitoring distance increases in the second experiment. In accordance, the coupling ratios chosen for the optical couplers located at the kilometers 50, 100, and 150 are 1%, 5%, and 10% respectively as depicted in Figure 5. 9 b). In this case, the FBGs present the following Bragg wavelengths: λ_1 = 1545.6 nm, λ_2 = 1550 nm, λ_3 = 1547 nm, λ_4 = 1548.6 nm, and λ5 = 1542.4 nm. The Bragg wavelengths of the two FBGs located at the end of the channel illustrated in Figure 5. 9 b) are λ_6 = 1541.2 nm and λ_7 = 1543.6 nm.

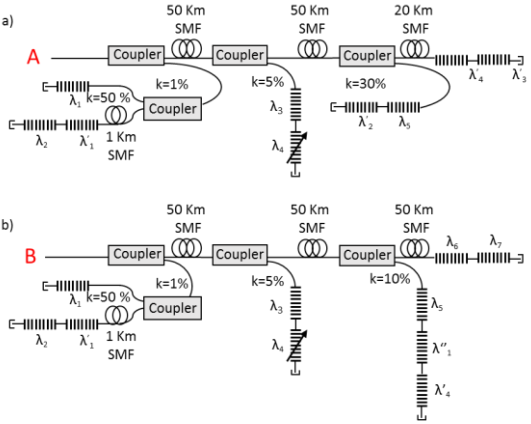

Figure 5. 9. Experimental setup of the sensor network to be monitored in the (a) first and (b) second experiment using hybrid WDM/TDM.

Principle of operation

The operating principle of this multiplexing system is based on the particular properties of RDFB-FL, such as their good performance when they are internally modulated [41] as well as their high peak power values [42]. In addition, the absence of longitudinal modes (Chapter II, section 2.2.3) allow obtaining stable output signals both in power and wavelength.

Initially, the laser is tuned in wavelength by the filter placed in the loop mirror and then it is modulated by the EOM before re-entering the distributed cavity. As a result, the power reflected along the fiber can be measured using an oscilloscope due to pulse modulation, acting as an optical reflectometer in the time domain. Therefore, we can obtain the voltage profile with respect to time for a certain wavelength. This same method can be used to determine the reflected power in a given wavelength range by sweeping the laser wavelength. If several FBGs are placed in the cavity, a reflection peak will be detected in the header when the central wavelength of the laser coincides with the Bragg wavelength of the grating. This is the principle of operation of the interrogating technique.

Since the reflected wavelengths of the FBGs vary with physical parameters (e.g., temperature or strain), the wavelength of the reflections will encode the information of the sensors. This implies that sensors can be wavelength

and time-multiplexed since for identical wavelength, sensors can be identified by their position along the fiber. Similarly, FBG sensors positioned at a close location (limited by the pulse duration) can be wavelength-multiplexed.

In summary, we can obtain a 3D map of our sensor network, with its three axes being wavelength, time/distance and detected voltage.

b. Experimental results

First, we confirmed that the generated laser was in the random regime for the entire wavelength range used in the experiment. The spectrum of the generated laser is shown in Figure 5. 10 a), using a pumping power of 1.4 W and a filter frequency of 1545 nm. In addition, the self-beating of the laser was detected by a photo-detector and measured in an electrical spectrum analyzer (ESA). As can be seen in Figure 5. 10 b), the detected signal does not present longitudinal modes for the whole wavelength range used in the experiments. This fact confirms that the laser continues to operate in the random regime, without noticing any influence on its performance caused by the gratings present in the cavity.

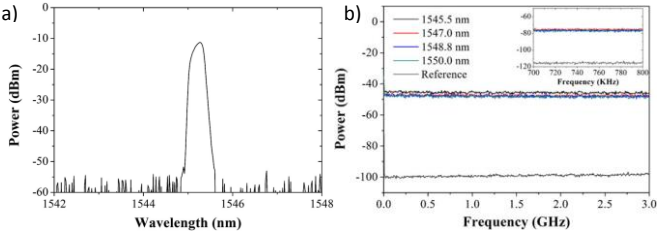

Figure 5. 10. a) Optical spectrum of the RDFB-FL (resolution= 0.01 nm) and b) self-beating signal of the emission line for different wavelengths. ESA resolution= 300 kHz (300 Hz Inset).

In the first experiment, measurements were carried out with a spatial resolution of 85 m and a wavelength step of 0.05 nm. In areas without sensors, larger steps were considered to reduce the measurement time. The results obtained after performing a complete wavelength sweep (from 1545 to 1550 nm) are shown in Figure 5. 11. The graphs confirm that it is possible to identify each sensor without ambiguity, both by its position and by its wavelength. The sensors presenting the same wavelength are identified by

their position and on the contrary, the sensors located at the same position can be wavelength-multiplexed. This circumstance is observed in the inset of Figure 5. 11 b), where two sensors centered on the same wavelength and separated by 1 km can be easily identified.

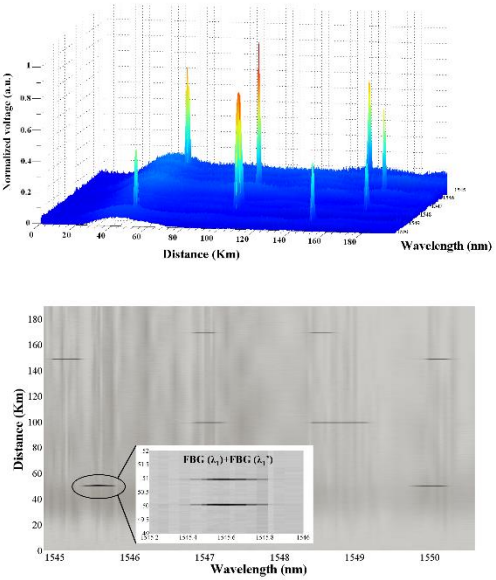

Figure 5. 11. Experimental results obtained for the 170 Km-setup.

Finally, the appropriate operation of the proposed scheme was validated performing strain measurements. An axial strain of 1000 με was applied to the FBG (λ'_3) located at 170 km. Figure 5. 12 shows the wavelength variation of FBG (λ_3) and FBG (λ'_3) located at kilometer 100 and 170, respectively, when the strain was applied to FBG (λ'_3). The graph verifies the proper behavior of the multiplexing network, without crosstalk between the sensors.

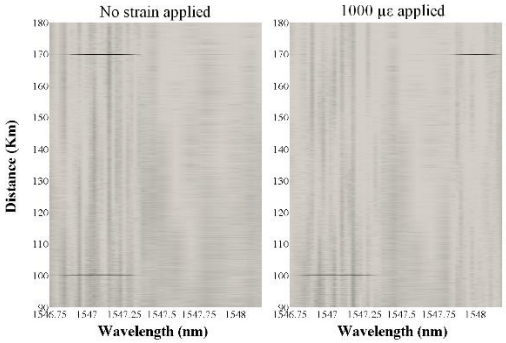

Figure 5. 12. FBG (λ_3) and FBG (λ'_3) wavelength response when 1000 με are applied to FBG (λ'_3).

As previously mentioned, in the second experiment we wanted to improve the multiplexing capacity of the network. For this, we have focused on three main objectives: increasing the maximum range of the network, its spatial resolution and its wavelength range. An independent study has been carried out in each case to determine the best configuration. To perform this task, it has been essential to use a programmable filter (Finisar 100S) replacing the tunable FBG used in the previous scheme. Thanks to this device, the comparative studies that are presented below have been carried out in a simple manner. Besides, these tests have undoubtedly improve the final performance of the initial sensor network.

To begin with, a study was performed varying the bandwidth of the programmable filter. The objective was to find the optimal bandwidth value that causes a higher reflection of the sensors so the maximum range of the network can be increased. Figure 5. 13 a) shows the results obtained for filter bandwidths between 0.22 and 0.40 nm. An increment of the reflected signal with the bandwidth is observed, being 0.38 nm the optimum value. As a result, a full width at half maximum (FWHM) of 0.38 nm was chosen for the filter, obtaining the optical spectrum presented in Figure 5. 13 b).

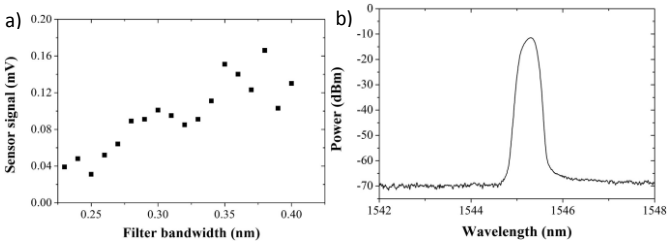

Figure 5. 13. a) Reflection given by a FBG for different filter bandwidth values and b) optical spectrum of the laser configuration used in the second experiment.

Later, an experimental study to improve the spatial resolution was developed. The pulse width of the interrogation signal determines the spatial resolution of the system, establishing a compromise between the spatial resolution and the system range. The narrower the width of the pulse is, the higher spatial resolution can be achieved. However, this causes a reduction in the amplitude of the reflected signal which limits the maximum distance that can be reached. For this reason, a narrower pulse width has been sought that does not reduce the amplitude of the reflected pulse. The results of the reflection detected for a FBG located at 50 km using different pulse width are displayed in Figure 5. 14. The reflected amplitude remains constant, except in the case of the narrowest pulse. This decrease and the pulse deformation is mainly caused by the bandwidth limit of the oscilloscope. Anyhow, these results verify that the spatial resolution can be improved from 85 m to 45 m, slightly reducing the amplitude of the signal detected. Therefore, a pulse width of 0.44 μs was generated in the second experiment.

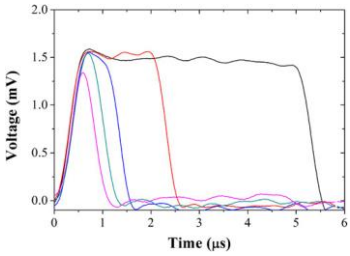

Figure 5. 14. Reflection given by a FBG for different pulse widths.

The last study deals with the extension of the wavelength range. The Raman gain presents a strong dependence with wavelength, causing an uneven amplification profile. To avoid this undesirable effect, which can destabilize the behavior of the laser, an automatic power equalization has been carried out using the programmable filter. By applying a previously determined attenuation profile, the laser is guaranteed to operate at constant power. The results obtained with and without the attenuation control are depicted in Figure 5. 15, showing a similar power detected for the whole wavelength range. The losses induced by this process were compensated by injecting a higher pump power (1.6 W). The power equalization allowed to increase the wavelength range of the network from 1540 to 1550 nm.

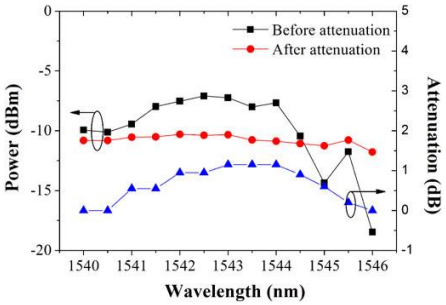

Figure 5. 15. Attenuation profile (blue line) and optical power detected before (black line) and after its application (red line).

Finally, the operation of the improved sensor network was tested, Figure 5. 9 b). The results obtained after measuring the FBGs located at 150 and 200 km are shown in Figure 5. 16 a) and b) respectively. The sensors can be identified even after improving the spatial resolution from 85 to 45 m, doubling the wavelength range and increasing the detection distance to 200 km.

In addition, the repeatability of the measures was verified by making nine consecutive sweeps. In Figure 5. 17, the measured results are displayed for a determined wavelength range centered at 1547 nm, showing a good repeatability of the measurements.

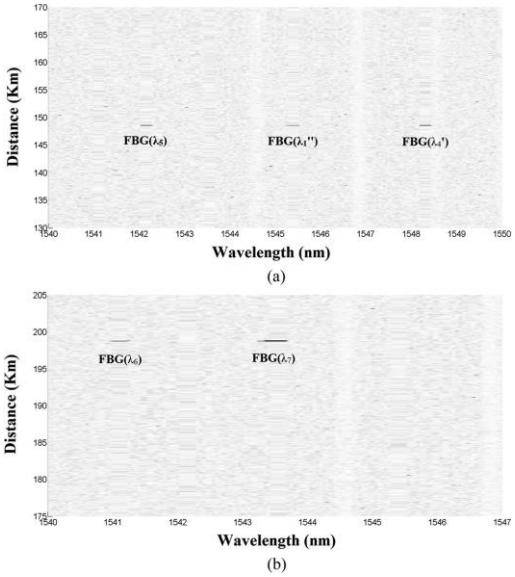

Figure 5. 16. Experimental results for the FBGs located at the kilometers 150 and 200.

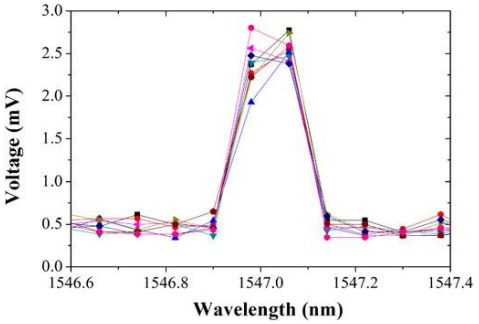

Figure 5. 17. Results obtained from ten consecutive sweeps to evaluate the repeatability of the measurements.

5.4. Remote (225 km) real-time interferometric sensor monitoring using FFT analysis

Despite their potential application in many fields, interferometric sensors, such as fiber loop mirrors (FLM), are not frequently employed in remote sensing structures due to their limited multiplexing capacity and high loss compared to FBGs. Several approaches have been previously presented for multiplexing interferometric sensors, such as coherence multiplexing [43] and phase carrier techniques [44]. In addition, some recent work has provided other solution to solve this problem by validating multiple multiplexing topologies based on the Fast Fourier Transform (FFT) analysis [45]-[47], initially proposed in [48].

In this work, the combination of the FFT technique and an RDFB-FL has been exploited to remotely interrogate a FLM at 225 km away from the central station. The axial strain applied to the interferometer has been monitored, obtaining a good linearity and a sensitivity of 1.69 πrad/mε.

a. Description of the system

The set-up developed for this experiment is shown in Figure 5. 18. It consists of a modified forward-pumped RDFB-FL combined with a commercial interrogator of FBGs (Smartec SM125). The principle of operation of the laser is the same as in previous schemes. Nevertheless, the main difference lies in the use of an additional element in the head mirror, the commercial interrogator, which acts as a seed for the generation of the distributed random laser.

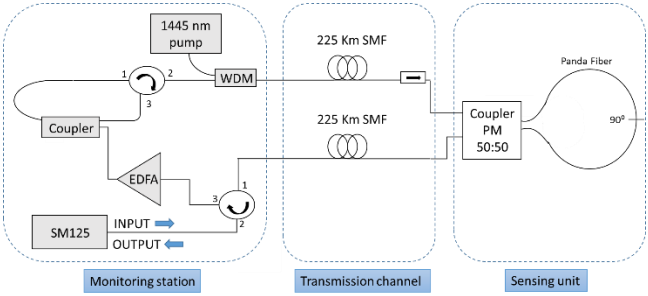

Figure 5. 18. Experimental set-up for interferometric sensor monitoring (EDFA: Erbium doped fiber amplifier; PM: Polarization maintaining).

This device performs a wavelength sweep in the 1510 to 1590 nm band every second and collects the signal reflected in the network. In this scheme, two channels of the device have been occupied: one to send the interrogating signal and another to receive the response of the sensor. The signal emitted by the SM125 enters through port 2 of a 3-port circulator and is amplified by an EDFA before injecting it into the laser cavity, using a 50:50 coupler. Amplification is required to equate the power generated in the laser cavity with that of the injected emission lines. By increasing the power of the latter, the random laser synchronizes with the interrogator, influencing the generation of the laser. An isolator is placed at the end of the 225 km distributed cavity to avoid the influence of the sensor on the performance of the laser.

The sensing unit consists of a high-birefringence (Hi-Bi) FLM. The use of this type of fibers allows detecting external physical changes, such as temperature or axial strain. These physical changes lead to a wavelength shift of the interference measured in the optical spectrum. In our sensor, two sections of Panda fiber have been fused together with a 90° rotation angle and connected to a polarization maintainer coupler. The 90° angle fusion between the sections of Panda fiber eliminates the requirement of a polarization controller, as it is demonstrated in [49].

Finally, the interference signal generated in the FLM is redirected to a 225 km way back fiber, collected by the port 1 of the circulator and then received at the Smartec device. As in previous schemes, we avoid the undesired amplified spontaneous emission noise generated in the laser cavity using a second path to send the signal back to the detector. The FFT of the received signal is calculated in Matlab every second, giving real-time information of the sensor system.

b. Experimental results

First, we verified the achievement of an RDFB fiber laser. For this purpose, the maximum power of the spectrum detected at the output of the system was measured, varying the injected pump power from 0.8 to 1.7 W. The resulting curve is shown in Figure 5. 19. As expected, there is an abrupt increase in the output power around 1.1 W corresponding to the laser threshold, validating the behavior of the system as a laser.

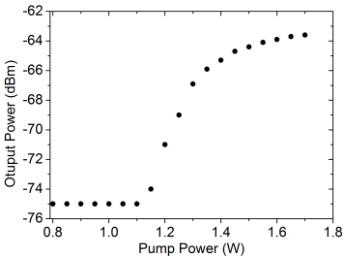

Figure 5. 19. Study of the output power vs pump power injected in the system.

Besides, some examples of the measured spectra for different pump powers are depicted in Figure 5. 20 a), as well as their corresponding FFT module in b). The interferometric signal of the sensor is properly measured for pumping values above 1.3 W. It is important to note that the detected spectrum does not fill the whole band scanned by the interrogator. We can only distinguish the lobes present in the band from 1530 to 1565 nm, which is the amplification band of the EDFA used in the header. A greater bandwidth of amplification would allow to obtain a higher resolution in the module of the FFT, thus improving the performance of the system.

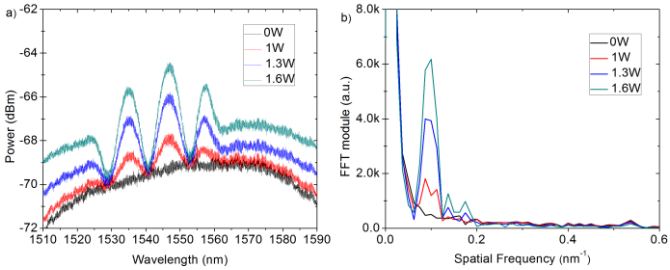

Figure 5. 20. Examples of the measured spectra varying the pump power and their corresponding FFT module.

In spite of this, the available bandwidth has allowed to correctly monitor the main frequency component of the sensor. As can be observed in Figure 5. 21, the FFTs corresponding to the interferometer measured independently and the signal obtained at the end of our scheme coincide. During the strain measuring process, the phase change of the component located at the spatial frequency 0.8 nm^{-1} has been monitored. The obtained results, see Figure 5.

22, show a clear linear fit with an R^2 like good as 0.9996 and a sensor sensitivity of 1.69 πrad/mε. As a conclusion, the proposed system has been validated to monitor in real time an interferometric sensor located 225 km away from the monitoring station.

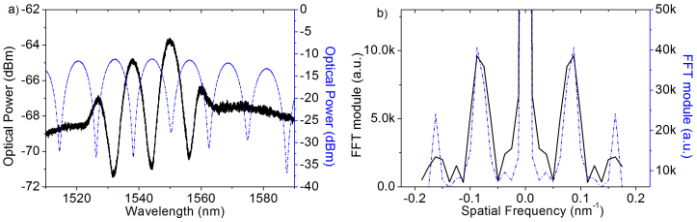

Figure 5. 21. Optical spectrum (a) and its FFT module (b) detected at the system's output (in black) and measured independently (in blue).

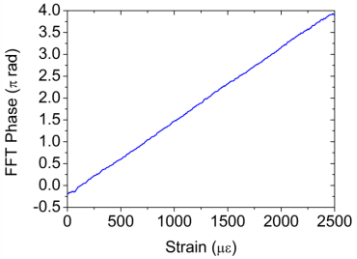

Figure 5. 22. FFT phase behavior of the sensor vs strain applied.

5.5. Remote (290 km) displacement sensor monitoring and coherence multiplexing at 270 km

Among all the multiplexing approaches, coherence multiplexing uses light sources with low coherence length in interferometric configurations to multiplex several sensors into a single optical signal [50]. CDM avoids the relatively complex requirements of time [51] or wavelength-division multiplexing [52], such as synchronization and frequency ramping of the optical source, respectively. However, it requires that the geometry of the sensor must be carefully designed so that the optical path differences (OPD) of each sensing interferometer are in different ranges. Then every sensing signal can be de-multiplexed by selecting its OPD in the local receiving interferometer. Systems that apply CDM have been widely used in fiber optic sensing, multiplexing up to 10 sensors in [53] and measuring physical parameters such as temperature, displacement and strain [54]-[56].

Commonly, CDM is employed in sensor systems based on fiber optic low-coherence interferometry (FOLCI) [57][58]. Temperature [59], pressure [60], strain [61] and refractive index [62] are some of the parameters that can be measured with high accuracy using this approach. Although the FOLCI technique is intensity-based, the measurement accuracy is ideally insensitive to fluctuations in optical power between the monitoring station and the location of the sensor. Consequently, higher resolutions are provided when compared to conventional intensity-based sensors. Moreover, FOLCI systems allow the measurement of absolute displacements without the requirement of a prior characterization of the sensors. Due to the intrinsic need for short-coherence length in FOLCI, broadband light sources are generally employed. However, their low output power (compared to laser sources) makes systems based on low coherence generally not suitable for long-range applications.

In the present study, we demonstrate that the natural coherence length of RDFB-FLs can be used in low-coherence interferometry and coherence-multiplexing schemes, since it is short enough to be suitable for FOLCI. Besides, the remote interrogation of an interferometric sensor has been achieved 290 km away from the header. This is, as far as we are aware, the longest distance for a remote fiber optic sensing system.

a. Description of the system

Two experiments have been carried out to show the potential of this technique in conjunction with an RDFB-FL. Accordingly, two different

schemes have been developed for this purpose, both formed by three differentiated parts: the laser source, the transmission channel and the sensing unit (see Figure 5. 23 and Figure 5. 24).

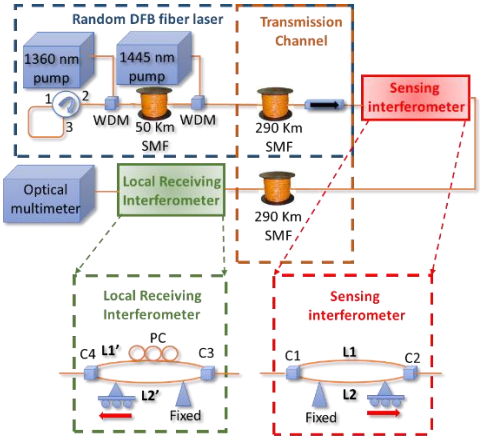

Figure 5. 23. Set-up 1.Schematic FOLCI set-up with one sensor.

The light source used to interrogate the sensor unit is the same in both cases. A previous study, presented in Chapter IV Section 4.3, determined the optimal laser configuration which maximizes the system's performance. Then, the laser header is formed by two pump lasers (1360 and 1445nm), separated by 50 km of SMF, which inject 3W each into the cavity of a single-arm forward-pumped RDFB-FL.

The transmission channel consists of two identical optical paths of 290 km in the first and 270 km in the second experiment. The first path is part of the distributed cavity of the laser, which illuminates the sensor unit. The second path guides the signal modulated by the sensor unit back to the detection system. The counter-propagating noise in the arm of the laser is higher than the sensor response. For this reason, both the illuminating signal and the response of the sensors cannot share the same transmission channel.

In the first scheme, Figure 5. 23, two Mach Zehnder interferometers (MZI) compose the FOLCI sensing scheme: a sensing interferometer (SI) located 290 km away from the monitoring station and a local receiving interferometer (LRI). Two 50:50 optical couplers (C1, C2 and C3, C4) connected by two SMF

arms (L1, L2 and L1', L2') compose each interferometer, respectively. The lengths of each arm in the SI and LRI are: L1≈L1'=2.16 m, L2=9.04 m and L2'=9.03 m. Two separate displacement stages, equally formed by a fixed platform and a mobile micro-positioner (Newport M423), apply displacement in L2 and L2' arms. The detected interference depends on the polarization of the two interfering signals that arrive at the LRI. Therefore, a polarization controller is connected in the LRI arm L1' so the fringe visibility of the interference signal is maximized. Finally, the optical power reaching the monitoring station is measured by an optical multimeter (ANDO AQ-2140) connected at the output of the LRI.

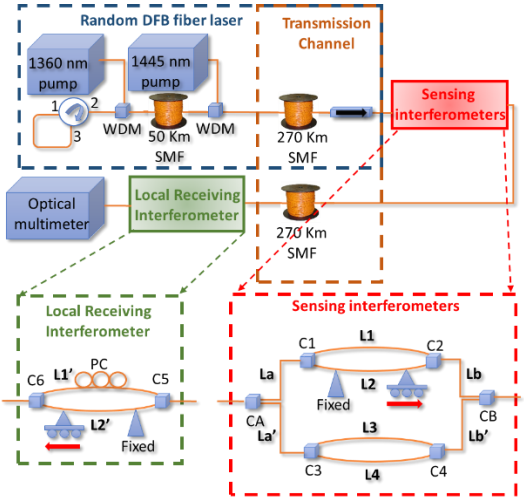

Figure 5. 24. Set-up 2. Schematic FOLCI set-up with two sensors.

To evaluate the capability of the system to achieve coherence multiplexing, a second setup is proposed (see Figure 5. 24). This one is composed by three MZI: two coherence multiplexed sensing interferometers (SI1 and SI2) located 270 km away from the monitoring station and a LRI. The SIs are arrayed in parallel between the input and output buses by two optical couplers 50:50, CA and CB, following an intrinsic-reference ladder configuration [50]. The arms of CA and CB present a length of La≈ La'≈ Lb≈ Lb'= 1.08 m. The detection of the sensors is done by the LRI connected in series, which interrogates both SIs in a single displacement sweep. SI1 and the LRI are the same as in set-up 1. The second SI (SI2) is formed by two 50:50 optical couplers (C5 and C6)

connected by two SMF arms (L3 and L4), with a length of 2.16 m and 9.05 m, respectively. As before, a polarization controller is used in the LRI arm L1' to maximize the fringe visibility of the interference signal detected.

Due to the larger number of couplers employed in this second test and the losses induced by them, the interrogation distance of the sensors was reduced to 270 km. However, power losses can be modest if the coupling ratios of the couplers used are properly chosen, even if several sensors are multiplexed [63].

Principle of operation

A FOLCI system requires at least two illuminated interferometers sharing optical paths. The OPDs of both interferometers must differ a length several times larger than the coherence length of the light source (*Lc*). Providing this, no coherent interference will be generated by each interferometer individually. Let us consider that we are using MZ interferometers. If the difference between the OPDs of the SI (OPD1=|L1-L2|) and the LRI (OPDr=|L1'-L2'|) is tailored to be shorter than *Lc*, |OPDr-OPD1|< *Lc*, interference will result. Then, the optical intensity detected at the output of the LRI (*I*) will be given by:

$$\boldsymbol{I(\Delta L) = I_0\left(1+\sqrt{K_1K_2K_3K_4}\,exp\left(-\frac{2\Delta L}{L_c}\right)^2 cos(k\Delta L)\right)} \qquad (1)$$

where ΔL=OPDr-OPD1, k is the wavenumber, I_0 the total optical power arriving at the detector and K_1, K_2, K_3 and K_4 are the power split ratios of the couplers used in the SI and the LRI respectively [58].

In FOLCI structures, low-coherence broadband sources such as light-emitting diodes (LED) are widely employed. As their spectral width varies from 30 to 60 nm, they offer short coherence lengths (compared to laser sources) and narrower interferograms are obtained. In our experiments, a RDFB-FL serves as the broadband source needed for a FOLCI system. Although the inherent line-width of RDFB-FL is much narrower than the spectral width of LED sources (several nanometers), it is considerably wider than in traditional laser sources. It also presents a high output power (hundreds of milliwatts) which combined with a coherence length under the millimeter (see Chapter II, section 2.2.3) make RDFB-FLs perfect candidates to allow the use of FOLCI in long-range schemes.

Figure 5. 25 a) shows an example of the normalized interferogram measured at the output of the FOLCI system for a single sensor. In order to verify the experimental results, simulations have been performed and presented in Figure 5. 25 b), showing a good agreement. The simulated interferogram has been obtained through equation (1), calculating the values of I for ΔL from -1.2 mm to 1.2 mm, considering a coherence length of 0.808 mm, k=2π/1550 nm and K_1=K_2=K_3=K_4= 0.5.

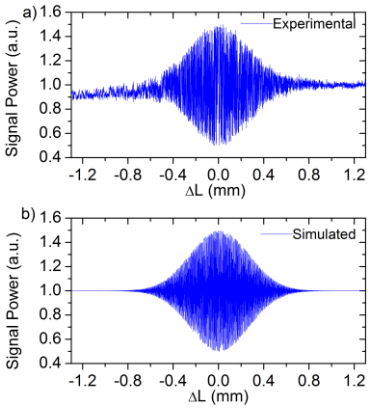

Figure 5. 25. Normalized a) experimental and b) simulated traces detected at the output of the FOLCI scheme.

According to the theory, both traces present a Gaussian profile with a total width ≈ 2Lc. If any variation is caused in the OPD of the SI (OPD1), the value of ΔL will be modified. As a result, the fringe visibility and the phase of the signal detected at the output of the FOLCI system I will be shifted, altering the position of the central fringe. Absolute changes in OPD1 can be determined by measuring the displacement of the central fringe. To interrogate the sensors, the OPD in the local receiving interferometer (OPDr) is modified using a translation stage and a displacement sweep. In this manner, the power received at the power-meter is detected every step to reconstruct the interferogram. Consequently, the position of the central fringe (i.e. OPD1) can be inferred for every complete sweep.

To avoid signal overlapping when interrogating more than one SI, the OPD of each MZ sensing interferometer must differ by at least two times the coherence length of the source, OPD1-OPD2 >2Lc. Increasing the difference

between the OPDs of each SI reduces crosstalk in the detected signal. Moreover, it enlarges the displacement range that can be measured without overlapping.

b. Experimental results

The aim of the first experiment was to evaluate the feasibility of monitoring an optical fiber interferometer at 290 km as a displacement sensor. In a second test, a set of measurements have been performed to validate the proposed system as a coherence multiplexing scheme, interrogating two MZI at 270 km.

First, the optical spectra measured after 290 and 270 km (between the optical isolator and C1) are represented in Figure 5. 26 a) and b), showing a central wavelength set at 1555 nm and a peak power of -30.18 dBm and -25.21 dBm, respectively.

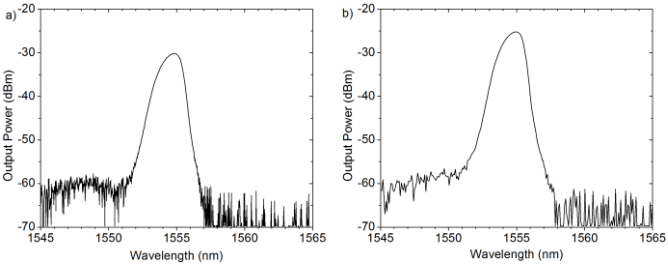

Figure 5. 26. a) Optical spectrum of the random DFB fiber laser measured after 290 km and b) 270 km.

The development of both experiments was similar, although some parameters were modified. Length variations have been induced and tracked in OPD1. In the experiment with two sensing interferometers, the OPD in the SI2 was not modified during the experiment to prove the absence of crosstalk between them. The arm L2 of the SI (SI1 in the second test) has been fixed to a micro-positioner, with a resolution of 10 µm, to apply a displacement from 0 to 1 mm with 0.1 mm steps. Equivalently, the arm L2' in the LRI was attached to a separate micro-positioner, with a resolution of 20 nm, to perform the interrogation. In this manner, a displacement sweep was performed for 2.5 mm (10mm) every 3.4 µm (8.5 µm). After each complete sweep, it has been

determined the central fringe position of the detected interferogram which represents the displacement of the SI (SI1 and also SI2).

The evolution of the interferograms detected in both experiments are presented in Figure 5. 27 a) and Figure 5. 28 a), respectively. In the first case, the measured signals for 0, 4 and 8 mm displacements are displayed, showing a clear shift of the central fringe. In order to ease the process of locating the central fringe, simple post-processing was applied by calculating the moving average of the absolute value of the data (Figure 5. 27 b)). From the previous figures it can be inferred that the displacement of the central fringe position is clearly discernible and measurable.

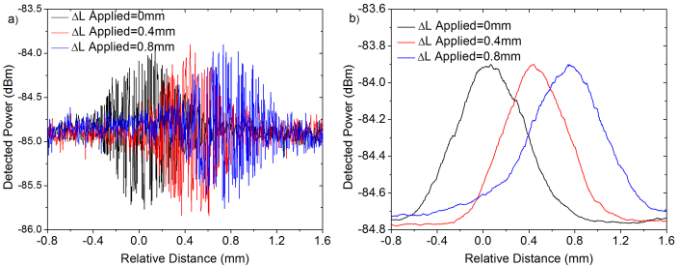

Figure 5. 27. a) Experimental traces detected at the output of the FOLCI set-up 1 for three different sensor states and b) after post-processing.

In the same manner, Figure 5. 28 a) shows the observed signals at the LRI output for 0 mm and 2 mm displacements. The same detected signals are presented in Figure 5. 28 b) after applying post-processing (as in Figure 5. 27 b)). It can be seen in the figures that the displacement of the central fringe position of both SI1 and SI2 can be evidently determined.

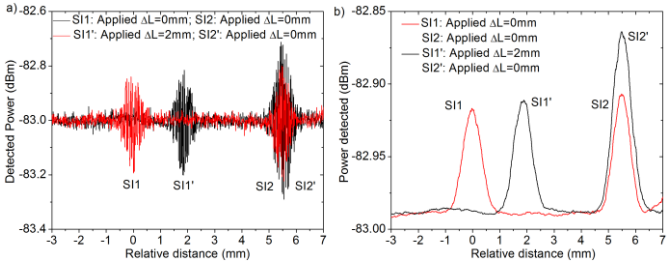

Figure 5. 28. a) Experimental traces detected at the output of the FOLCI set-up 2 for two different sensor states and b) after post-processing.

It is also evidenced the lack of cross-talk since the interferogram of SI2 remains in a fixed position in all the displacement sweeps while SI1 shifts as we modify its OPD. It should be noted that the total displacement range is limited by the difference between the OPDs of the sensing interferometers. In this experiment, the band-gap between the OPDs of the sensors is 4 mm. As a result, the displacement range that can be measured without overlapping is 4 mm. However, if the OPD difference between sensing interferometers is adjusted, the displacement range can be increased depending on the application and its requirements.

Another aspect to be considered, common in every FOLCI system, is the total interrogation range, which is limited by the maximum displacement generated in the OPD of the receiving interferometer. In this experiment, simple elongation has been applied for the verification, but other solutions allow a wider range, such as the based on moving mirrors [53].

In our system, MZ interferometers with considerably long arms are used. In this manner, the strain applied on the fiber during its elongation is reduced and a larger displacement can be induced without breaking the fiber. However, the polarization fading can be an annoying issue for large cavity interferometers, especially for MZI. As a result, the amplitude of the detected interferograms depends also on the instantaneous polarization state of the signals interfering. A variation in the range of both SI2 and SI2' interferograms is appreciated due to these polarization changes. In order to manage and reduce this effect, polarization has been controlled by means of a polarization controller in the LRI. In each displacement sweep performed, the polarization state has been set at the beginning of each measurement to maximize the fringe visibility of the signal. However, this issue could be addressed by

including some polarization selective devices in the receiving interferometer, such as a polarization scrambler.

Finally, the relative distance measurements that correspond to the peak of each trace are displayed in Figure 5. 29 a) and b). In these graphs, the displacement applied to the sensor versus the displacement measured shows a linear tendency with a slope of 1.03 (1.04), R^2=0.99 (0.98) and a resolution of 0.02mm. Some deviations in the experimental data are observed from the desired unity slope line. The intrinsic error of the micro-positioners and vibrations during the measuring process might be the cause.

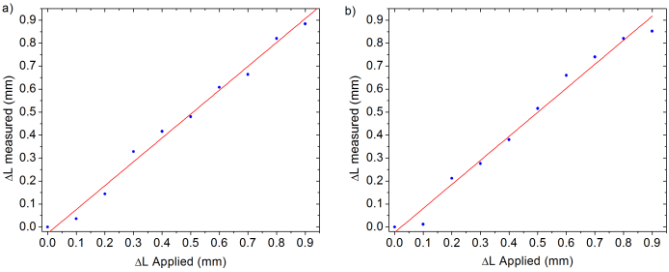

Figure 5. 29. a) Experimental displacement measurements obtained using set-up 1 and b) set-up 2.

In order to provide a more complete study of the system, an estimation of the sensors that can be multiplexed vs. distance was carried out. This estimation was made according to the worst case scenario, taking into account the power losses measured experimentally. From the experimental results, we have determined that a single sensor can be monitored at 290 km. In the estimation we have considered that only one LRI is employed to interrogate all the sensors. As a consequence, the loss induced by this interferometer is the same in every case. As more SIs are added to the FOLCI system, the number of couplers (supposing 2x2 couplers for simplicity) increases. Each time the number of SIs double, the losses induced by the couplers increase in 3dB. In addition, each 50:50 coupler present a maximum of 0.6 dB of measured insertion losses. Providing the gain in the cavity is negligible at distances over 200 km, the monitoring distance is reduced as losses increase. A simple scheme, see Figure 5. 30, is presented to explain these concepts:

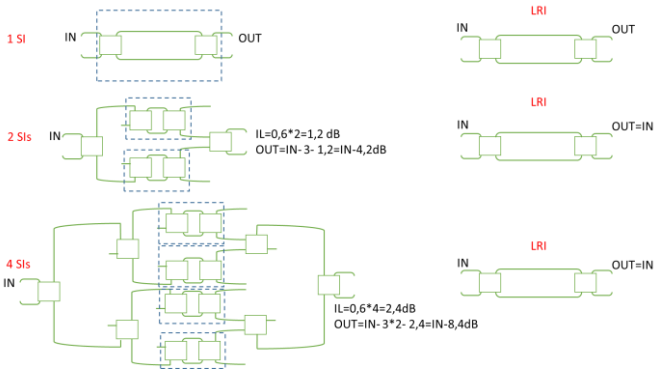

Figure 5. 30. Scheme for the progressive calculation of losses of the SIs and the LRI.

Considering the losses introduced by the SIs and providing that the fiber presents an attenuation of 0.2dB/km, the following table has been calculated:

Maximum number of SIs (2^n)	Number of 2x2 couplers (2^{n+2}-2)	Estimated loss increase (dB) (-3n-0.6x2n)	Maximum monitoring distance (km)
1	**2**	0	290
2	6	-4,2	279,5
4	14	-8,4	269
8	30	-12,6	258,5
16	62	-16,8	248

From the previous table, we have inferred the formula that calculates the maximum interrogation distance based on the maximum number of SIs and the achieved maximum length:

$$Max\ distance = 290 - \frac{1}{2}\left(\frac{3n - 0.6 \cdot 2n}{0.2}\right)$$

However, it should be noted that these calculations take only into consideration power constrains. However, other aspects for coherence multiplexing should be considered in a real situation, such as OPD selection to avoid crosstalk, etc. [50]

5.6. Conclusions

The main motivation of this chapter has been to demonstrate through a variety of experiments the great potential of RDFB-FL lasers for the interrogation of sensor networks. Most of the attention has been focused on increasing the interrogation distance as well as the multiplexing capacity.

In particular, section 5.2 focuses on experimental validation of a switchable and reconfigurable MWFL in real-time based on a RDFB-FL. Two sensor networks were simultaneously monitored at 50 km using a remote powered-by-light fiber optic switch. From the experiments, we can draw some conclusions as following:

- The presented technique allows to interrogate as many sensor networks as outputs has the optical switch, which expands the multiplexing capacity of the network. Two sensor networks have been monitored simultaneously: one composed of 11 gratings and another composed of 7 interferometric sensors. The spectral versatility of the RDFB-FL makes possible the interrogation of both networks by implementing WDM.
- The developed scheme is also power efficient, since it uses the excess Raman pump to power the RFOSw. In addition, the control signal is generated by the MWFL together with the sensor monitoring signal, avoiding the need of an additional control device.
- The inclusion of an additional method of amplification in the header of the laser improves its general operation. The EDFA has allowed to expand the usable wavelength range as well as an easier equalization of the interrogation channels.

Section 5.3 is dedicated to a network of sensors which implements hybrid WDM/TDM and offers a promising solution to improve the limited multiplexing capacity of the ultra-long range remote sensing systems.

- The modulation of the laser cavity offers a new range of possibilities and allows to identify the sensors using time-domain reflectometry. The ability to internally modulate an RDFB-FL without frequency restrictions [41] has permitted to implement a quasi-distributed interrogation scheme.
- The performed experiments verify that not only WDM can be implemented, but also TDM can also be applied, exploiting the advantages offered by both multiplexing techniques used jointly.
- From an initial proof of concept scheme, several studies have been carried out to optimize the general features of the system. Spatial resolution, maximum distance and wavelength range have been increased. The repeatability and general good performance of the system has been validated for a maximum of 10 sensors and a 200 km range. However,

more advanced reflectometry techniques and equipment could improve the performance of the system.
- The use of a programmable filter to filter the signal into the cavity instead of a tunable FBG has demonstrated to be an advantageous tool, since it improves the general features of the system and its versatility.

Following with Section 5.4, a new sensing application of RDFB-FL is presented and demonstrated. It implements a real-time FFT analysis to monitor an interferometric sensor located at a distance of 225 km.

- The proposed scheme demonstrates that not only gratings are suitable for long distance sensor networks. In addition, it offers a solution to the main problems of interferometric sensors, such as their low multiplexing capability and high losses. By combining the RDFB-FL with the commercial FBGs interrogator, interferometric sensors can be multiplexed and monitored using FFT analysis.
- Different physical parameters could be measured using other types of interferometric sensors, such as MZ interferometers, and Hi-Bi fibers, depending on the requirements of the application.
- The performance of the system could be improved by modifying the additional amplifier device in the header of the RDFB-FL. A larger amplification bandwidth and a higher gain will allow to increase the resolution of the measurements and the distance to the sensor unit.

The last section considers a double-pumped RDFB-FL as the light source for a fiber optic low-coherence interferometry scheme. As far as the author are aware, it is the first time that this type of lasers has been used in FOLCI schemes. In addition, the ability of the system to achieve coherence multiplexing has been proved. This can be attained due to the particular properties of RDFB-FL, such as its high power and relatively short coherence length.

- The experimental results provided in this section show the great potential of FOLCI schemes in remote sensing applications when using RDFB-FL as the light source.
- The study presented in Chapter IV section 4.3 has served to optimize the performance of this light source. This has been exploited for a particular sensing application, establishing a new milestone of interrogation distance in fiber optic networks.
- The experiments performed serve as a proof of concept, but the accuracy of the measurements could be enhanced by modifying the receiving interferometer setup (improve noise isolation or polarization control) and improving the accuracy of the mechanical sweep applied to both sensors, without crosstalk.

- In several of the proposed schemes it is necessary to double the fiber in the system to avoid the counter propagating noise. However, a cable of two fibers can be used instead of a single-fiber cable so it does not present a significant increment in the final costs of the installation.

As a final conclusion, the experiments developed in this chapter verify the great versatility that RDFB-FLs offer for their use in remote monitoring applications. As it has been previously stated, there is no ideal solution for all remote sensing scenarios. However, the outstanding features of RDFB-FL allow their adaptation to a great variety of applications. In fact, RDFB-FL have demonstrated their capability to interrogate sensors of different nature (FLM, MZ interferometers and FBGs), to implement several multiplexing techniques (WDM, TDM and CDM) as well as combinations thereof, all at distances of hundreds of kilometers.

These results have originated the publications in references [34]-[37].

5.7. References

[1] López-Higuera, J. M., Cobo, L. R., Incera, A. Q., & Cobo, A. (2011). Fiber optic sensors in structural health monitoring. Journal of lightwave technology, 29(4), 587-608.

[2] Li, H. N., Li, D. S., & Song, G. B. (2004). Recent applications of fiber optic sensors to health monitoring in civil engineering. Engineering structures, 26(11), 1647-1657.

[3] Guo, H., Xiao, G., Mrad, N., & Yao, J. (2011). Fiber optic sensors for structural health monitoring of air platforms. Sensors, 11(4), 3687-3705.

[4] Glisic, B., & Inaudi, D. (2008). Fibre optic methods for structural health monitoring. John Wiley & Sons.

[5] Ko, J. M., & Ni, Y. Q. (2005). Technology developments in structural health monitoring of large-scale bridges. Engineering structures, 27(12), 1715-1725.

[6] Chang, P. C., Flatau, A., & Liu, S. C. (2003). Health monitoring of civil infrastructure. Structural health monitoring, 2(3), 257-267.

[7] DING, Y., SHI, B., & SUI, H. B. (2005). Tunnel structural health monitoring system and fiber optic sensing technology. Journal of Disaster Pnevention and Mitigation Engineering, 4, 004.

[8] Wong, K. Y. (2004). Instrumentation and health monitoring of cable-supported bridges. Structural control and health monitoring, 11(2), 91-124.

[9] Prasad, A. G., Asokan, S., & Tatavarti, R. (2009, October). Detection of tsunami wave generation and propagation using fiber bragg grating sensors. In Sensors, 2009 IEEE (pp. 1278-1281). IEEE.

[10] Nakstad, H., & Kringlebotn, J. T. (2008, May). Realisation of a full-scale fibre optic ocean bottom seismic system. In 19th International Conference on Optical Fibre Sensors (Vol. 7004, p. 700436). International Society for Optics and Photonics.

[11] Tam, H. Y., Lee, T., Ho, S. L., Haber, T., Graver, T., Méndez, A., ... & Tin, S. (2007). Utilization of fiber optic Bragg Grating sensing systems for health monitoring in railway applications. Struct. Health Monitoring, Quantification, Validation, Implementation, 1, 2.

[12] Filograno, M. L., Guillén, P. C., Rodríguez-Barrios, A., Martín-López, S., Rodríguez-Plaza, M., Andrés-Alguacil, Á., & González-Herráez, M. (2012). Real-time monitoring of railway traffic using fiber Bragg grating sensors. IEEE Sensors Journal, 12(1), 85-92.

[13] Ferraro, P., & De Natale, G. (2002). On the possible use of optical fiber Bragg gratings as strain sensors for geodynamical monitoring. Optics and Lasers in Engineering, 37(2-3), 115-130.

[14] Moore, J. R., Gischig, V., Button, E., & Loew, S. (2010). Rockslide deformation monitoring with fiber optic strain sensors. Natural Hazards & Earth System Sciences, 10(2).

[15] Vallejo, M. F., Perez-Herrera, R. A., Elosua, C., Diaz, S., Urquhart, P., Bariain, C., & Lopez-Amo, M. (2009). Resilient amplified double-ring optical networks to multiplex optical fiber sensors. Journal of Lightwave Technology, 27(10), 1301-1306.

[16] Fernandez-Vallejo, M., Díaz, S., Perez-Herrera, R. A., Passaro, D., Selleri, S., Quintela, M. A., Lopez Higuera, J.M., & Lopez-Amo, M. (2010). Resilient long-distance sensor system using a multiwavelength Raman laser. Measurement Science and Technology, 21(9), 094017.
[17] Perez-Herrera, R. A., Fernandez-Vallejo, M., & Lopez-Amo, M. (2012). Robust fiber-optic sensor networks. Photonic sensors, 2(4), 366-380.
[18] Zhang, H., Wang, S., Gong, Y., Liu, T., Xu, T., Jia, D., & Zhang, Y. (2013). A quantitative robustness evaluation model for optical fiber sensor networks. Journal of Lightwave Technology, 31(8), 1240-1246.
[19] Jackson, D. A., Ribeiro, A. L., Reekie, L., & Archambault, J. L. (1993). Simple multiplexing scheme for a fiber-optic grating sensor network. Optics Letters, 18(14), 1192-1194.
[20] Brooks, J., Wentworth, R., Youngquist, R., Tur, M., Kim, B., & Shaw, H. (1985). Coherence multiplexing of fiber-optic interferometric sensors. Journal of Lightwave Technology, 3(5), 1062-1072.
[21] Nelson, A. R., McMahon, D. H., & Gravel, R. L. (1980). Passive multiplexing system for fiber-optic sensors. Applied optics, 19(17), 2917-2920.
[22] Morey, W. W., Dunphy, J. R., & Meltz, G. (1991). Multiplexing fiber Bragg grating sensors. Fiber & Integrated Optics, 10(4), 351-360.
[23] Cranch, G. A., & Nash, P. J. (2001). Large-scale multiplexing of interferometric fiber-optic sensors using TDM and DWDM. Journal of lightwave technology, 19(5), 687-699.
[24] Montoya, V., López-Amo, M., & Abad, S. (2000). Improved double-fiber-bus with distributed optical amplification for wavelength-division multiplexing of photonic sensors. IEEE Photonics Technology Letters, 12(9), 1270-1272.
[25] Diaz, S., Cerrolaza, B., Lasheras, G., & Lopez-Amo, M. (2007). Double Raman amplified bus networks for wavelength-division multiplexing of fiber-optic sensors. Journal of lightwave technology, 25(3), 733-739.
[26] Digonnet, M. J., Vakoc, B. J., Hodgson, C. W., & Kino, G. S. (2004, June). Acoustic fiber sensor arrays. In Second European Workshop on Optical Fibre Sensors (Vol. 5502, pp. 39-51). International Society for Optics and Photonics.
[27] Fernandez-Vallejo, M., & Lopez-Amo, M. (2012). Optical fiber networks for remote fiber optic sensors. Sensors, 12(4), 3929-3951.
[28] Perez-Herrera, R. A., & Lopez-Amo, M. (2013). Fiber optic sensor networks. Optical Fiber Technology, 19(6), 689-699.
[29] Culshaw, B. (1991, August). Fiber optic sensor networks. In Fiber Optic Sensors: Engineering and Applications (Vol. 1511, pp. 168-179). International Society for Optics and Photonics.
[30] Sun, Q., Li, X., Zhang, M., Liu, Q., Liu, H., & Liu, D. (2013, December). High capacity fiber optic sensor networks using hybrid multiplexing techniques and their applications. In 2013 International Conference on Optical Instruments and Technology: Optical Sensors and Applications (Vol. 9044, p. 90440L). International Society for Optics and Photonics.
[31] Martins, H., Marques, M. B., & Frazão, O. (2011). 300 km-ultralong Raman fiber lasers using a distributed mirror for sensing applications. Optics express, 19(19), 18149-18154.

[32] Wang, Z. N., Rao, Y. J., Wu, H., Li, P. Y., Jiang, Y., Jia, X. H., & Zhang, W. L. (2012). Long-distance fiber-optic point-sensing systems based on random fiber lasers. Optics express, 20(16), 17695-17700.
[33] Fernandez-Vallejo, M., Bravo, M., & Lopez-Amo, M. (2013). Ultra-long laser systems for remote fiber Bragg gratings arrays interrogation. IEEE Photonics Technology Letters, 25(14), 1362-1364.
[34] Bravo, M., de Miguel Soto, V., Ortigosa, A., & Lopez-Amo, M. (2015). Fully Switchable Multi-Wavelength Fiber Lasers Based on Random Distributed Feedback for Sensors Interrogation. Journal of Lightwave Technology, 33(12), 2598-2604.
[35] Leandro, D., deMiguel Soto, V., Perez-Herrera, R. A., Acha, M. B., & López-Amo, M. (2016). Random DFB fiber laser for remote (200 km) sensor monitoring using hybrid WDM/TDM. Journal of Lightwave Technology, 34(19), 4430-4436.
[36] DeMiguel-Soto, V., Lopez-Aldaba, A., Leandro, D., & Lopez-Amo, M. (2016, October). Ultra-Long random laser for remote real-time interferometric sensor monitoring using FFT analysis. In Asia-Pacific Optical Sensors Conference (pp. Tu3A-4). Optical Society of America.
[37] DeMiguel-Soto, V., Leandro, D., & Lopez-Amo, M. (2018). Ultra-long (290 km) remote interrogation sensor network based on a random distributed feedback fiber laser. Optics Express, 26(21), 27189-27200.
[38] Bravo, M., Baptista, J. M., Santos, J. L., Lopez-Amo, M., & Frazão, O. (2011). Ultralong 250 km remote sensor system based on a fiber loop mirror interrogated by an optical time-domain reflectometer. Optics letters, 36(20), 4059-4061.
[39] Bravo, M., Erro, M. A., Algueta, J. M., Diaz, S., & Lopez-Amo, M. (2013). Remote fiber optic switch powered by light for robust interrogation of fiber Bragg grating sensor networks. Measurement Science and Technology, 24(9), 094021.
[40] Zhang, M., Sun, Q., Wang, Z., Li, X., Liu, H., & Liu, D. (2012). A large capacity sensing network with identical weak fiber Bragg gratings multiplexing. Optics Communications, 285(13-14), 3082-3087.
[41] Bravo, M., Fernandez-Vallejo, M., & Lopez-Amo, M. (2013). Internal modulation of a random fiber laser. Optics letters, 38(9), 1542-1544.
[42] Churkin, D. V., El-Taher, A. E., Vatnik, I. D., Ania-Castañón, J. D., Harper, P., Podivilov, E. V., ... & Turitsyn, S. K. (2012). Experimental and theoretical study of longitudinal power distribution in a random DFB fiber laser. Optics express, 20(10), 11178-11188.
[43] Brooks, J., Wentworth, R., Youngquist, R., Tur, M., Kim, B., & Shaw, H. (1985). Coherence multiplexing of fiber-optic interferometric sensors. Journal of Lightwave Technology, 3(5), 1062-1072.
[44] Dandridge, A., Tveten, A., Kersey, A., & Yurek, A. (1987). Multiplexing of interferometric sensors using phase carrier techniques. Journal of Lightwave Technology, 5(7), 947-952.
[45] Barrera, D., Villatoro, J., Finazzi, V. P., Cárdenas-Sevilla, G. A., Minkovich, V. P., Sales, S., & Pruneri, V. (2010). Low-loss photonic

crystal fiber interferometers for sensor networks. Journal of lightwave technology, 28(24), 3542-3547.
[46] Leandro, D., Bravo, M., Ortigosa, A., & Lopez-Amo, M. (2015). Real-time FFT analysis for interferometric sensors multiplexing. Journal of Lightwave Technology, 33(2), 354-360.
[47] Leandro, D., Lopez-Aldaba, A., Bravo, M., & Lopez-Amo, M. (2016). Monitoring multiple Hi-Bi sensing fibers in a single fiber loop mirror. Journal of Lightwave Technology, 34(19), 4543-4549.
[48] Hu, Y., & Chen, S. (1995). Spatial frequency multiplexing of optical fiber sensor arrays. Optics letters, 20(10), 1207-1209.
[49] Leandro, D., Bravo, M., & Lopez-Amo, M. (2015). High resolution polarization-independent high-birefringence fiber loop mirror sensor. Optics express, 23(24), 30985-30990.
[50] Brooks, J., Wentworth, R., Youngquist, R., Tur, M., Kim, B., & Shaw, H. (1985). Coherence multiplexing of fiber-optic interferometric sensors. *Journal of Lightwave Technology*, *3*(5), 1062-1072.
[51] Spirit, D. M., Ellis, A. D., & Barnsley, P. E. (1994). Optical time division multiplexing: Systems and networks. *IEEE Communications Magazine*, *32*(12), 56-62.
[52] Mukherjee, B. (2000). WDM optical communication networks: progress and challenges. *IEEE Journal on Selected Areas in communications*, *18*(10), 1810-1824.
[53] Inaudi, D., Vurpillot, S., & LLoret, S. (1996, May). In-line coherence multiplexing of displacement sensors: a fiber optic extensometer. In Smart Structures and Materials 1996: Smart Sensing, Processing, and Instrumentation (Vol. 2718, pp. 251-258). International Society for Optics and Photonics.
[54] Guan, Z. G., Chen, D., & He, S. (2007). Coherence multiplexing of distributed sensors based on pairs of fiber Bragg gratings of low reflectivity. Journal of lightwave technology, 25(8), 2143-2148.
[55] Inaudi, D. (1995). Coherence multiplexing of in-line displacement and temperature sensors. *Optical Engineering*, *34*(7), 1912-1916.
[56] Jones, M. E., Grace, J. L., Greene, J. A., Tran, T. A., Bhatia, V., Murphy, K. A., & Claus, R. O. (1995, April). Multiplexed absolute strain measurements using extrinsic Fabry-Perot interferometers. In Smart Structures and Materials 1995: Smart Sensing, Processing, and Instrumentation (Vol. 2444, pp. 267-276). International Society for Optics and Photonics.
[57] Al-Chalabi, S. A., Culshaw, B., & Davies, D. E. N. (1983, April). Partially coherent sources in interferometric sensors. In First International Conference on Optical Fibre Sensors (pp. 26-28).
[58] Rao, Y. J., & Jackson, D. A. (1996). Recent progress in fibre optic low-coherence interferometry. Measurement Science and Technology, 7(7), 981.
[59] Choi, H. S., Taylor, H. F., & Lee, C. E. (1997). High-performance fiber-optic temperature sensor using low-coherence interferometry. Optics letters, 22(23), 1814-1816.

[60] Totsu, K., Haga, Y., & Esashi, M. (2004). Ultra-miniature fiber-optic pressure sensor using white light interferometry. Journal of Micromechanics and Microengineering, 15(1), 71.
[61] Belleville, C., & Duplain, G. (1993). White-light interferometric multimode fiber-optic strain sensor. Optics letters, 18(1), 78-80.
[62] Jedrzejewska-Szczerska, M., Gnyba, M., & Kosmowski, B. B. (2011). Low-coherence fibre-optic interferometric sensors. Acta Phys. Pol. A, 120(4), 621-624.
[63] Jia, X. H., Rao, Y. J., Wang, Z. N., Zhang, W. L., Jiang, Y., Zhu, J. M., & Yang, Z. X. (2012, October). Towards fully distributed amplification and high-performance long-range distributed sensing based on random fiber laser. In OFS2012 22nd International Conference on Optical Fiber Sensors (Vol. 8421, p. 842127). International Society for Optics and Photonics.

CHAPTER VI

Summary, conclusions and open research lines

6.1. Summary and conclusions

Fiber optic sensor technology has experienced tremendous growth since its early beginnings in the 1970s, when it was envisioned for sensing physical and chemical parameters. Besides, the demonstration of the first fiber laser in 1961 brought intensive research into fiber laser technology, which has radically changed the market situation in the industrial laser sector, optical communications and sensing applications.

In this framework, an original study about novel Rayleigh scattering-based fiber optic systems for sensing applications has been presented in this thesis. Most of them are based on random distributed-feedback fiber lasers (RDFB-FL). The schemes of all the configurations are included once again to ease the comprehension of the conclusions.

Chapter III has been mostly dedicated to presenting a new set of high-resolution sensing applications based on RDFB-FLs. These original schemes aim to solve two of the main challenges faced by high resolution systems based on traditional fiber lasers: first, the instabilities caused by mode hopping and mode competition and secondly, the limited resolution provided by optical devices compared to the electrical ones.

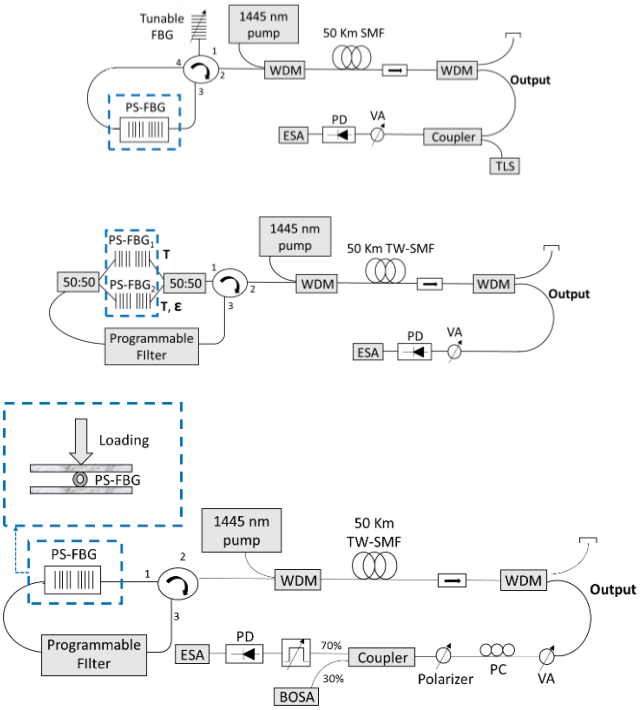

Figure 6. 1. RDFB-FL-based schematic diagrams proposed for high resolution temperature, strain and transversal load measurements, respectively.

The first study focuses on achieving high resolution temperature measurements by narrowing the naturally wide output spectrum of a RDFB-FL to a linewidth of a few picometers. A phase-shifted fiber Bragg grating has been chosen to act as the sensing and filtering element in the RDFB-FL cavity. The outstanding frequency and amplitude stability of these lasers together with their mode-less behavior avoid the mode-related instabilities inherent

to traditional-cavity fiber lasers thus providing enhanced resolution. In addition, the distinctive features of the generated emission line, such as a pm-linewidth and a continuous self-beating electrical spectrum (without peaks), allows the application of heterodyne detection techniques. Although the detection process could also be performed in the optical domain by tracking the wavelength shift of the laser emission line, the maximum resolution of the system would be limited by the optical detection devices. For this reason and to avoid this limitation, the sensor signal has been detected in the electrical domain, achieving a maximum resolution of 0.01°C.

From this initial proposal, two other schemes for strain and transversal load measurement have been developed introducing some variations in the original set-up. However, the heterodyne detection technique has been implemented in both systems to measure the response of the PS-FBG sensor and maximize their performances. A high resolution axial strain sensor system with a measured resolution of 0.2 με has been achieved. Among its advantages, its ability to self-compensate any temperature variation, avoiding crosstalk with the axial strain measurements, is especially remarkable. Then, a transversal load sensing system with a 1 g resolution is accomplished. Although this scheme shows a great potential when compared with previous published works, several improvements in this particular experimental set-up could be performed to increase the obtained resolution.

The next part of the chapter has been dedicated to examine the performance of different types of FOS at cryogenic temperatures. In fact, the previously developed RDFB-FL-based temperature sensor was tested for this particular application. Moreover, the performances of a distributed sensor, several interferometric (Sagnac and photonic crystal fiber (PCF) Fabry-Perot-based) and FBG-based FOS have been analyzed, comparing their advantages and drawbacks. Their most crucial parameters such as size, response time, absence or presence of coating, sensitivity and resolution have been taken into account in this comparison. A simple experiment has been carried out using liquid nitrogen to decrease temperature to -160^{o}C. As a general conclusion, performing measurements at cryogenic temperatures is a complex task for several reasons:

- The reduced spaces needed to perform the measurements might cause large power losses and sometimes damage the sensors due to the difficult handling.
- Pure cryogenic temperatures are difficult to reach and to maintain constant for long periods of time. Isolation and

temperature gradients in the measuring locations play a significant role and affect the accuracy and resolution of the measurements.

- Due to the fast response required, sensors with larger size or showing high response time may not be suitable for this particular application. Considering these factors, reduced-size sensors, such as FBG-based fiber sensors or PCF Fabry-Perot interferometers, have proven to be more advantageous.

Finally, a phase-OTDR system for quasi-distributed vibration measurements has been proposed in the last subsection of this chapter. An additional theoretical and experimental study has been developed to enhance the performance of the system. From the work done on distributed systems, several conclusions can be drawn:

- The obtained results verify that quasi-distributed systems are a powerful tool to monitor all types of structures. The proposed system was capable of detecting where fiber vibration occurs, as well as extracting the vibrational frequency at that particular point and along the entire sensing fiber. The use of weak-FBGs inscribed along the fiber have allowed to improve the SNR and the general precision of the vibration detection system.

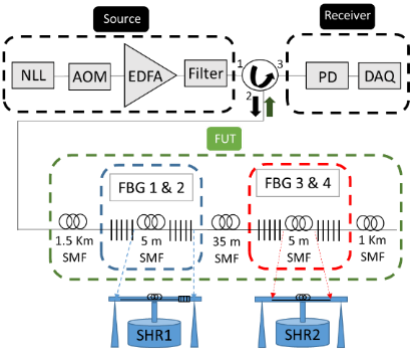

Figure 6. 2. Phase-OTDR experimental set-up for improved performance vibration measurements.

- In addition, an extensive theoretical analysis of the signals involved in the system has allowed to develop a post-processing method that reduces the spectral shadowing crosstalk and improved the overall performance of the structure. In this particular approach, only two pair of gratings were monitored to

verify the validity of the proposed technique in a simple manner. However, the formalism and suppression technique developed can directly be applied to equidistant FBG arrays. In the case of interrogating an array of dozens of gratings, the spectral shadowing crosstalk accumulated at the end of the fiber may degrade the quality of the detected signal and can lead to poor fault detection. For this reason, the proposed method would be an interesting technique to implement in this type of applications.

The second experimental part of this work, which comprises chapter IV and V, provides the activity carried out in the field of remote optical sensor networks. Two of their major challenges have been covered, such as enhance their multiplexing capability and increase the monitoring distance. All the presented schemes have in common the use of RDFB-FLs for the remote interrogation of the sensor structure. However, two approaches have focused on increasing the number of multiplexed sensors while two other have focused on extending the monitoring distance.

Regarding the need to increase the number of sensors that can be multiplexed on a single network while ensuring good signal quality, the following methods have been provided:

- A multi-wavelength RDFB-FL for its use in a WDM sensor network
- An Internally-modulated RDFB-FL for hybrid WDM/TDM

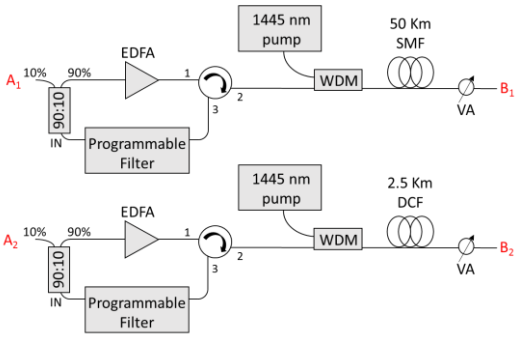

Figure 6. 3. Schemes using two different Raman gain medium.

First, a multi-wavelength fiber laser (MWFL) scheme is presented in Chapter IV for its later use in a WDM sensor network. With this objective in mind, a previous experimental study has been performed in order to maximize the number of emission lines generated in the L-band. Two different fibers have been tested as the gain medium of the laser, single-mode fiber (SMF) and dispersion compensating fiber (DCF). Although the DCF guaranteed a higher output power, the SMF ended being the best candidate in this particular case. With the latter, the number of multiplexed sensors can be greater and its low losses per km make it more suitable for long haul applications. Among the conclusions drawn from these optimization experiments, it should be highlighted the importance of making a right choice of the gain-media fiber in the RDFB-FL, since it affects notably the shape, wavelength and power of the generated spectrum. From the work developed in this section, the following aspects should be remarked:

- A novel software has been developed to control the programmable filter which tailors the laser spectrum, providing great versatility and improving the overall performance of the system. In addition, this method has demonstrated an easy integration and control from the header fiber loop.
- Thanks to this software, the MWFL generated can be employed in optical communications applications as well as in multiplexed sensor networks. The customized filters satisfy the ITU grid specifications, meeting both the separation and width requirements of the channels. The system showed a more convenient performance for separations greater than 100 GHz between lines. Smaller distances enhanced non-linear effects and decreased the power stability of the emission lines.
- The number of emission lines has been increased by applying two methods. First, a hybrid amplification scheme which combines RDFB and EDFA amplification allowed to enlarge the total amplification bandwidth. Then, power equalization of the uneven generated emission lines has been carried out thanks to the customized software of the programmable filter.

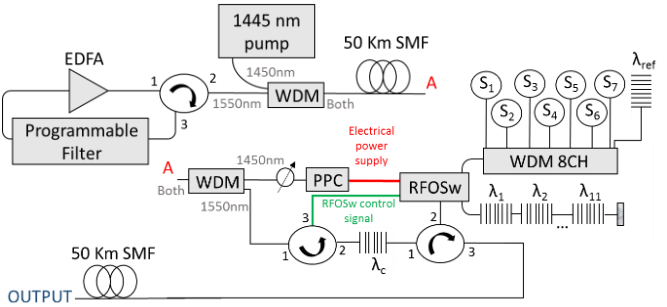

Figure 6. 4. Schematic representation for the multi-wavelength RDFB-FL and for the remote sensor network.

The optimized MWFL scheme has been tested to interrogate two remote optical fiber networks, and the results obtained have been gathered in Chapter V. An experimental validation of this proposal has been performed, achieving a switchable and reconfigurable MWFL in real-time based on a RDFB-FL, see Figure 6. 4. Two sensor networks have been simultaneously monitored at 50 km using a remote powered-by-light fiber optic switch. From these experiments, the following conclusions can be drawn:

- The presented technique allows to interrogate as many sensor networks as outputs has the optical switch, which expands the multiplexing capacity of the network.
- In this proof-of-concept approach, two sensor networks have been monitored simultaneously: one composed of 11 gratings and another composed of 7 interferometric sensors. The spectral versatility of the RDFB-FL makes possible the interrogation of both networks by implementing WDM.
- The developed scheme is also power efficient, since it uses the excess Raman pump to power the RFOSw. In addition, the control signal is generated by the MWFL together with the sensor monitoring signal, avoiding the need of an additional control device.

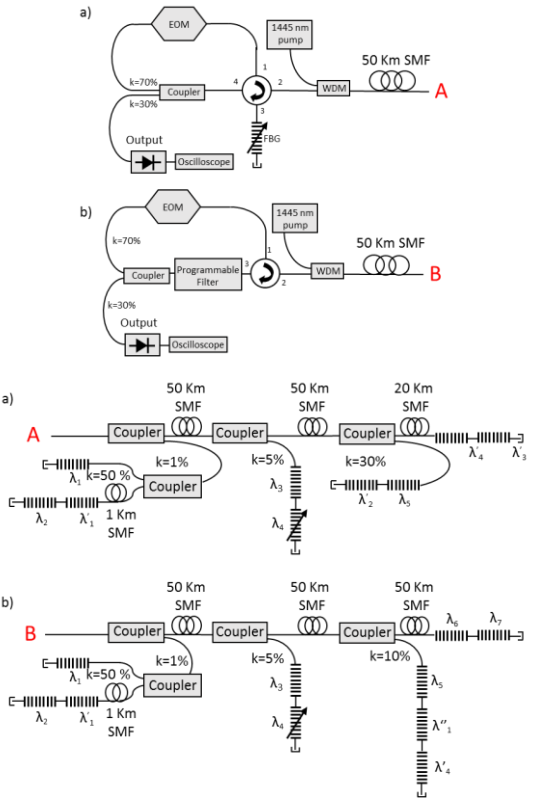

Figure 6. 5. Experimental setups of the proposed hybrid WDM/TDM sensor networks in the a) first approach using a tunable-FBG and b) second improved approach applying a programmable filter.

Secondly, an optical sensor network which implements hybrid WDM/TDM has been proposed in subsection 5.3. This approach offers a promising solution to improve the generally limited multiplexing capacity of the ultra-long range remote sensing systems, see Figure 6. 5. A RDFB-FL has been internally modulated without frequency restrictions, offering a new range of possibilities and allowing to identify the sensors using time-domain reflectometry. From an initial proof of concept scheme, several studies have been carried out to optimize the general features of the system. Spatial resolution, maximum distance and wavelength range have been increased. The main conclusions extracted from this work are:

- The performed experiments verify that not only WDM can be implemented in a RDFB-FL scheme, but also TDM can also be applied, exploiting the advantages offered by both multiplexing techniques used jointly.
- The proposed system has demonstrated good repeatability and overall performance for a maximum of 10 sensors and a 200 km range.
- The use of a programmable filter to filter the cavity instead of a tunable FBG has demonstrated to be an advantageous tool, which allows to improve the general performance of the system and its versatility.

Regarding the need to enlarge the monitoring distance of the optical sensor network, two experiments have been carried out:

- A 225-km remote real-time interferometric sensor monitoring using a RDFB-FL
- A 290-km remote displacement sensor monitoring by a double-pumped second order RDFB-FL scheme.

In subsection 5.4, a new sensing application of RDFB-FL which implements a real-time FFT analysis to monitor a 225-km-remote interferometric sensor is presented and demonstrated, see Figure 6. 6. The combination of the FFT technique and a RDFB-FL has been exploited to monitor the axial strain applied to the interferometer, obtaining a good linearity and a sensitivity of 1.69 πrad/mε. The most relevant conclusions derived from this work are:

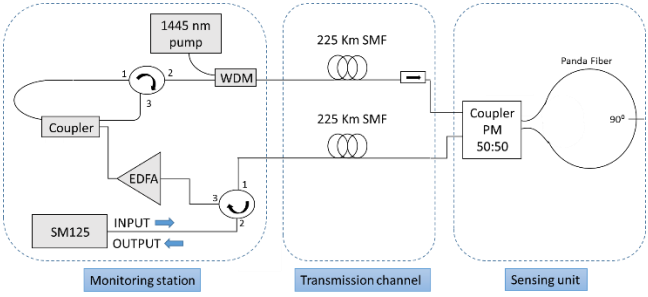

Figure 6. 6. Experimental set-up (EDFA: Erbium doped fiber amplifier; PM: Polarization maintaining).

- It has been demonstrated that not only gratings are suitable for long distance sensor networks. In addition, this proposal offers a solution to the main problems of interferometric sensors in remote sensor networks: their low multiplexing capability and high losses. In fact, several interferometric sensors could be multiplexed and remotely monitored using FFT analysis by combining the RDFB-FL with the commercial FBGs interrogator.
- An extensive variety of physical parameters could be measured using other types of interferometric sensors, such as MZ interferometers, and Hi-Bi fibers, depending on the requirements of the application.
- The performance of the system could be further improved by modifying the additional amplifier device in the header of the RDFB-FL. A larger amplification bandwidth and a higher gain will allow to increase the resolution of the measurements and the distance to the sensor unit.

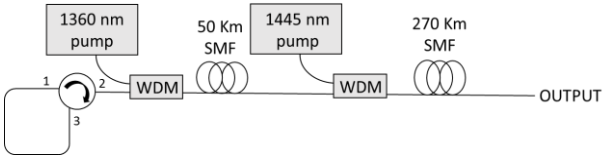

Figure 6. 7. Scheme with two pump lasers analyzed.

Finally and similar to the MWFL case, an experimental optimization study of a double-pumped RDFB-FL structure for long-haul applications has been performed in Chapter IV. This optimized structure (Figure 6. 7) implements two pump lasers connected in series and takes advantage of second-order laser generation. The order of the pump lasers, their separation distance as well as the pump powers injected were adjusted to maximize the output power of the system. As general conclusions from the developed experiments:

- A distance of tens of kilometers between pump lasers should be applied. First Stokes laser generation must be achieved in the fiber section that separates both pump lasers. In this manner, the generated signal (first stokes) will be reinforced by the following pump laser to achieve second-order laser generation.
- Theoretical and simulation studies may be useful for the optimization process.

The last section of Chapter V considers the aforementioned double-pumped scheme as the light source for a fiber optic low-coherence interferometry (FOLCI) scheme, see Figure 6. 8. The remote interrogation of an interferometric sensor has been achieved 290 km away from the header. This is, as far as we are aware, the longest distance for a remote fiber optic sensing system. In addition, its ability to achieve coherence division multiplexing has been proved. The particular properties of RDFB-FL, such as their high power and relatively short coherence length, make them suitable for CDM and long-haul remote applications. As conclusions, we can emphasize that:

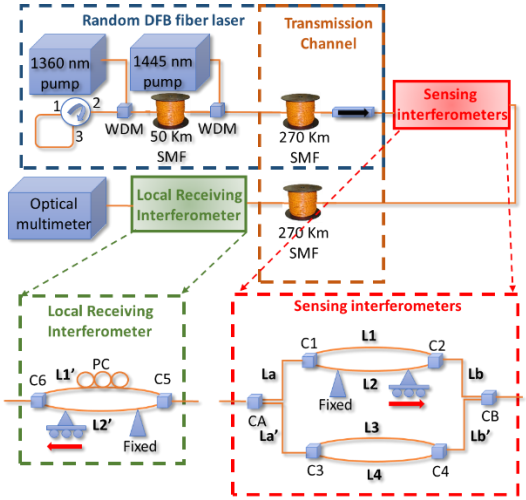

Figure 6. 8. Schematic set-up to monitor a 290-km remote optical sensor network implementing CDM and double-pump second-order amplification RDFB-FL.

- The obtained results showed the great potential of FOLCI schemes in remote sensing applications when using RDFB-FL as the light source.
- Although this approach can be considered as a proof-of-concept, the accuracy of the measurements could be enhanced by modifying the receiving interferometer setup (improve noise isolation or polarization control) and improving the accuracy of the mechanical sweep applied to both sensors, without crosstalk.

- This last system represents the longest range sensor system reported so far that includes fiber sensor multiplexing capability.

As a final conclusion, the experiments developed in this chapter verify the great versatility that RDFB-FLs offer for their use in remote monitoring applications. As it has been previously stated, there is no ideal solution for all remote sensing scenarios. In fact, in several of the proposed schemes it is necessary to double the fiber in the system to avoid the counter propagating noise. However, a cable of two fibers can be used instead of a single-fiber cable so it does not present a significant increment in the final costs of the installation. Nevertheless, the outstanding features of RDFB-FL allow their adaptation to a great variety of applications. Actually, RDFB-FL have demonstrated their capability to interrogate sensors of different nature (FLM, MZ interferometers and FBGs), to implement several multiplexing techniques (WDM, TDM and CM) as well as combinations thereof, all at distances of hundreds of kilometers.

6.2. Open research lines

Once the conclusions are exposed, the research lines that this works has not covered will be summarized, along with other details that should be considered in future work.

Being consistent with the scheme followed throughout the work, the proposed future research directions can be classified into two groups:

- The related with high-resolution sensor systems

The first idea would be to implement other techniques that provide higher sensitivity and resolution measurements. RDFB-FL-based sensing systems have demonstrated advantageous features for this purpose although there are room for improvement.

In relation to this fact, two main ideas can be applied to enhance the system performance. The first one would imply a further narrowing of the emission line-width, so the accuracy of the system could be improved. The other may involve the application of techniques to increase the sensitivity of the sensing element, such as improved-sensitivity FBGs (coated or bonded FBGs). These techniques would also enhance the performance of these sensors at cryogenic temperatures and enlarge the range of applications.

- The associated with challenges of optical sensor networks

In this thesis two of the challenges faced by optical sensor networks have been addressed. Reaching longer distances could be further investigated as well as increasing the number of sensor multiplexed in a network efficiently. Several schemes have been proposed to solve both demands. Regarding the multiplexing task, the proposal using FFT analysis may be a favorable solution to multiplex interferometric-type sensors. Its performance could be enhanced if the double-pump laser scheme (Figure 6. 7) were used as the light source. In this manner, the interrogation distance could be increased, making it possible to monitor several interferometric sensors at distances of hundreds of kilometers. Besides, a theoretical study simulating double-pump RDFB-FL would be highly valuable and could significantly expand the monitoring distance above 300 km.

Other future line may involve the internal modulation of the double-pump second-order amplification scheme. The use of a RDFB-FL in a time domain reflectometer-based scheme, see Figure 6. 5, has showed promising results enhancing the multiplexing capability of the sensor network and several approaches should be explored regarding this structure. In addition, more advanced reflectometry techniques and equipment could straightforwardly improve the performance of the system.

APPENDIX

List of publications related to the thesis

1. Papers in international journals

[1] **DeMiguel-Soto, V.**, Bravo, M., & Lopez-Amo, M. (2014). Fully switchable multiwavelength fiber laser assisted by a random mirror. Optics letters, 39(7), 2020-2023.

[2] Bravo, M., **de Miguel Soto, V.,** Ortigosa, A., & Lopez-Amo, M. (2015). Fully Switchable Multi-Wavelength Fiber Lasers Based on Random Distributed Feedback for Sensors Interrogation. Journal of Lightwave Technology, 33(12), 2598-2604.

[3] Leandro, D., **deMiguel Soto, V.**, Perez-Herrera, R. A., Acha, M. B., & López-Amo, M. (2016). Random DFB fiber laser for remote (200 km) sensor monitoring using hybrid WDM/TDM. Journal of Lightwave Technology, 34(19), 4430-4436.

[4] Leandro, D., **deMiguel-Soto, V.**, & Lopez-Amo, M. (2016). High-Resolution Sensor System Using a Random Distributed Feedback Fiber Laser. Journal of Lightwave Technology, 34, 4596-4602.

[5] **De Miguel-Soto, V.**, Leandro, D., Lopez-Aldaba, A., Beato-López, J. J., Pérez-Landazábal, J. I., Auguste, J. L., Jamier, R., Roy, P. & Lopez-Amo, M. (2017). Study of Optical Fiber Sensors for Cryogenic Temperature Measurements. Sensors, 17(12), 2773.

[6] **DeMiguel-Soto, V.**, Leandro, D., & Lopez-Amo, M. (2018). Ultra-long (290 km) remote interrogation sensor network based on a random distributed feedback fiber laser. Optics Express, 26(21), 27189-27200.

[7] **De Miguel Soto, V.,** Jason, J., Kurtoğlu, D., Lopez-Amo, M., & Wuilpart, M. (2019). Spectral shadowing suppression technique in

phase-OTDR sensing based on weak fiber Bragg grating array. Optics letters, 44(3), 526-529.

2. Papers in international journals under review

[1] **De Miguel Soto, V.** and Lopez-Amo, (2019). Truly remote interrogation of fiber-optic sensor networks. Journal of Physics Photonics.

3. Papers in international conferences

[1] Acha, M. B., **DeMiguel-Soto, V.,** Ortigosa, A., & Lopez-Amo, M. (2014, June). Fully switchable multi-wavelength fiber laser based interrogator system for remote and versatile fiber optic sensors multiplexing structures. In 23rd International Conference on Optical Fibre Sensors (Vol. 9157, p. 91576P). International Society for Optics and Photonics.

[2] **DeMiguel-Soto, V**., Leandro, D., & Lopez-Amo, M. (2016, May). *High-resolution transversal load sensor using a random distributed feedback fiber laser*. In Sixth European Workshop on Optical Fibre Sensors (Vol. 9916, p. 991606). International Society for Optics and Photonics.

[3] **DeMiguel-Soto, V**., Lopez-Aldaba, A., Leandro, D., & Lopez-Amo, M. (2016, October). Ultra-Long random laser for remote real-time interferometric sensor monitoring using FFT analysis. In Asia-Pacific Optical Sensors Conference (pp. Tu3A-4). Optical Society of America.

[4] **DeMiguel-Soto, V.**, Leandro, D., Lopez-Aldaba, A., Beato-López, J. J., Pérez-Landazábal, J. I., Auguste, J. L., Jamier, R., Roy, P. & Lopez-Amo, M. (2017, April). Interferometric vs wavelength selective optical fiber sensors for cryogenic temperature measurements. In 2017 25th Optical Fiber Sensors Conference (OFS) (pp. 1-4). IEEE.

[5] Lopez-Amo, M., Leandro, D., **de Miguel, V.**, Bravo, M., Fernández-Vallejo, M., & Perez-Herrera, R. A. (2017, July). Random fiber lasers: Application to fiber optic sensors networks. In 2017 19th International Conference on Transparent Optical Networks (ICTON) (pp. 1-4). IEEE.

[6] **DeMiguel-Soto, V.**, Leandro, D., & Lopez-Amo, M. (2018, September). Ultra-long (275 km) Random Distributed Feedback Fiber Laser for Remote Sensor Monitoring. In Optical Fiber Sensors (p. TuE23). Optical Society of America.

[7] Kivilcim, Y., Per-Johan, J., **De Miguel Soto, V**., Lopez-Amo, M., Mégret, P. and Wuilpart, M. , "Performance evaluation of phase-OTDR sensing system based on weak fiber Bragg grating array" in IEEE Photonics Society Benelux Chapter 2018, 20-23, Bruxelles, Belgique, 2018.

4. Papers in national conferences

[1] **DeMiguel-Soto, V**., Lopez-Aldaba, A., Leandro, D., & Lopez-Amo, M. "Láser random ultra largo para monitorización de sensores interferométricos remotos en tiempo real usando la FFT" in Conference: 10ª Reunión Española de Optoelectrónica, OPTOEL17 at Santiago de Compostela, July 2017.